Hyperelastic Models for Granular Materials

Paul W. Humrickhouse

January 2009

UWFDM-1365

Ph.D. thesis.

FUSION TECHNOLOGY INSTITUTE

UNIVERSITY OF WISCONSIN

MADISON WISCONSIN

Hyperelastic Models for Granular Materials

Paul W. Humrickhouse

Fusion Technology Institute
University of Wisconsin
1500 Engineering Drive
Madison, WI 53706

http://fti.neep.wisc.edu

January 2009

UWFDM-1365

Ph.D. thesis.

HYPERELASTIC MODELS FOR GRANULAR MATERIALS

by

Paul W. Humrickhouse

Under the supervision of

Michael Corradini

Nuclear Engineering and Engineering Physics

University of Wisconsin

Madison WI 53706

January 29, 2009

ABSTRACT

Motivated by the need for a continuum mechanical description of particulate materials for nuclear safety analyses, several recently proposed hyperelastic models for granular materials are analyzed and compared with experiment data. As even the quasi-elastic regime of granular materials is non-linear, the hyperelastic forms considered here are all designed to capture the widely observed dependence of the elastic moduli on the square root of pressure. Building this sort of dependence in to the free energy results in some physically relevant behavior that is missed by other non-linear models, including stress-induced anisotropy and shear dilatancy. The granular elasticity (GE) model of Jiang and Liu additionally possesses a region outside a Drucker-Prager type yield surface in which the free energy is not convex, implying a lack of stable solutions there. This proves to be an over-constraint, as it limits yield angles to values lower than typically observed. Models due to Einav and Puzrin (EP), and Houlsby, Amorosi, and Rojas (HAR), lack this constraint, and thus provide greater flexibility; the EP model proves to best capture the sort of stress-induced anisotropy observed in experiments. All three models are implemented in the finite element code Abaqus, and used to calculate stress distributions in sand piles and silos, and the granular response function. The models agree qualitatively, but not always quantitatively, with experiments; paradoxically, the EP model proves to be the least accurate, producing an unphysically narrow and high peaked response function. They also possess shortcomings similar to those of linear elasticity. In silos with an applied surface load, they underestimate the observed "overshoot" of the saturated stress. For both sand piles and the response function, the stress profiles are insensitive to the values of the elastic constants, and as such are not able to account for the range of data observed experimentally. Incorporating some dependence on the pile formation history is likely necessary to describe these effects. In light of the findings, and the relative simplicity it affords, linear elasticity (despite its known shortcomings) is an appropriate choice for coupling to flow models in engineering analyses.

ACKNOWLEDGMENTS

Thanks are due to the many people who have shaped my experience at UW and at INL, without whom this work would not have been possible. My advisor, Mike Corradini, was charged with the difficult task of keeping tabs on a student over a thousand miles away, but has always been available and has continually been a source of new ideas and much needed direction. I am grateful to Phil Sharpe, my INL mentor, for encouraging me to pursue the technical problems I found most interesting, for his continued patience, and for bringing me to INL many years ago. It has been a pleasure to work with him and everyone else in the Fusion Safety Program at INL, and I look forward to continuing my work there. Lee Cadwallader deserves special thanks for his careful reading of this manuscript, and most of my other papers. In earlier years at UW, I enjoyed working with and learned a lot from Paul Wilson, my M.S. advisor, everyone at UWNR, and the professors in the College of Engineering, too many to name, who taught me through my undergraduate and graduate careers; your efforts were probably underappreciated at the time. Finally, I am eternally grateful to my parents, Scott and Deb, for their continued support and guidance throughout my life- I would not be here today without it.

DISCARD THIS PAGE

TABLE OF CONTENTS

DISCARD THIS PAGE

LIST OF FIGURES

Figure Page

Appendix
Figure Page

Figure Page

DISCARD THIS PAGE

LIST OF TABLES

1 Introduction

Granular materials, though ubiquitous in nature and widely used in engineering and construction, remain relatively poorly understood. They may variously behave like solids, liquids or gases, though typically exhibiting a variety of unexpected behaviors that are not encountered in these conventional forms of materials. The preponderance of problems yet to be solved has sparked a renewed interest in granular materials, particularly in the physics community [1].

Much of this new research has focused on a discrete element description of granular materials, analogous to molecular dynamics. In many situations this is the most intuitive and appropriate way to describe the system, and there is much insight to be gained from such analyses. On the other hand, many granular systems are comprised of very many particles which are small relative to the system under consideration. This is the limit in which continuum models apply. Clearly there are many engineering problems for which the continuum description is simpler and more appropriate, and we consider the applicability of various continuum models in what follows.

For both static and flow problems, constitutive models are notoriously problem-specific; in a review of recently proposed flow models, it was noted [2] that none seem to work for more than a single problem. As we will see, the situation is similar for granular statics. Linear elasticity is regularly employed to calculate static stress distributions, or coupled with various plasticity models, though we know granular statics is not always well described by linear elasticity. An analogous situation for flow problems would be modeling a granular material as a Newtonian fluid. The author is not aware of any flow models employing such an oversimplification. Non-Newtonian models for granular flow have even made their way into CFD codes such as Fluent [3]. Seeking to rectify the failings of linear elasticity, in recent years hyperelastic models have been proposed for granular materials. These have been successful in describing some aspects of granular statics absent from linear elasticity, and a critical evalutation is given here.

While one important objective of the present work is to evaluate continuum models for generality, there is a specific problem to which we shall regularly refer. This is the mobilization of a granular pile sheared by a flowing gas. This type of problem is of interest in nuclear systems, both fission and fusion. In tokamaks such as the International Experimental Thermonuclear Reactor (ITER), large quantities of particulate material are produced from wall materials through plasma-surface interactions [4, 5]. The material is potentially toxic, radioactive, tritiated, and if mobilized, could enable a dust explosion; thus, understanding how it is mobilized and transported during loss of vacuum or other accident scenarios is important. Similar issues may exist for gas-cooled fission reactors [6].

Interest in "mobilization" and "transport" suggests we are solving a flow problem. But this is not always the case. Experiments designed to study mobilization of dust (appendix B, [7]) clearly indicate that it does not always flow; for sufficiently low flow rates, dust piles remain entirely static. When does flow begin? This is usually understood in terms of a "yield surface" that divides allowed and unobtainable static stress states. Thus the static problem is a prerequisite to the flow problem. Unfortunately, as was noted, models for granular statics tend to over-simplify; they are either tailored to very specific types of problems, or simply employ linear elasticity, for lack of a better model, and despite its inability to describe many characteristics of granular materials.

We begin with a review of some noteworthy aspects of granular behavior, and of the various existing models for granular statics, in section 2. The focus of the work is primarily on three recently proposed hyperelastic models, which successfully describe many granular phenomena, despite their relative simplicity. The motivation for and applicability of hyperelastic models is discussed in section 3. Some analytical results from these theories are compared with experiment data in section 4, and finite element calculations of stress distributions are presented in section 5.

2 Statics of Granular Materials

2.1 Some Characteristics of Granular Materials

2.1.1 Yield

Our earliest knowledge of granular materials is due to Coulomb [8]. He observed that in static equilibrium, in accordance with static friction, the shear τ_n on a plane of granular material cannot exceed a constant fraction of the normal force σ_n:

$$\tau_n \leq \mu_f \left(-\sigma_n\right) + c \tag{2.1}$$

where μ_f is the coefficient of friction, and c is a constant of cohesion. We take the usual sign convention of solid mechanics (contrary to some work in soil mechanics and granular materials), with tension positive. Here and throughout (except in appendix G), we will ignore cohesive effects and take $c = 0$. We may also redefine the friction coefficient in terms of the Coulomb angle or angle of internal friction:

$$\left|\frac{\tau_n}{\sigma_n}\right| \leq \mu_f = \tan\phi \tag{2.2}$$

In terms of the actual stress tensor components,

$$\tau^* - \sigma^* \sin\phi \leq 0 \tag{2.3}$$

where

$$\tau^* = \sqrt{\frac{1}{4}\left(\sigma_{xx} - \sigma_{yy}\right)^2 + \sigma_{xy}^2} \tag{2.4}$$

is the radius of Mohr's circle, and

$$-\sigma^* = \frac{1}{2}\left(\sigma_{xx} + \sigma_{yy}\right) \tag{2.5}$$

its center (figure 2.1). All stable stress circles, then, are bounded by the line defined by the friction angle ϕ. If the stress state reaches the yield surface, then plastic deformations ensue; we will be primarily interested in the static problem here, though some yield surfaces and plastic flow models are considered in appendix A.2.

Extending the Mohr-Coulomb condition to three dimensions results in either a hexagonal cone or cone in principal stress space. In the former case, it is assumed that there is no dependence on the intermediate principal stress σ_2, in which case the major and minor principal stresses are given by

$$\sigma_1 = -\left(\sigma^* + \tau^*\right) \tag{2.6}$$

$$\sigma_3 = -\left(\sigma^* - \tau^*\right) \tag{2.7}$$

with the yield surface defined by

$$\frac{1}{2}\left(\sigma_3 - \sigma_1\right) + \frac{1}{2}\left(\sigma_3 + \sigma_1\right)\sin\phi = 0 \tag{2.8}$$

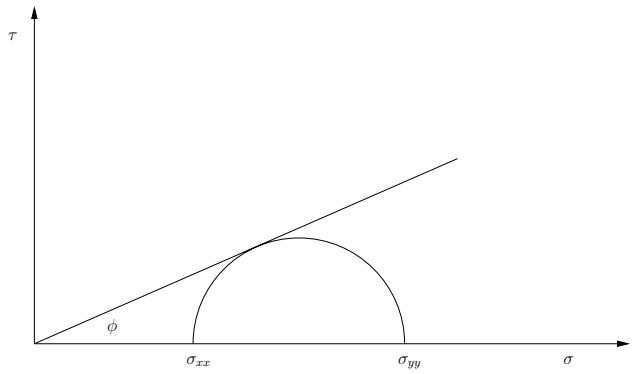

Figure 2.1. The Coulomb yield criterion and Mohr's circle. τ and σ are the shear and normal stresses, σ_{xx} and σ_{yy} are the principal stresses, and ϕ is the angle of internal friction or Coulomb angle.

or

$$\frac{\sigma_1}{\sigma_3} = \frac{1+\sin\phi}{1-\sin\phi} \tag{2.9}$$

For the conical (Drucker-Prager) yield surface (also known as the conical von Mises yield surface, see appendix A.2),

$$\sigma_s^2 - C^2 P^2 = 0 \tag{2.10}$$

where the stress tensor invariants P and σ_s^2 are given by

$$P = \tfrac{1}{3}\left(\sigma_{xx} + \sigma_{yy} + \sigma_{zz}\right) \tag{2.11}$$

$$\sigma_s^2 = \sigma_{xx}^2 + \sigma_{yy}^2 + \sigma_{zz}^2 + 2\tau_{xy}^2 + 2\tau_{yz}^2 + 2\tau_{xz}^2 - 3P^2 \tag{2.12}$$

or in terms of the principal stresses,

$$P = \tfrac{1}{3}\left(\sigma_1 + \sigma_2 + \sigma_3\right) \tag{2.13}$$

$$\sigma_s^2 = \frac{1}{3}\left(\left(\sigma_1 - \sigma_2\right)^2 + \left(\sigma_2 - \sigma_3\right)^2 + \left(\sigma_3 - \sigma_1\right)^2\right) \tag{2.14}$$

C is a constant; if we assume $\sigma_2 = \left(\sigma_1 + \sigma_3\right)/2$ (appropriate for plane strain [9]),

$$C = \frac{\sin\phi}{\sqrt{2}} \tag{2.15}$$

Note that this is not the same angle as that defined by plotting σ_s vs. P in 2D. More complicated yield surfaces are commonly employed in modeling plastic flows, see appendix A.2. Whatever yield surface is employed, stress states that fall within it are stable and must be treated with a suitable static model; this is the subject of the present work.

For a Mohr-Coulomb yield condition, the friction angle is identical to the angle of repose, the latter identifying the steepest stable slope of a granular pile or layer. For other surfaces, there is not always a unique definition of the "friction angle" (as evidenced above), and may be different from the angle of repose.

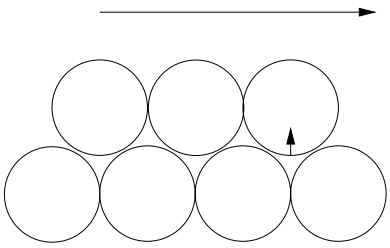

Figure 2.2. Dilatancy in a granular layer: particles must slide up and over each other while undergoing shear deformation.

Modaressi and Evesque, for example, have modeled stable piles using the Drucker-Prager model with angles of repose higher than the friction angle [10]. Typical angles of repose are in the range 10°-20° for perfectly spherical particles, $\sim$ 30°-40° for more irregular materials such as sand [11], and perhaps as high as 60° for very angular materials [12]. The angle of repose is, not surprisingly, dependent on the geometry of the pile. Different values for the angle of repose are obtained for conical and wedge shaped piles, and for a cone vs. a conical crater (i.e., a convex vs. concave surface) [13, 14]. There are also observed differences depending on the preparation method; pouring a sand wedge into a box, for example, may result in different angles than draining from a filled box [11, 15], and the presence of walls increases the angle of stability [11, 12, 15]. One may also identify a distinct "angle of movement"; a layer poured at its angle of repose may be carefully tilted slightly higher by a degree or two, at which point an avalanche occurs, and the pile relaxes to the angle of repose [11, 16]. If the experiment is performed in a rotating drum, the rate of rotation may be increased such that avalanches cease to be discrete events, allowing for the definition of a "dynamic" angle [13, 14, 17].

2.1.2 Dilatancy

Reynolds [18] first observed that granular materials possess dilatancy; when sheared, they also undergo a volume expansion. This can lead to some rather non-intuitive behavior, as described by Duran [14]. For example, consider a rubber pouch or balloon filled with sand and liquid, with a thin tube penetrating the top. Intuition suggests that squeezing the pouch should result in a rise of the level of the liquid in the tube, but in fact the opposite occurs: the liquid level falls. Changing the shape of the compacted sand results in a volume expansion, and more liquid fills the balloon.

The dilatancy principle is easier to understand by considering a discrete granular layer (figure 2.2). In order to undergo shear deformations, layers of particles must roll or slide up and over the top of each other. For a more quantitative discussion of the problem, see Duran [14].

2.1.3 Arching, "stress propagation", and the stress dip in sand piles

Experimental measurements of the stress distribution at the bottom of sand piles have revealed rather counter-intuitive behavior: the stress sometimes possesses a dip, rather than a maximum, under the peak of

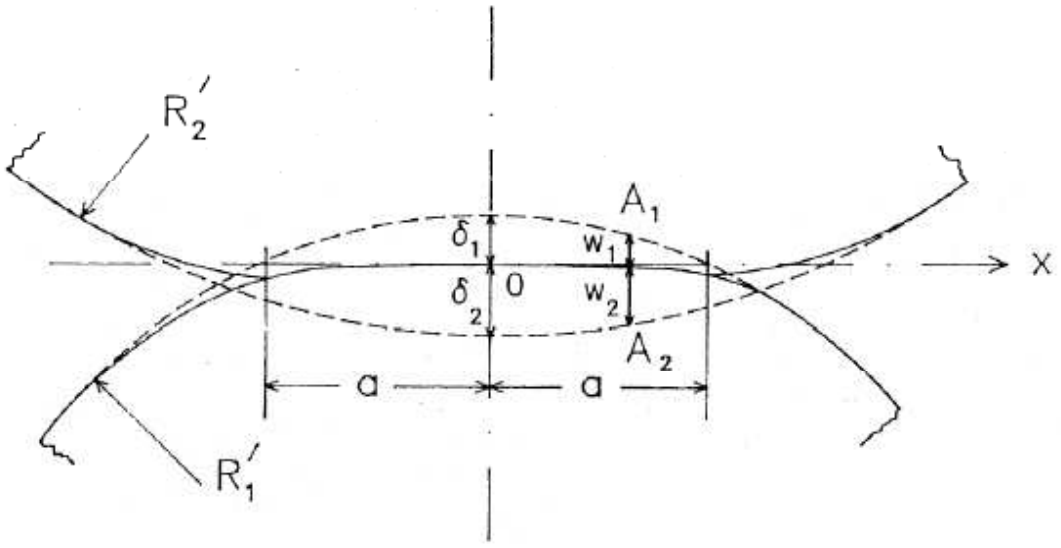

Figure 2.3. Two spheres deforming elastically under load [28]. If they have identical radii (i.e. $R_1' = R_2'$) then $\delta_1 = \delta_2$.

the pile [19]. This is thought by some to be related to the the ability of granular materials to form arches [14] and "force chains" [20], and has led some to propose a description of granular materials in which stresses "propagate" [21, 22], governed by hyperbolic rather than elliptic equations as in elasticity. The competing descriptions and the stress dip problem have sparked a heated debate in recent years [23]. The stress dip has also been variously explained by anisotropy [24] and density inhomogeneity [25]. The applicability of hyperbolic vs. elliptic models will be considered in subsequent sections.

2.1.4 The Hertz problem and non-linearity at small strains

An intuitive starting point for granular mechanics is the deformation of two elastic spheres in contact. This problem was originally solved by Hertz [26] and is described by Landau and Lifshitz [27]. As two particles of radius R are pressed together by a force F, the radius of their circular contact area a increases, and each suffers a displacement δ (Figure 2.3).

Hertz established that

$$a = \left(\frac{RF}{K_e}\right)^{1/3} \tag{2.16}$$

and

$$\delta = \frac{a^2}{R} \tag{2.17}$$

where K_e is an "effective" elastic modulus given in terms of the bulk and shear moduli K and G by

$$K_e = \frac{8G(3K+G)}{3(3K+4G)} \tag{2.18}$$

Thus the applied force is related to the deformation by

$$F = K_e \sqrt{R} \delta^{3/2} \tag{2.19}$$

and the elastic energy U_E is given by

$$U_E = \int F d\delta = \frac{2}{5} K_e \sqrt{R} \delta^{5/2} \tag{2.20}$$

Thus, due to the changing contact area a, the relationship between normal force and displacement for two spheres that are themselves linear elastic, is not linear. We anticipate, then, that bulk granular materials will possess non-linear stress-strain behavior, even at small strains.

2.2 Methods of Determining Static Stress

Before considering several new hyperelastic models for granular materials, we review briefly some existing methods for calculating static stresses. These are either elastic-type constitutive relations, which relate the stresses in some way to the strains, or stress-only closures, in which some special relation between stress components is proposed in order to close the force balance.

2.2.1 Mohr-Coulomb limit state analysis

Perhaps the simplest and oldest model for granular statics is to simply employ the Coulomb condition (equation 2.2, or equivalently equation 2.9), as an equality, which is sufficient to close the force balance in 2D [9, 29]. This places the material in a state of incipient failure everywhere (IFE). While perhaps useful as a bound for stable systems or in those close to yield, this will not be the case for many static systems of interest. Furthermore, what is desired is a model of granular statics that will be a predictive tool for yield; i.e., one in which stresses are calculated, and compared against some yield criterion. If yield is imposed from the outset, the IFE model is obviously not useful for this purpose.

2.2.2 The Janssen method for silos

The method of Janssen [30] is notable for its widespread use in design of silos. He assumes that the ratio of horizontal to vertical stress is a constant, given by

$$k_J = \frac{\sigma_{rr}}{\sigma_{zz}} \tag{2.21}$$

and that friction acts along the wall and is "fully mobilized", i.e. it takes the maximum static value

$$\sigma_{rz} = \mu_f \sigma_{rr} \tag{2.22}$$

Assuming that σ_{zz} is a function of z only, it is found to saturate with depth, in contrast with the usual hydrostatic pressure. The value of k_J is sometimes supposed to be related to the yield angle ϕ_y by the

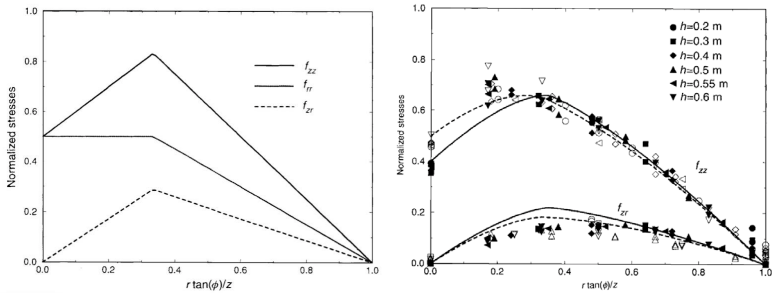

Figure 2.4. Stress dips produced by the FPA model, in 2D (left) and 3D (right). Reprinted by permission from Macmillan Publishers Ltd.: Nature [21], copyright 1996.

empirical relation [31]

$$k_J = 1 - \sin\phi_y \tag{2.23}$$

These conditions are sufficient to determine σ_{rr} and σ_{zz}. The Janssen problem is solved and compared with some numerical results in section 5.4.

2.2.3 Fixed Principal Axis

Another stress-only closure has been proposed more recently [21, 22, 32], whose motivation is explaining the stress dip that is sometimes measured at the center of sand piles. It is hypothesized that the principal axes of stress are "frozen in" during the pouring of the pile, leading to a relationship

$$\sigma_{rr} = \sigma_{zz} - 2tan\phi_y|\sigma_{zr}| \tag{2.24}$$

which is sufficient to close the 2D force balance. This gives wave equations with piecewise linear solutions that possess a stress dip (figure 2.4). Results are similar in 3D, though another constitutive relation is required (the second relation is not found to strongly influence the stress distributions [21]).

Though successful at producing a stress dip, it is not clear that the fixed principal axis (FPA) model would apply generally, tailored as it is to not only a specific problem geometry (conical pile), but a specific pile formation mechanism (pouring from a funnel). Indeed, it is found experimentally that piles formed by sieving lack the stress dip. Furthermore, FPA presumes to rectify a perceived failing of elastic-type constitutive models, namely that they do not produce the stress dip, but some, in fact, do. Cantelaube and Goddard find multiple solutions with a coupled linear elastic, Mohr-Coulomb plastic model, some of which possess stress dips [33, 34]. Others [25] have proposed that it may result from density inhomogeneity; grains rolling down the sides of pile are supposed to pack themselves more tightly at the edges of the pile, leaving a core of lesser density. See also critiques by Savage [23, 35] and comments by de Gennes [1].

FPA and other hyperbolic models also possess a double-peaked response function, which we consider in more detail in section 5.5. As experiments invariably give a single peak characteristic of elliptic (e.g. elastic) systems except for discrete and highly ordered systems, the general applicability of such models is

questionable. It is worth noting, however, that a proposed "force-chain splitting" mechanism may lead to elliptic systems beginning with FPA assumptions, see [36].

2.2.4 Linear Elasticity

All "stress only" closures have a similar shortcoming in that they do not account for deformations of the material; there is a large body of work dedicated to (quasi) elastic deformations, elastic moduli, and sound propagation in granular materials [37–58]. Probably the most common method of modeling the elastic region is to simply employ isotropic linear elasticity (ILE) up to the presumed point of failure on a Mohr-Coulomb or other yield surface (cf. [59, 60]). This treatment is simple, but there are many reasons why linear elasticity fails to properly describe granular materials. As we have seen, such materials cannot take tension, undergo shear dilation, and yield under relatively small shear stresses, none of which are accounted for by ILE. The aforementioned large body of work on the elastic moduli of soils demonstrates the non-linear, quasi-elastic regime clearly; the elastic moduli are not constant, but depend on the stress.

2.2.5 Non-linear elasticity: Effective Medium Theory and the Boussinesq model

As an improvement on linear elasticity, there have been attempts to incorporate nonlinear stress-strain relations or stress-dependent elastic moduli in the elastic framework. An early example is due to Boussinesq [61] (see also [62, 63]), who took elastic moduli $\sim \sqrt{u_{ii}}$, the square root of the trace of the small strain tensor, similar to Hertz contacts. Duffy and Mindlin [64] added Mindlin tangential forces to the Hertz model [28], and extended it to the continuum in a model referred to as the effective medium theory (EMT) [65]; for an increment of tangential force ΔF_t and corresponding tangential displacement Δs,

$$\Delta F_t = K_t \sqrt{R\delta} \Delta s \tag{2.25}$$

with K_t given in terms of the solid shear modulus G and Poisson's ratio ν,

$$K_t = \frac{8G}{2-\nu} \tag{2.26}$$

There are numerous additional examples in soil mechanics. Such models behave in ways inconsistent with the usual picture of elasticity; they may, for example, be path dependent [65] and fail to conserve energy [66, 67]. This has led to several proposed hyperelastic models [25, 63, 67–76], which, proceeding from a scalar free energy function, always conserve energy and are independent of path (the hierarchy of elastic models is described in section 3.1). In some cases these models do rather well at reproducing granular behavior including nonlinearity, shear dilation, and yield, but have been selectively or minimally tested against experiment data. It is this task that will be the focus of the present work.

There is an overwhelming body of experimental data that suggests the elastic moduli for dry granular materials do not have $K,\ G \sim P^{\frac{1}{3}}$ as in the Hertz model [37–57], but rather $K,\ G \sim P^{\frac{1}{2}}$. This has

been variously explained by Goddard [77] as due to either non-spherical contacts (e.g. sharp or conical contacts characteristic of angular particles) or an increase in the number of contacts with loading, and by de Gennes [78], who found that spherical particles with a soft shell (due to, say, oxidation) also have K, $G \sim P^{\frac{1}{2}}$. Whatever the micro-mechanical explanation, this experimental result is unambiguous, and will be our preferred stress dependence in what follows.

3 Elasticity

3.1 On the Validity of Elasticity for Granular Materials

"Elastic" is not an intuitive description of granular materials, so some comments on the validity of elasticity theory are in order. First, it should be clarified what is meant by "elasticity". In particular, we consider three different definitions, as outlined in [67, 79]. Elastic deformations are generally understood to be reversible. This does not preclude additional irreversible plastic strains, but henceforth when considering "strain" we are referring to the *elastic* strain, and assume that the total strain may be decomposed into elastic and plastic parts:

$$u_{ij}^{elastic} = u_{ij}^{total} - u_{ij}^{plastic} \tag{3.1}$$

The only way to ensure that the elastic strains are indeed reversible and energy is conserved, is to specify a strain energy potential $\mathcal{F}$, from which the stresses are given as functions of the strains by differentiation:

$$\sigma_{ij} = \frac{\partial \mathcal{F}\left(u_{ij}\right)}{\partial u_{ij}} \tag{3.2}$$

A material which possesses such a strain energy function is said to be *hyperelastic*. Alternately, the requirement of a strain energy potential may be relaxed, and instead we require only that the stresses are given as some function of the strains,

$$\sigma_{ij} = f_{ij}\left(u_{ij}\right) \tag{3.3}$$

In this case the material is said to be just *elastic*. If f is integrable such that $\mathcal{F}$ can be obtained, the material is in fact hyperelastic; thus, hyperelasticity is a special case of elasticity. Taking this line of thinking a step further, we might also consider a material in which we define only the incremental stress-strain relation:

$$\delta\sigma_{ij} = f_{ijk\ell}\left(u_{ij}\right)\delta u_{k\ell} \tag{3.4}$$

This type of relation is called *hypoelastic*. Once again, if f were integrable we would obtain stresses as a function of strains, and recover the *elastic* case. The incremental relation for the elastic and hyperelastic cases are given, respectively, by

$$\delta\sigma_{ij} = \frac{\partial f_{ij}\left(u_{ij}\right)}{\partial u_{k\ell}}\delta u_{k\ell} \tag{3.5}$$

$$\delta\sigma_{ij} = \frac{\partial^2 \mathcal{F}\left(u_{ij}\right)}{\partial u_{ij}\partial u_{k\ell}}\delta u_{k\ell} \tag{3.6}$$

The hierarchy of these definitions is illustrated in figure 3.1.

Kolymbas [80] adopts the hypoelastic approach in developing the theory of hypoplasticity, which proposes rate equations of the type given above (equation 3.4), and additionally dispenses with the usual strain decomposition (equation 3.1), taking the stress rate to be a function of the total strain rate, and declaring simply that "soil is not elastic" [81]. Furthermore, he outlines three reasons why elasticity is not appropriate for modeling granular materials:

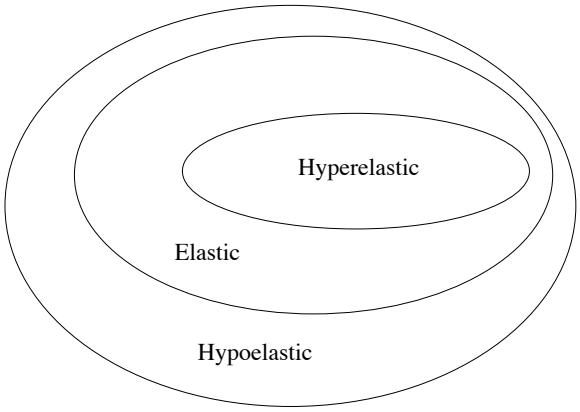

Figure 3.1. Hierarchy of elastic models.

1. It does not account for plastic yield.

2. It does not account for dilatancy/contractancy, i.e. coupled volume and shear deformations.

3. It does not account for stress-dependent stiffness

While this list of shortcomings certainly applies to *linear* elasticity, we will consider several hyperelastic models that predict all of the preceding behavior. Thus, this list of requirements certainly does not invalidate elastic, elasto-plastic, or hyperelastic models for granular materials. Furthermore, as hypoplasticity employs rate equations, it follows the evolution of stresses and strains with time, but the initial stress "has to be known or assumed" [80]. The initial or static stress distribution prior to plastic deformation is precisely the information that elasticity provides, and thus is better suited to this purpose than hypoplasticity, which was noted by Jiang and Liu [82]. Kolymbas does not consider elasticity appropriate for even the static stress calculation, but does not propose an alternative either.

Nevertheless, in many problems dealing with soils and granular materials, plastic deformations, which include irreversible rolling and sliding of particles, will far exceed elastic ones. If elasticity is appropriate for describing some classes of problems, we expect there to be at least a small range where elastic deformations dominate, i.e. where the deformation is predominantly reversible. This elastic regime has been identified in both experiments (e.g. [55]) and numerical simulations [83]. Difficulties have been noted in the case of shearing, in which some discrete element simulations suggest there are always irreversible shear deformations, leading some authors to conclude that all granular materials must be considered viscoelastic [84, 85]. Some types of loading, e.g. changes in direction of shear, are likely to always result in some changes to the particle contact network, and irreversible sliding, that are not elastic. But the major discrepancy here seems to appear when the inter-particle friction coefficient goes to zero, in which case discrete element simulations, but not the effective medium theory (EMT), predict a vanishing shear modulus. That elasticity is inappropriate for

materials that cannot sustain static shear is not a surprising conclusion, as this is essentially the definition of a fluid. For many cases in which both plastic and elastic deformations occur, viscoelasticity may be appropriate or necessary, but the viscous part is not necessary for static problems (see appendix A.2), and we may as well employ an elastic model, greatly simplifying the problem.

Others have questioned the continuum approach altogether, arguing that granular materials exhibit behavior that cannot be described by continuum mechanics. Many of these arguments have been motivated by the stress dip in sand piles, and arching. Some have proposed that stresses "propagate" in granular media along preferred directions, as if governed by hyperbolic, rather than elliptic, equations [22]. Goldenberg and Goldhirsch have shown in simulations that while this is true for small systems, there is a transition to elliptic behavior for larger systems [20, 86, 87]. That the constituent particles be large in number and small relative to the system size, of course, is the usual requirement of continuum mechanics. Put another way, there must exist a sufficiently large separation of micro and macro scales, and a representative volume element may be defined in which stresses and strains vary smoothly from one to the next. Rycroft and Kamrin [65, 88] find that for granular materials the size of this representative volume element may be as small as five particle diameters, validating the the use of continuum mechanics for such problems.

Perhaps the most convincing argument in favor of elasticity is the so-called "response function" of a granular layer to a point force perturbation. This will be discussed in detail in section 5.5; the measured response function is consistent with the elliptic equations of elasticity, and not the variously proposed hyperbolic models.

We will not concern ourselves further with any micro-scale problems. While there are clearly some difficulties in applying continuum mechanics and elasticity to some problems of granular physics, it does not appear to be an invalid approach altogether. An appropriate elastic model (i.e. one that successfully models experiment data) is a useful and simple tool in determining the static stress distribution.

3.2 Linear Elasticity Theory

In order to solve the force balance $\partial\sigma_{ij}/\partial x_j + \rho g_i = 0$, we require a constitutive equation that relates forces and displacements in a body. We will consider only cases in which the strains u_{ij} are small, in which case they are given in terms of the displacements U_i by the following [27]:

$$u_{ij} = \frac{1}{2}\left(\frac{\partial U_i}{\partial x_j} + \frac{\partial U_j}{\partial x_i}\right) \tag{3.7}$$

Elasticity implies reversible deformations, which change the internal energy $\mathcal{E}$ of the deformed body according to

$$d\mathcal{E} = TdS + \sigma_{ij}du_{ij} \tag{3.8}$$

a generalization of the familiar

$$d\mathcal{E} = TdS - PdV \tag{3.9}$$

for temperature T, entropy S, pressure P, and volume V. In hydrostatic compression, $\sigma_{ij} = -P\delta_{ij}$, and $\sigma_{ij}du_{ij} = -P\delta_{ij}du_{ij} = -Pdu_{ii}$; the sum u_{ii} is the relative volume change. Equivalently, we may consider the Helmholtz free energy $\mathcal{F}$, defined by

$$\mathcal{F} = \mathcal{E} - TS \tag{3.10}$$

and differential relation

$$d\mathcal{F} = -SdT + \sigma_{ij}du_{ij} \tag{3.11}$$

If there are no changes in temperature (or an analogous "granular temperature", [89, 90]),

$$\frac{d\mathcal{F}}{du_{ij}} = \sigma_{ij} \tag{3.12}$$

the stresses are given as derivatives of the Helmholtz free energy with respect to the strains. The constitutive behavior of a material, then, is completely specified by $\mathcal{F}(u_{ij})$. The question remains, what is the appropriate form of $\mathcal{F}(u_{ij})$? The linear elasticity theory assumes a reference state of zero strain at zero applied force, and since the strains are small, expands the free energy in a Taylor series about this point. The free energy is a scalar, and as such must be a function of scalar quantities. For an isotropic material, this means that it is a function of the strain invariants

$$u_{ii} = u_{11} + u_{22} + u_{33} \tag{3.13}$$

$$u_{ij}u_{ij} \equiv u_{11}^2 + u_{12}^2 + u_{13}^2 + u_{21}^2 + u_{22}^2 + u_{23}^2 + u_{31}^2 + u_{32}^2 + u_{33}^2 \tag{3.14}$$

$$u_{ij}u_{jk}u_{ki} = \det \mathbf{u} \tag{3.15}$$

Neglecting any higher (third) order terms,

$$\mathcal{F} = \mathcal{F}_0 + Cu_{ii} + \frac{1}{2}\lambda u_{ii}^2 + \mu u_{ij}u_{ij} \tag{3.16}$$

where $\mathcal{F}_0$, C, λ, and μ are constants. Since the energy must be a minimum at zero strain, we require

$$\frac{d\mathcal{F}}{du_{ij}} = 0 \tag{3.17}$$

and hence $C = 0$. Neglecting the free energy of the undeformed body $\mathcal{F}_0$,

$$\mathcal{F} = \frac{1}{2}\lambda u_{ii}^2 + \mu u_{ij}u_{ij} \tag{3.18}$$

It is more useful to consider the free energy in terms of volume changes, or pure compression, and shape changes, or pure shear; we may do so by instead defining

$$u_{ij}^0 \equiv u_{ij} - \frac{1}{3}u_{\ell\ell}\delta_{ij} \tag{3.19}$$

$$u_s^2 \equiv u_{ij}^0 u_{ij}^0 \tag{3.20}$$

$$\Delta \equiv -u_{ii} \tag{3.21}$$

Table 3.1. Mapping of tensor to matrix indices

Matrix	1	2	3	4	5	6
Tensor	11	22	33	12 & 21	23 & 32	13 & 31

$$K \equiv \lambda + \tfrac{2}{3}\mu \tag{3.22}$$

$$G \equiv \mu \tag{3.23}$$

referring generally to Δ as the "compression" and u_s as the "shear". The free energy is then given by

$$\mathcal{F} = \tfrac{1}{2}K\Delta^2 + Gu_s^2 \tag{3.24}$$

Since the free energy is quadratic in the strains, the stress-strain relationship will be linear:

$$\sigma_{ij} = \frac{\partial \mathcal{F}}{\partial u_{ij}} \tag{3.25}$$

with the incremental stress-strain relation given by

$$\delta\sigma_{ij} = M_{ijk\ell}\delta u_{k\ell} \tag{3.26}$$

where $M_{ijk\ell}$ is the stiffness tensor. As the stress and strain tensors are symmetric, we may re-index according to table 3.1 and write the system of six equations in the matrix notation

$$\begin{bmatrix} \delta\sigma_1 \\ \delta\sigma_2 \\ \delta\sigma_3 \\ \delta\tau_4 \\ \delta\tau_5 \\ \delta\tau_6 \end{bmatrix} = \begin{bmatrix} \frac{\partial^2\mathcal{F}}{\partial u_1^2} & \frac{\partial^2\mathcal{F}}{\partial u_1\partial u_2} & \frac{\partial^2\mathcal{F}}{\partial u_1\partial u_3} & \frac{\partial^2\mathcal{F}}{\partial u_1\partial\gamma_4} & \frac{\partial^2\mathcal{F}}{\partial u_1\partial\gamma_5} & \frac{\partial^2\mathcal{F}}{\partial u_1\partial\gamma_6} \\ \frac{\partial^2\mathcal{F}}{\partial u_2\partial u_1} & \frac{\partial^2\mathcal{F}}{\partial u_2^2} & \frac{\partial^2\mathcal{F}}{\partial u_2\partial u_3} & \frac{\partial^2\mathcal{F}}{\partial u_2\partial\gamma_4} & \frac{\partial^2\mathcal{F}}{\partial u_2\partial\gamma_5} & \frac{\partial^2\mathcal{F}}{\partial u_2\partial\gamma_6} \\ \frac{\partial^2\mathcal{F}}{\partial u_3\partial u_1} & \frac{\partial^2\mathcal{F}}{\partial u_3\partial u_2} & \frac{\partial^2\mathcal{F}}{\partial u_3^2} & \frac{\partial^2\mathcal{F}}{\partial u_3\partial\gamma_4} & \frac{\partial^2\mathcal{F}}{\partial u_3\partial\gamma_5} & \frac{\partial^2\mathcal{F}}{\partial u_3\partial\gamma_6} \\ \frac{\partial^2\mathcal{F}}{\partial\gamma_4\partial u_1} & \frac{\partial^2\mathcal{F}}{\partial\gamma_4\partial u_2} & \frac{\partial^2\mathcal{F}}{\partial\gamma_4\partial u_3} & \frac{\partial^2\mathcal{F}}{\partial\gamma_4^2} & \frac{\partial^2\mathcal{F}}{\partial\gamma_4\partial\gamma_5} & \frac{\partial^2\mathcal{F}}{\partial\gamma_4\partial\gamma_6} \\ \frac{\partial^2\mathcal{F}}{\partial\gamma_5\partial u_1} & \frac{\partial^2\mathcal{F}}{\partial\gamma_5\partial u_2} & \frac{\partial^2\mathcal{F}}{\partial\gamma_5\partial u_3} & \frac{\partial^2\mathcal{F}}{\partial\gamma_5\partial\gamma_4} & \frac{\partial^2\mathcal{F}}{\partial\gamma_5^2} & \frac{\partial^2\mathcal{F}}{\partial\gamma_5\partial\gamma_6} \\ \frac{\partial^2\mathcal{F}}{\partial\gamma_6\partial u_1} & \frac{\partial^2\mathcal{F}}{\partial\gamma_6\partial u_2} & \frac{\partial^2\mathcal{F}}{\partial\gamma_6\partial u_3} & \frac{\partial^2\mathcal{F}}{\partial\gamma_6\partial\gamma_4} & \frac{\partial^2\mathcal{F}}{\partial\gamma_6\partial\gamma_5} & \frac{\partial^2\mathcal{F}}{\partial\gamma_6^2} \end{bmatrix} \begin{bmatrix} \delta u_1 \\ \delta u_2 \\ \delta u_3 \\ \delta\gamma_4 \\ \delta\gamma_5 \\ \delta\gamma_6 \end{bmatrix} \tag{3.27}$$

where shear stresses are denoted by τ and the engineering shear strain $\gamma_i = 2u_i$. Since the free energy for linear elasticity is quadratic in the strains, the second derivatives that comprise the stiffness matrix M_{ij} are combinations of the constants K and G;

$$M_{ij} = \begin{bmatrix} K + \frac{4}{3}G & K - \frac{2}{3}G & K - \frac{2}{3}G & 0 & 0 & 0 \\ K - \frac{2}{3}G & K + \frac{4}{3}G & K - \frac{2}{3}G & 0 & 0 & 0 \\ K - \frac{2}{3}G & K - \frac{2}{3}G & K + \frac{4}{3}G & 0 & 0 & 0 \\ 0 & 0 & 0 & G & 0 & 0 \\ 0 & 0 & 0 & 0 & G & 0 \\ 0 & 0 & 0 & 0 & 0 & G \end{bmatrix} \tag{3.28}$$

It is apparent that the shear modulus, or ratio of shear stress to shear strain, is equal to G:

$$\frac{\delta\tau_i}{\delta\gamma_i} = G \tag{3.29}$$

In the absence of shear,

$$\tfrac{1}{3}\sigma_{ii} \equiv P = K\Delta \tag{3.30}$$

The bulk modulus given by the constant K.

There are thermodynamic restrictions on the values of K and G. Stability requires that the free energy $\mathcal{F}$ be a convex function of the strains [91], or

$$\frac{\partial^2\mathcal{F}}{\partial\Delta^2} \geq 0 \tag{3.31}$$

$$\frac{\partial^2\mathcal{F}}{\partial u_s^2} \geq 0 \tag{3.32}$$

$$\frac{\partial^2\mathcal{F}}{\partial\Delta^2}\frac{\partial^2\mathcal{F}}{\partial u_s^2} - \left(\frac{\partial^2\mathcal{F}}{\partial\Delta\partial u_s}\right)^2 \geq 0 \tag{3.33}$$

The first two require that K and G, respectively, are positive. The third condition, in this case, places no additional restrictions on K and G.

3.3 Granular Elasticity

We know that the elastic behavior of granular materials is not linear, and there have been many attempts to model it by taking the elastic moduli as functions of stress or strain. Zytynski et al. [66] were the first to point out a significant theoretical problem with such models; as they did not derive the elastic moduli from an appropriate free energy, the elastic response was not always conservative, with some models predicting continuous production of energy by materials subjected to a simple stress cycle (i.e. perpetual motion machines). An elastic constitutive relation must conserve energy, and hence follow from the free energy. We now consider some recently proposed free energies for granular materials, and their ability to predict experimental data.

The following free energy has been proposed and analyzed in a series of papers by Jiang and Liu [25, 63, 68–72]:

$$\mathcal{F} = \Delta^a\left(\tfrac{1}{2}\tilde{K}\Delta^2 + \tilde{G}u_s^2\right) \tag{3.34}$$

Here they have taken the free energy of isotropic linear elasticity and multiplied it by Δ^a. They take $a = 1/2$, consistent with "Hertz contacts", if not experimental data, and call this "granular elasticity", or GE. We shall leave a unspecified for the time being, and investigate different choices of a below. Here and throughout, tildes have been added to the constants K and G to distinguish them from the bulk and shear moduli. In linear elasticity, as was shown above, these constants *are* the bulk and shear moduli; but for any other form

of the free energy that is not quadratic in the strains, the quantities in the stiffness matrix that we identify as "elastic moduli" will not be constants, but will have some dependence on the strains.

In linear elasticity, the thermodynamic stability requirement that the free energy be a convex function of the strains established that $\tilde{K}$ and $\tilde{G}$ must be *positive* constants. Similarly, thermodynamic stability will place some constraints on the present model. For reasons that will become apparent, it is useful to define a dimensionless constant ξ,

$$\xi \equiv \frac{5\tilde{K}}{4\tilde{G}} \tag{3.35}$$

and rewrite the free energy as

$$\mathcal{F} = \tilde{G}\Delta^a \left(\tfrac{2}{5}\xi\Delta^2 + u_s^2\right) \tag{3.36}$$

The second derivatives are given by

$$\frac{\partial^2 \mathcal{F}}{\partial \Delta^2} = \tfrac{2}{5}\xi\tilde{G}(a+1)(a+2)\Delta^a + a(a-1)\Delta^{a-2}u_s^2 \tag{3.37}$$

$$\frac{\partial^2 \mathcal{F}}{\partial u_s^2} = 2\tilde{G}\Delta^a \tag{3.38}$$

$$\frac{\partial^2 \mathcal{F}}{\partial \Delta \partial u_s} = 2a\tilde{G}\Delta^{a-1}u_s \tag{3.39}$$

Recalling that $\Delta = -u_{ii}$ will be positive in compression, the second stability condition (equation 3.32) indicates $\tilde{G}$ is still a positive constant, but also that the material is not stable under tension; this is precisely the case for granular materials. The first stability condition (equation 3.31) is more complicated, and includes both terms Δ and u_s. It requires

$$\tfrac{2}{5}\xi\tilde{G}(a+1)(a+2)\Delta^a + \tilde{G}a(a-1)\Delta^{a-2}u_s^2 > 0 \tag{3.40}$$

or

$$\tfrac{2}{5}\xi\tilde{G}(a+1)(a+2) + \tilde{G}a(a-1)\frac{u_s^2}{\Delta^2} > 0 \tag{3.41}$$

Anticipating that $0 < a < 1$, the second of the two terms will be negative. The first, then, must be positive for this condition to hold at all, so ξ must also be positive. But it also implies a maximum stable ratio of shear to compressive strain:

$$\frac{u_s^2}{\Delta^2} < \frac{2\xi(a+1)(a+2)}{5a(1-a)} \tag{3.42}$$

The third stability condition (equation 3.33) is an even stricter requirement of this type:

$$\left(\tfrac{2}{5}\xi\tilde{G}(a+1)(a+2)\Delta^a + \tilde{G}a(a-1)\Delta^{a-2}u_s^2\right)\left(2\tilde{G}\Delta^a\right) > \left(2a\tilde{G}\Delta^{a-1}u_s\right)^2 \tag{3.43}$$

Canceling common terms,

$$\frac{2}{5}\xi(a+1)(a+2) + a(a-1)\frac{u_s^2}{\Delta^2} > 2a^2\frac{u_s^2}{\Delta^2} \tag{3.44}$$

and rearranging,

$$\frac{u_s^2}{\Delta^2}\left(2a^2 - a(a-1)\right) = \frac{u_s^2}{\Delta^2}a(a+1) < \frac{2}{5}\xi(a+1)(a+2) \tag{3.45}$$

or

$$\frac{u_s^2}{\Delta^2} < \frac{2\xi(a+2)}{5a} \tag{3.46}$$

What does this mean in terms of the stresses? The pressure and effective shear stress are given by

$$P \equiv \frac{\partial \mathcal{F}}{\partial \Delta} = \tfrac{2}{5}\tilde{G}\xi(a+2)\Delta^{a+1} + a\tilde{G}\frac{u_s^2}{\Delta^{1-a}} \tag{3.47}$$

$$\sigma_s \equiv \frac{\partial \mathcal{F}}{\partial u_s} = 2\tilde{G}\Delta^a u_s \tag{3.48}$$

At the loss of stability,

$$u_s = \Delta\sqrt{\frac{2\xi(a+2)}{5a}} \tag{3.49}$$

Substituting this into equations 3.47 and 3.48 gives

$$P = \tfrac{2}{5}\tilde{G}\xi(a+2)\Delta^{a+1} + a\tilde{G}\frac{\Delta^2\frac{2\xi(a+2)}{5a}}{\Delta^{1-a}} \tag{3.50}$$

$$\sigma_s = 2\tilde{G}\Delta^a\Delta\sqrt{\frac{2\xi(a+2)}{5a}} \tag{3.51}$$

or

$$P = \tfrac{4}{5}\tilde{G}\xi(a+2)\Delta^{a+1} \tag{3.52}$$

$$\Delta^{a+1} = \frac{\sigma_s}{\tilde{G}}\sqrt{\frac{5a}{8\xi(a+2)}} \tag{3.53}$$

Combining the two gives the stability limit in terms of the stresses,

$$\frac{\sigma_s}{P} = \sqrt{\frac{5}{2\xi a(a+2)}} \tag{3.54}$$

Remarkably, this is precisely the Drucker-Prager form of the Coulomb yield criterion (2.9), with the Coulomb angle ϕ_c defined by

$$\phi_c = \arctan\sqrt{\frac{5}{2\xi a(a+2)}} \tag{3.55}$$

Stress states violating this yield criterion are not merely inadmissible in this case, they are also inaccessible; there are no real solutions for

$$\frac{\sigma_s}{P} > \sqrt{\frac{5}{2\xi a(a+2)}} \tag{3.56}$$

To see why this is so, consider the stress paths for some constant value of Δ. Solving equation 3.48 for u_s and substituting into equation 3.47 gives

$$P = \tfrac{2}{5}\tilde{G}\xi(a+2)\Delta^{a+1} + \frac{a\sigma_s^2}{4\tilde{G}\Delta^{a+1}} \tag{3.57}$$

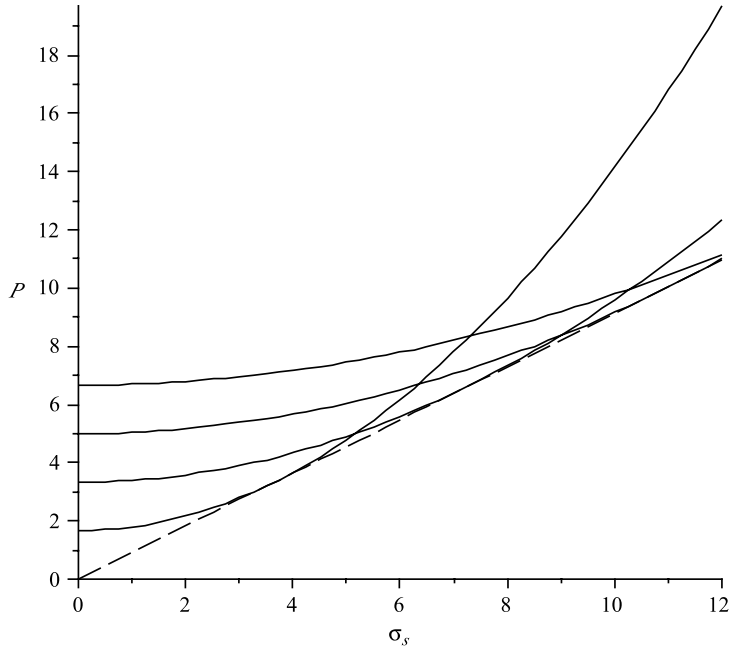

Figure 3.2. Stress paths for various values of $\tilde{G}\Delta^{a+1}$ (arbitrary units), illustrating the lack of solutions for $\sigma_s/P > \sqrt{5/(2\xi a(a+2))}$. Here $a = 1/2$ and $\xi = 5/3$.

The curves $P(\sigma_s)$ at constant Δ are parabolas (see Figure 3.2). The line beginning at the origin and tangent to the parabolic stress path intersects it at the maximum value of σ_s/P, (or, equivalently, the minimum value of P/σ_s). The slope at this point of intersection is given by

$$\frac{\partial P}{\partial \sigma_s} = \frac{a\sigma_s}{2\tilde{G}\Delta^{a+1}} \tag{3.58}$$

and the tangent line is then defined by

$$\frac{P}{\sigma_s} = \frac{a\sigma_s}{2\tilde{G}\Delta^{a+1}} \tag{3.59}$$

The two equations 3.57 and 3.59 are sufficient to solve for the two unknowns P and σ_s, which are

$$\sigma_s = \tilde{G}\Delta^{a+1}\sqrt{\frac{8\xi(a+2)}{5a}} \tag{3.60}$$

$$P = \frac{4}{5}\tilde{G}\xi(a+2)\Delta^{a+1} \tag{3.61}$$

or

$$\frac{\sigma_s}{P} = \sqrt{\frac{5}{2\xi a(a+2)}} \tag{3.62}$$

independent of Δ; the maximum attainable stress ratio along any path is the same as the limit for thermodynamic stability, equation 3.54.

Just as the pressure P and shear stress σ_s are no longer independent (as they are in linear elasticity), we might consider the relationship between Δ and u_s at constant pressure. This is obtained simply by rearranging equation 3.47, to get

$$u_s = \sqrt{\frac{1}{a}\left(\frac{P}{\tilde{G}}\right)\Delta^{1-a} - \frac{2\xi}{5a}(a+2)\Delta^2} \tag{3.63}$$

In this case, there are solutions for the strains that *are* thermodynamically inadmissible according to the stability condition, equation A.5. But in the stable regions, as indicated in Figure 3.3, increasing the shear u_s decreases the compression Δ; in other words, we also have shear dilatancy: shearing results in volume expansion, and eventually yield.

Thus, in adopting the hyperelastic formalism, and modifying the form of the free energy so as to account for the power law dependence of the elastic moduli on the stress (or strain), GE is able to describe many aspects of granular physics. Suitable values for the exponent a will be discussed at length below, but it is expected that a is not a material constant; a particular value of a should apply to an entire class of granular materials (say, cohesionless dry sands). So this form of the free energy, without really introducing any new material constants, predicts the following well known behavior of granular materials:

1. The inability to take tension

2. Yield, with a Coulomb condition limiting the shear

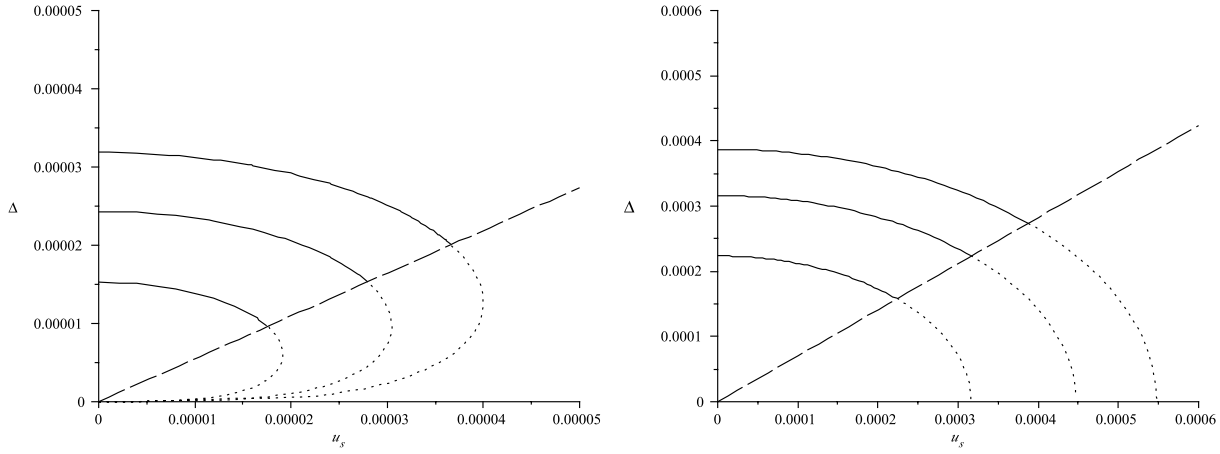

Figure 3.3. Strain paths for various values of $P/\tilde{G}$, with $\xi = 5/3$, and $a = 1/2$ (left) and $a = 1$ (right). Δ decreases (volume increases) with u_s in the stable region of each curve (solid lines). The dotted lines are thermodynamically unstable solutions.

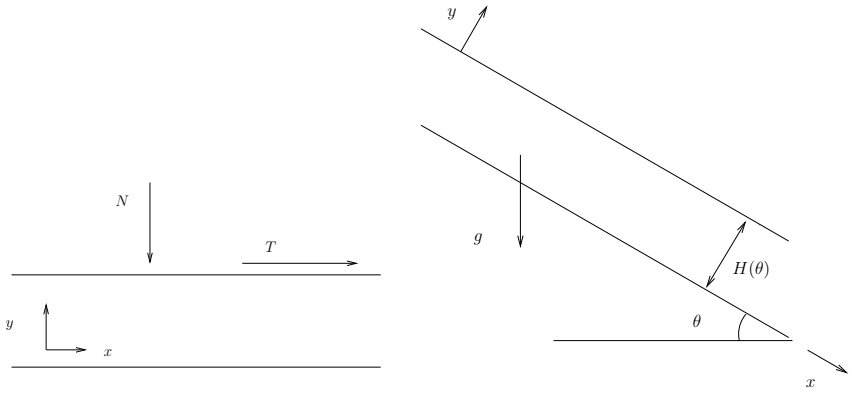

Figure 3.4. Left: infinite granular layer subject to normal force N and tangential force T. Right: infinite granular layer inclined at angle θ.

3. Reynolds dilatancy, the volume expansion that accompanies shear

This is a remarkable list of qualitative successes, given the simplicity of the approach. We now consider some analytical results to see how the theory performs quantitatively.

3.4 The Yield Angle

In a recent paper employing granular elasticity [58], the stress ratio σ_s/P was identified as the tangent of the Coulomb friction angle ϕ_c, but we have seen in section 2.1.1 that this Drucker-Prager parameter is *not* the Coulomb angle. Furthermore, the friction angle for the Drucker-Prager yield condition is not necessarily the angle of repose ϕ_y. In granular elasticity, the Drucker-Prager yield surface is a natural consequence of the thermodynamic stability requirement that the free energy be convex in the strains. Following Jiang and Liu [68], we consider two particular problems which give a definition of the yield angle for GE.

Consider the following two simple cases [68], whose solutions we will find to be identical. The first is a granular layer, infinite in two directions (Figure 3.4), subjected to a normal force N and shearing force T at its surface. The second is a similar layer, also infinite in extent, subject to gravity and inclined at an angle θ. In both cases, we are left with only two non-zero components of the strain, one normal and one shear, say u_2 and γ_4. In the first case, in which the only applied forces are the two at the surface, the stresses and strains will be uniform throughout the layer. Their constant values are given by the constitutive relation, equation 3.36. With u_1, u_3, γ_5, and γ_6 all equal to zero, the equations for the stresses become

$$\sigma_2 = \frac{\partial \mathcal{F}}{\partial u_2} = -\tilde{G}\left(-u_2\right)^{a+1}\left(\frac{a}{2}\frac{\gamma_4^2}{u_2^2} + (a+2)\left(\frac{2}{5}\xi + \frac{2}{3}\right)\right) \tag{3.64}$$

$$\tau_4 = \frac{\partial \mathcal{F}}{\partial \gamma_4} = \tilde{G}\left(-u_2\right)^{a}\gamma_4 \tag{3.65}$$

In the first case, $\sigma_2 = -N$, and $\tau_4 = T$ throughout the layer. For the inclined layer, the above stress-strain relations hold, but they vary spatially. It is then necessary to solve the force balance,

$$\frac{d\sigma_{yy}}{dy} = \frac{d\sigma_2}{dy} = -\rho g \cos\theta \tag{3.66}$$

$$\frac{d\sigma_{xy}}{dy} = \frac{d\tau_4}{dy} = \rho g \sin\theta \tag{3.67}$$

Integrating with respect to y,

$$\sigma_2 = -gM(y)\cos\theta \tag{3.68}$$

$$\tau_4 = gM(y)\sin\theta \tag{3.69}$$

where

$$M(y) \equiv \int_y^H \rho(y')dy' \tag{3.70}$$

is the mass per unit area between y and the free surface at H. $M(y)$ is not a function of the angle of the layer, θ, so we may write

$$\tan\theta = \frac{\tau_4}{-\sigma_2} = \frac{T}{-N} \tag{3.71}$$

From the equations 3.64 and 3.65,

$$\tan\theta = \frac{\dfrac{\gamma_4}{-u_2}}{\dfrac{2}{5}\xi\,(a+2) + \dfrac{1}{2}a\dfrac{\gamma_4^2}{u_2^2} + \dfrac{\dfrac{2}{3}a^2 + 2a + \dfrac{4}{3}}{a+1}} \tag{3.72}$$

So, we have the angle θ as a function of the strain ratio γ_4/u_2, the exponent a, and the material constant ξ. We identify the angle of repose as the value of θ at which there are no solutions, or no thermodynamically stable solutions, for the strains. Recall that we have a stability condition on the strain ratio,

$$\frac{u_s^2}{\Delta^2} < \frac{2\xi(a+2)}{5a} \tag{3.73}$$

which simplifies, in the present case, to

$$\frac{\gamma_4^2}{u_2^2} < \frac{4\xi(a+2)}{5a} - \frac{4}{3} \tag{3.74}$$

since

$$\Delta = -u_2 \tag{3.75}$$

and

$$u_s^2 = \tfrac{2}{3}u_2^2 + \tfrac{1}{2}\gamma_4^2 \tag{3.76}$$

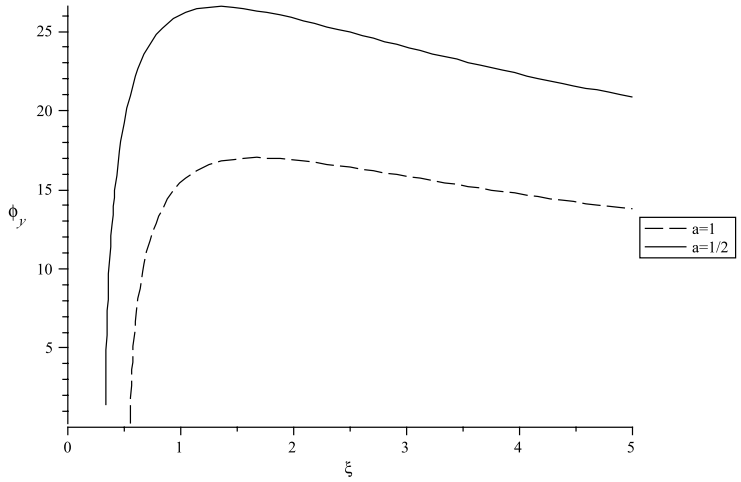

Figure 3.5. The yield angle ϕ_y for GE as a function of ξ. The maximum occurs at $\sim 25.5°$ for $a = 1/2$ and $\sim 17°$ for $a = 1$.

Substituting this critical value of the strain ratio into equation 3.72 gives the angle of repose ϕ_y in terms of only the constants a and ξ:

$$\tan\phi_y = \frac{\sqrt{\dfrac{4\xi\,(a+2)}{5a} - \dfrac{4}{3}}}{\dfrac{2}{5}\xi\,(a+2) + \dfrac{1}{2}a\left(\dfrac{4\xi\,(a+2)}{5a} - \dfrac{4}{3}\right) + \dfrac{\dfrac{2}{3}a^2 + 2a + \dfrac{4}{3}}{a+1}} \tag{3.77}$$

which simplifies to

$$\tan\phi_y = \frac{\sqrt{\dfrac{\xi\,(a+2)}{5a} - \dfrac{1}{3}}}{\dfrac{2}{5}\xi\,(a+2) + \dfrac{2}{3}} \tag{3.78}$$

So, ϕ_y is no longer a third material constant, but is given here in terms of the other material constants, a requirement for thermodynamic stability. This is a satisfying physical description of the problem, but it is also a significant practical advantage for the modeler. Rather than having to postulate the values of $\tilde{K}$ and $\tilde{G}$, or determine them at great expense through triaxial tests or something similar, one may conduct simple experiments to determine ϕ_y, and back out the value of ξ employing the equation above. ξ fixes the ratio of $\tilde{K}$ and $\tilde{G}$, so one of them must be determined via some other means if it is important to know the magnitude of the strains, but the ratio ξ alone is sufficient to predict the onset of yield.

Of course, we must also pick a value for the exponent a, and it is apparent from equation 3.78 that the yield angle depends on a. But we do not expect a to differ much from one material to the next; as discussed previously, it reflects the changing contact area between discrete particles when stressed. The Hertz theory for spheres suggests $a = 1/2$, while a large body of experimental evidence suggests $a \sim 1$. Consider, then, $\phi_y(\xi)$ for $a = 1/2$ and $a = 1$, shown in Figure 3.5. Equation 3.78 simplifies to

$$\phi_y = \arctan\left(\frac{\sqrt{\xi - \frac{1}{3}}}{\xi + \frac{2}{3}}\right) \tag{3.79}$$

for $a = 1/2$ and

$$\phi_y = \arctan\left(\frac{\sqrt{\frac{3}{5}\xi - \frac{1}{3}}}{\frac{6}{5}\xi + \frac{2}{3}}\right) \tag{3.80}$$

for $a = 1$. The peculiar feature of these curves is that they have a maximum; for GE ($a = 1/2$) it occurs at $\xi = 4/3$, $\phi_y \approx 25.5°$. So no matter what the material constants $\tilde{K}$ and $\tilde{G}$ are, granular elasticity predicts a yield angle that is, at most, 25.5°. As we have seen, yield angles for most materials are around 30-35°; thus yield, the remarkable qualitative feature of GE, possesses a significant quantitative discrepancy with real materials.

While the choice of $a = 1/2$ is motivated by the Hertz theory, we have also seen that real granular materials, except at high pressures [77], generally have elastic moduli varying as $P^{1/2}$, implying $a \sim 1$. We shall subsequently refer to this case as GE-C, for "granular elasticity - cubic", since the free energy is a cubic function of the strains:

$$\mathcal{F} = \frac{2}{5}\xi\tilde{G}\Delta^3 + \tilde{G}\Delta u_s^2 \tag{3.81}$$

In this case, $\phi_y(\xi)$ has a similar shape, but shifts to even lower values of ϕ_y, with a maximum at $\xi = 5/3$, $\phi_y \approx 17°$. The peak in the curve, as a function of a, can be determined by solving for ξ at the maximum, $\partial\phi_y/\partial\xi = 0$, with

$$\xi_{max} = \frac{5(1+2a)}{3(a+2)} \tag{3.82}$$

and the value of the maximum yield angle given by

$$\phi_{y,max} = \arctan\left(\frac{1}{4}\sqrt{\frac{3}{a(a+1)}}\right) \tag{3.83}$$

We see in Figure 3.6 that $\phi_{y,max}$ is a decreasing function of a. Thus, in employing GE/GE-C, one is forced to make a rather unpleasant choice; take $a \sim 1/4$, say, to allow for realistic yield angles (a maximum of $\sim 37.76°$ in that case), but contrary to what we know about the pressure dependence of the elastic moduli, or take $a \sim 1$ to match the latter, implying sand piles cannot be stable if steeper than $\sim 17°$. $a = 1/2$ is something of a compromise in that regard; Jiang and Liu mention that the chosen form "oversimplifies" [68]. They have, however, suggested two ways in which one might generalize the theory to resolve the discrepancy, which we consider below.

3.5 Generalizing the Granular Elasticity Theory

While the qualitative successes of granular elasticity are remarkable, we have seen that quantitatively, there is a contradiction; choosing a power law form of the free energy to match the widely observed scaling of the elastic moduli with pressure results in unrealistically low yield angles. Conversely, choosing the power

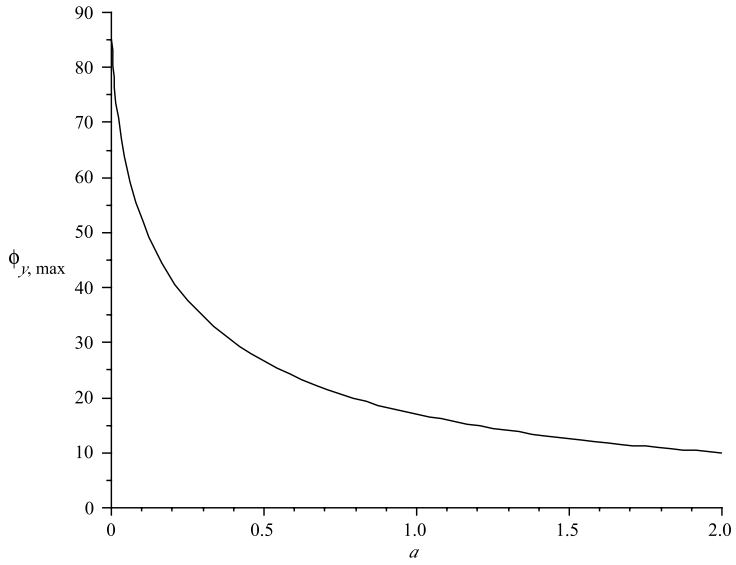

Figure 3.6. The maximum yield angle for GE, a decreasing function of a.

law to give an appropriate range of yield angles gives a much weaker dependence of the moduli on pressure than is observed. Jiang and Liu have proposed two possible generalizations of granular elasticity to rectify this difficulty, though they pursue neither; both will be considered here.

3.5.1 Differing dependence of bulk and shear moduli on compression

Originally, Jiang and Liu considered the following more general form for the free energy [68]:

$$\mathcal{F} = \tfrac{1}{2}\tilde{K}\Delta^{b+2} + \tilde{G}\Delta^{a}u_s^2 \tag{3.84}$$

of which granular elasticity is the special case $a = b = 1/2$. This gives the freedom to choose $a < 1/2$ in an attempt to allow higher yield angles, and $b = 1$ such that, for isotropic compression, the bulk modulus has the desired $P^{1/2}$ dependence. First, consider the effect on the stability condition,

$$\left(\frac{\partial^2\mathcal{F}}{\partial\Delta^2}\right)\left(\frac{\partial^2\mathcal{F}}{\partial u_s^2}\right) - \left(\frac{\partial^2\mathcal{F}}{\partial\Delta\partial u_s}\right)^2 \geq 0 \tag{3.85}$$

Now we have

$$\frac{\partial^2\mathcal{F}}{\partial\Delta^2} = \tfrac{1}{2}(b+1)(b+2)\tilde{K}\Delta^{b} + \tilde{G}a(a-1)\Delta^{a-2}u_s^2 \tag{3.86}$$

$$\frac{\partial^2\mathcal{F}}{\partial u_s^2} = 2\tilde{G}\Delta^{a} \tag{3.87}$$

$$\frac{\partial^2\mathcal{F}}{\partial\Delta\partial u_s} = 2\tilde{G}a\Delta^{a-1}u_s \tag{3.88}$$

and the stability condition simplifies to

$$\frac{u_s^2}{\Delta^2} \leq \frac{(b+1)(b+2)\tilde{K}}{2a(a+1)\tilde{G}}\Delta^{b-a} \tag{3.89}$$

The presence of the term Δ^{b-a} on the right hand side means the limiting stress ratio is no longer constant, but depends on the compression Δ; so the Drucker-Prager yield condition of GE is lost. Taking $a \neq b$ here will also result in the effective shear and bulk moduli having different dependence on the pressure, but as we will see in greater detail, both moduli usually have the same dependence on pressure (see, e.g., [55]).

Most importantly, for any anisotropic stress state (i.e. $u_s \neq 0$), this modification will not achieve the desired $P^{1/2}$ $\left(\Delta^1\right)$ dependence of the elastic moduli. While $b = 1$ ensures this relationship for isotropic stress, recall that we require $a < 1/2$ for realistic yield angles. If $u_s \neq 0$, this term will have a lower order dependence on the strains than the "bulk" term, and since the strains are small, the shear term will dominate, and the result will remain $K, G \sim u_{ij}^a \sim P^{\frac{a}{a+1}}$.

3.5.2 Incorporating dependence on the third strain invariant

Relaxing the requirement that $a = b$ clearly was not helpful in generalizing GE to capture both the observed nonlinearity in the elastic moduli and the observed range of yield angles; we must seek another

way. In a more recent paper [63], Jiang and Liu note that GE is a special case of the general form proposed by Goddard [77]:

$$\mathcal{F} = \Delta^{a+2} f\left(\frac{u_s^2}{\Delta^2}, \frac{u_{III}^3}{\Delta^3}\right) \tag{3.90}$$

where f is an arbitrary function, and u_{III}^3 is the third invariant of the (deviatoric) strain tensor,

$$u_{III}^3 \equiv u_{ij}^0 u_{jk}^0 u_{ki}^0 \equiv det\left(\underline{\underline{\mathbf{u}}}^0\right) \tag{3.91}$$

For GE, $a = 1/2$ and f is given by

$$f = \tilde{G}\left(\frac{2}{5}\xi + \frac{u_s}{\Delta^2}\right) \tag{3.92}$$

A logical extension that incorporates the third invariant is

$$f = \tilde{G}\left(\frac{2}{5}\xi + \frac{u_S}{\Delta^2} + \zeta\frac{u_{III}^3}{\Delta^3}\right) \tag{3.93}$$

where ζ is another dimensionless constant; we anticipate, then, that the yield angle will be given in terms of two constants ζ and ξ, potentially resulting in a larger range of allowable values. With $a = 1$, the free energy is now given by

$$\mathcal{F} = \tilde{G}\left(\frac{2}{5}\xi\Delta^3 + \Delta u_s^2 + \zeta u_{III}^3\right) \tag{3.94}$$

With the free energy given in terms of three, rather than just two, tensor invariants, we expect this will introduce more stability conditions of the type given in equations 3.31-3.33. But as with $u_s \equiv \sqrt{u_{ij}^0 u_{ij}^0}$, the transformation $u_{III} \equiv \sqrt[3]{u_{ij}^0 u_{jk}^0 u_{ki}^0}$ is not linear. In lieu of a coordinate transformation of the type given in [63] that would establish the general stability conditions explicitly, we may simply derive the stiffness matrix, set u_1, u_3, γ_5, and γ_6 equal to zero, and solve for the eigenvalues, to establish the stability limits for the infinite plane problem (see appendix C). The results are the following two stability conditions:

$$\frac{\gamma_4^2}{u_2^2} \leq \frac{8(-\zeta^2 + 3\zeta + 18)}{9\zeta^2} \tag{3.95}$$

$$\frac{\gamma_4^2}{u_2^2} \leq \frac{8(-3\zeta^2\xi - 5\zeta - 15 + 27\xi)}{9(2\zeta^2\xi + 5\zeta + 10)} \tag{3.96}$$

First we must establish which of these is the more stringent condition. As the value of γ_4^2/u_2^2 cannot be negative, and ξ and ζ are positive constants, we can first establish some limits on their values to ensure real solutions. The first condition does not depend on ξ at all, and it is clear that for the right hand side to be greater than zero, $\zeta < 6$. The second condition further requires that

$$-3\zeta^2\xi - 5\zeta - 15 + 27\xi > 0 \tag{3.97}$$

or

$$\xi(27 - 3\zeta^2) > 5\zeta + 15 \tag{3.98}$$

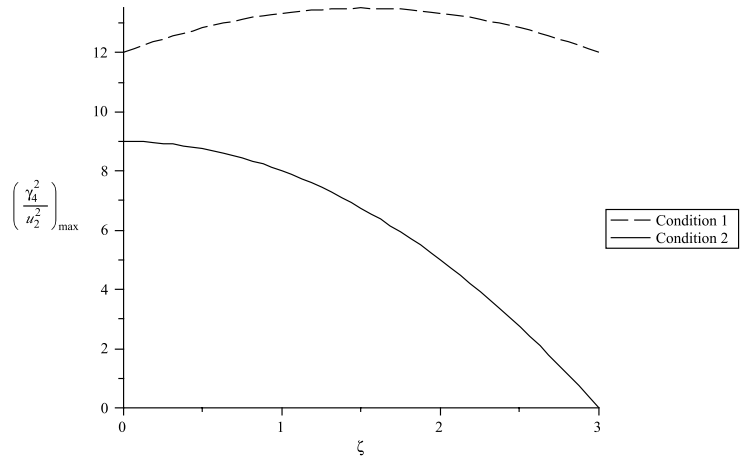

Figure 3.7. Maximum stable value of γ_4^2/u_2^2 for the two stability criteria, equations 3.102-3.103, in the limit $\xi \to \infty$. Stability is lost at condition two before ever reaching condition one.

Regardless of the value of ξ, this can only be satisfied for $\zeta < 3$; for larger values, the left hand side will be negative. Then we can also write

$$\xi > \frac{5\zeta + 15}{27 - 3\zeta^2} \tag{3.99}$$

In order to establish which of the two stability criteria is more severe, we shall first maximize the second with respect to ξ. Since

$$\frac{\partial}{\partial \xi}\left(\frac{8(-3\zeta^2\xi - 5\zeta - 15 + 27\xi)}{9(2\zeta^2\xi + 5\zeta + 10)}\right) = \frac{40(-\zeta^3 + 27\zeta + 54)}{9(2\zeta^2\xi + 5\zeta + 10)^2} \tag{3.100}$$

which is positive for $0 < \zeta < 3$, the second stability condition is an increasing function of ξ. There is no upper bound on the value of ξ, and

$$\lim_{\xi \to \infty}\left(\frac{8(-3\zeta^2\xi - 5\zeta - 15 + 27\xi)}{9(2\zeta^2\xi + 5\zeta + 10)}\right) = \frac{4(9 - \zeta^2)}{3\zeta^2} \tag{3.101}$$

So, having chosen ξ to make condition two as lenient as possible, we may rewrite the two conditions as follows:

$$\frac{3\zeta^2}{4}\frac{\gamma_4^2}{u_2^2} \leq (-\tfrac{2}{3}\zeta^2 + 2\zeta + 12) \tag{3.102}$$

$$\frac{3\zeta^2}{4}\frac{\gamma_4^2}{u_2^2} \leq (9 - \zeta^2) \tag{3.103}$$

Figure 3.7 shows that the second condition is more restrictive of the two, even in the limit $\xi \to \infty$. Identifying once again the ratio of shear to normal forces as the tangent of the yield angle, and substituting the stability condition 3.96 for the ratio of shear to normal strain (see appendix C), we arrive at an expression for the yield angle in terms of the two constants ξ and ζ:

$$\phi_y = \arctan\left(\frac{\sqrt{\left(\zeta^2\xi + \frac{5}{2}\zeta + 5\right)\left(\frac{1}{6}\zeta - 1\right)^2(-3\zeta^2\xi - 5\zeta - 15 + 27\xi)}}{\frac{9}{5}\zeta^2\xi^2 + 3\zeta\xi + 18\xi + 2\zeta^2\xi + 5\zeta + 10 - \frac{1}{6}\zeta^3\xi - \frac{5}{9}\zeta^2}\right) \tag{3.104}$$

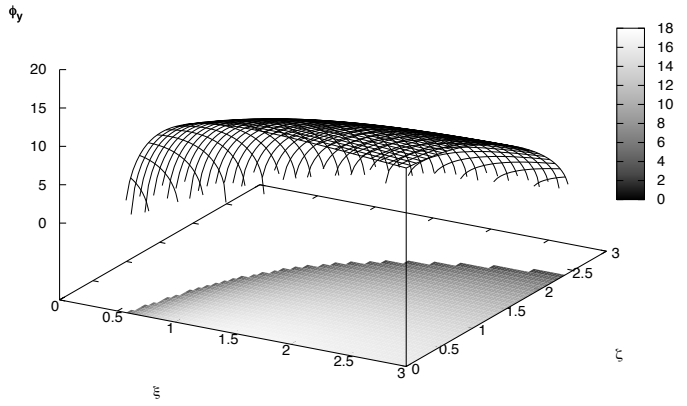

Figure 3.8. The yield angle ϕ_y as a function of the constants ξ and ζ. ϕ_y decreases rapidly with ζ.

For $\zeta = 0$, this simplifies to the relationship obtained from GE-C:

$$\phi_y = \arctan\left(\frac{\sqrt{\frac{3}{5}\xi - \frac{1}{3}}}{\frac{6}{5}\xi + \frac{2}{3}}\right) \tag{3.105}$$

Recall that GE-C has a maximum yield angle of $\sim 17^\circ$ at $\xi = 5/3$. Unfortunately, the preceding generalization does not allow for higher yield angles. Figure 3.8 shows the yield angle as a function of ξ and ζ. The familiar shape of $\phi_y(\xi)$ from GE/GE-C is apparent on the $\zeta = 0$ axis, but taking non-zero values of ζ only decreases the maximum yield angle. The peak of the surface $\phi_y(\xi, \zeta)$ occurs at $\xi = 5/3$, $\zeta = 0$ with the maximum yield angle still approximately equal to 17°.

3.5.3 A nonlinear shear model

Drawing ideas from both of the previous models, we shall investigate a potential of the form

$$\mathcal{F} = \tilde{G}\Delta^{b+2}\left(\frac{2}{5}\xi + \left(\frac{u_s^2}{\Delta^2}\right)^c\right) \tag{3.106}$$

which is equivalent to

$$\mathcal{F} = \tilde{G}\left(\tfrac{2}{5}\xi\Delta^{b+2} + \Delta^a u_s^{b-a+2}\right) \tag{3.107}$$

with $a \equiv b+2-2c$. This retains the flexibility of two power laws, but combines them in a way consistent with the form proposed by Goddard (equation 3.90). Both terms are of order $b+2$ in the strains, but the second term has a variable power law dependence on both the compression and the shear strain, implying a nonlinear relationship between shear stress and shear strain. This approach maintains the Coulomb condition, though as a more complicated function of both exponents a and b. As previously, it is given by the cross convexity

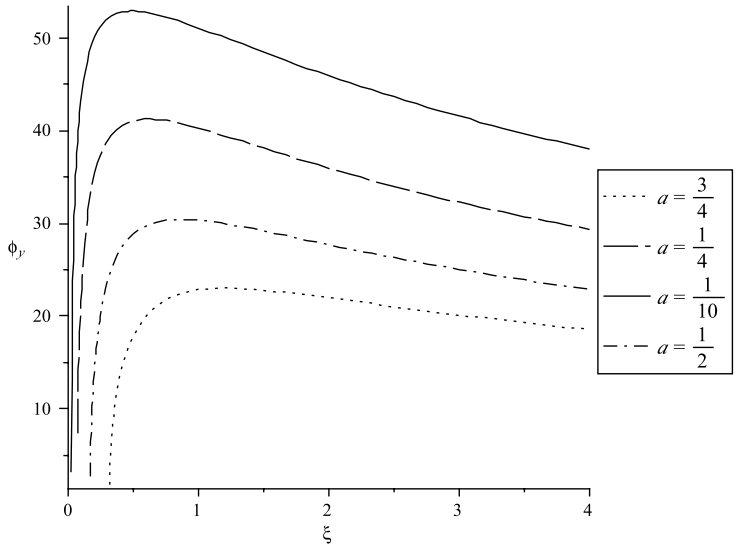

Figure 3.9. The yield angle for GE-NLS, for various values of a. As in GE, there is maximum value of ϕ_y, which decreases with a.

condition,

$$\left(\frac{\partial^2 \mathcal{F}}{\partial \Delta^2}\right)\left(\frac{\partial^2 \mathcal{F}}{\partial u_s^2}\right) - \left(\frac{\partial^2 \mathcal{F}}{\partial \Delta \partial u_s}\right)^2 \geq 0 \tag{3.108}$$

which for the new potential (equation 3.106) gives

$$\frac{u_s}{\Delta} \leq \left(\frac{2\xi(b+2)(b-a+1)}{5a}\right)^{\frac{1}{b-a+2}} \tag{3.109}$$

An expression for the yield angle is obtained just as in section 3.3, solving the plane problem and applying the new stability condition. Defining

$$\hat{\xi} \equiv \frac{2\xi(b+2)(b-a+1)}{5a} \tag{3.110}$$

$$\phi_y = \arctan\left(\frac{\sqrt{\frac{1}{2}\hat{\xi}^{\left(\frac{2}{b-a+2}\right)} - \frac{1}{3}}}{\frac{a}{b-a+2}\left(\frac{1}{b-a+1}\hat{\xi}^{\left(\frac{2}{b-a+2}\right)} + \hat{\xi}\right) + \frac{2}{3}}\right) \tag{3.111}$$

For $a = b$, the general GE form (equation 3.78) is recovered. Now, we may let $b = 1$, consistent with experimental data; we are still free to choose a value of a that gives a realistic range of yield angles. The yield angle as a function of ξ is given for several values of a in figure 3.9. It should be emphasized that our criterion for choosing a is the *maximum* theoretical yield angle, not the yield angle itself, which will take different values for different materials, and is determined by the material constant ξ. There is not a closed form solution for $\phi_{y,max}(a)$, though the trend is apparent from figure 3.9; $a = b = 1$ gives the same curve as GE-C, with a maximum of about 17°, and the maximum increases with decreasing a to 90° for $a = 0$. Figure 3.9 shows that $a = 1/4$ gives a maximum slightly over 40°, a reasonable choice.

So beginning from the free energy, equation 3.106, we have set the exponent b to match the known pressure dependence of the elastic moduli, and set a based on a theoretical maximum yield angle. $a = 1/4$ implies that no material may have a yield angle greater than $\sim 41°$. The actual yield angle for a given material gives the material constant ξ, and the remaining material constant $\tilde{G}$ is just a scale factor, and does not impact the stress or strain ratio. The non-linear shear model (GE-NLS) appears, then, to successfully generalize GE in the desired fashion. Unfortunately, it also has significant drawbacks, and seems to predict unphysical behavior in many situations. The form of the stiffness matrix is complicated, and none of the 36 terms in M are zero; they all depend on the shear strain. The nonlinear relationship between shear stress and shear strain results in a shear modulus that is a power law function of not only the compression, but also the shear strain u_s. Thus, in the absence of shear (i.e. pure (isotropic) compression), the shear modulus is zero. In this case M is singular,

$$M = \begin{bmatrix} K & K & K & 0 & 0 & 0 \\ K & K & K & 0 & 0 & 0 \\ K & K & K & 0 & 0 & 0 \\ 0 & 0 & 0 & 0 & 0 & 0 \\ 0 & 0 & 0 & 0 & 0 & 0 \\ 0 & 0 & 0 & 0 & 0 & 0 \end{bmatrix} \tag{3.112}$$

where the bulk modulus K is given by

$$K = \frac{2}{5}\xi\tilde{G}(b+1)(b+2)\Delta^b \tag{3.113}$$

According to the standard relationships between the various elastic constants,

$$E = \frac{9KG}{3K+G} \tag{3.114}$$

$$\nu = \frac{3K-2G}{2(3K+G)} \tag{3.115}$$

$G = 0$ implies a Young's modulus $E = 0$, and Poisson's ratio $\nu = 1/2$. The latter is typically associated with "incompressibility", i.e. a diverging bulk modulus, but it is evident in equation 3.113 that the bulk modulus is well defined here; the vanishing shear modulus is what gives $\nu = 1/2$ in this case (see [92] for some more interpretation of this issue).

The vanishing shear modulus at isotropic compression in GE-NLS results in a stiffness matrix that is singular there. This presents numerical difficulties, particularly when the inverse (compliance) matrix is needed, as it will be in subsequent sections. This will result in some rather unphysical behavior, and there really is no experimental support for vanishing shear and Young's moduli at isotropic compression, or a shear modulus that is a power law function of the shear (see, e.g., [57], and section 4.3.3). So while GE-NLS does allow for realistic yield angles, in light of these difficulties and the cumbersome nature of the governing equations, it is unlikely that this model is the best choice for modeling granular statics.

3.6 The Gibbs Free Energy in Elasticity

Thr rigorous thermodynamic approach to modeling nonlinear elasticity in granular materials has also found favor in the geotechnical engineering community. Zytynski and colleagues [66] noted in 1978 that many elastic models employed at the time did not conserve energy. Energy conservation, of course, is guaranteed in the hyperelastic formulation, which begins with the elastic energy potential. Elastic potentials appropriate for clays (in which the elastic moduli are taken to vary linearly with pressure) have been investigated by Houlsby [93] and Borja et al. [94], among others, and a general thermodynamic approach to modeling both elasticity and plasticity, logically termed "hyperplasticity", has been formulated by Collins and Houlsby [74] and later by Houlsby and Puzrin [67, 75]. Hyperelastic forms suitable for our present purposes have been proposed recently by Houlsby, Amorosi, and Rojas [76] and Einav and Puzrin [73], and will be considered in what follows.

3.6.1 Thermodynamic potentials and the Legendre transform

One difficulty of GE and its variants considered above is the fact that the elastic moduli are given as functions of the strains. Experiments invariably describe elastic moduli as functions of stress or pressure. This problem is not unique to elasticity; it is often preferred to take temperature and pressure as independent variables. This suggests we begin instead with the Gibbs free energy, whose variables are temperature and pressure. The change of independent variables is accomplished via the Legendre transform. More comprehensive discussions of the transform and its properties are given in [91] and [67]; we simply state here that for complementary potentials $X(x_i)$ and $Y(y_i)$, where

$$y_i = \frac{\partial X}{\partial x_i} \tag{3.116}$$

and

$$x_i = \frac{\partial Y}{\partial y_i} \tag{3.117}$$

the potentials are related by

$$X(x_i) + Y(y_i) = x_i y_i \tag{3.118}$$

Our presentation of the elasticity theory in section 3.2 gave the Helmholtz free energy as a Taylor series in the strains, but the linear elastic material also possesses a Gibbs free energy from which the identical constitutive behavior can be derived [67, 95]. Recall that the Helmholtz free energy for linear elasticity is given by

$$\mathcal{F} = \tfrac{1}{2} K \Delta^2 + G u_s^2 \tag{3.119}$$

with

$$P = \frac{-\sigma_{ii}}{3} = \frac{\partial \mathcal{F}}{\partial \Delta} \tag{3.120}$$

and

$$\sigma_s = \frac{\partial \mathcal{F}}{\partial u_s} \tag{3.121}$$

We seek the negative Gibbs free energy $\mathcal{G}$, such that

$$\Delta = \frac{\partial \mathcal{G}}{\partial P} \tag{3.122}$$

and

$$u_s = \frac{\partial \mathcal{G}}{\partial \sigma_s} \tag{3.123}$$

According to the Legendre transform, equation 3.118,

$$\mathcal{G} = P\Delta + \sigma_s u_s - \mathcal{F} = P\Delta + \sigma_s u_s - \tfrac{1}{2}K\Delta^2 - Gu_s^2 \tag{3.124}$$

and equations 3.120 and 3.121 give

$$P = K\Delta \tag{3.125}$$

and

$$\sigma_s = 2Gu_s \tag{3.126}$$

Solving these for Δ and u_s,

$$\Delta = \frac{P}{K} \tag{3.127}$$

$$u_s = \frac{\sigma_s}{2G} \tag{3.128}$$

and substituting into equation 3.124 gives

$$\mathcal{G} = \frac{P^2}{K} + \frac{\sigma_s^2}{2G} - \frac{1}{2}K\frac{P^2}{K^2} - G\frac{\sigma_s^2}{4G^2} \tag{3.129}$$

or

$$\mathcal{G} = \frac{P^2}{2K} + \frac{\sigma_s^2}{4G} \tag{3.130}$$

The second derivative of $\mathcal{G}$ with respect to the components of stress gives the compliance tensor, and the full incremental relation is

$$\begin{bmatrix} \delta u_1 \\ \delta u_2 \\ \delta u_3 \\ \delta \gamma_4 \\ \delta \gamma_5 \\ \delta \gamma_6 \end{bmatrix} = \begin{bmatrix} \frac{1}{E} & -\frac{\nu}{E} & -\frac{\nu}{E} & 0 & 0 & 0 \\ -\frac{\nu}{E} & \frac{1}{E} & -\frac{\nu}{E} & 0 & 0 & 0 \\ -\frac{\nu}{E} & -\frac{\nu}{E} & \frac{1}{E} & 0 & 0 & 0 \\ 0 & 0 & 0 & \frac{1}{G} & 0 & 0 \\ 0 & 0 & 0 & 0 & \frac{1}{G} & 0 \\ 0 & 0 & 0 & 0 & 0 & \frac{1}{G} \end{bmatrix} \begin{bmatrix} \delta \sigma_1 \\ \delta \sigma_2 \\ \delta \sigma_3 \\ \delta \tau_4 \\ \delta \tau_5 \\ \delta \tau_6 \end{bmatrix} \tag{3.131}$$

where Young's modulus E and Poisson's ratio ν are defined in terms of the bulk modulus K and shear modulus G by equations 3.114-3.115.

The transformation is straightforward for linear elasticity, but this is not generally the case; for example, there is no closed form solution for the Gibbs free energy in granular elasticity.

3.6.2 Model of Einav and Puzrin

Though the Gibbs free energy cannot be obtained from GE, we might apply similar arguments and propose a modification of the Gibbs free energy of linear elasticity. An analogous form is

$$\mathcal{G} = \frac{P^{2-m}}{B^{1-m}}\left(\beta + \frac{\sigma_s^2}{P^2}\right) \tag{3.132}$$

A potential of this type was considered by Einav and Puzrin (EP), who focused on the case $m = 1$ for clays; for dry granular materials, we will instead prefer $m = 1/2$, such that

$$\mathcal{G} = \sqrt{\frac{P^3}{B}}\left(\beta + \frac{\sigma_s^2}{P^2}\right) \tag{3.133}$$

where the constant β is dimensionless, and B has units of pressure. The elements of the compliance matrix will have a $P^{-\frac{1}{2}}$ dependence, and the corresponding elastic moduli will have the familiar $P^{\frac{1}{2}}$ dependence. While this is the same sort of argument applied to the Helmholtz free energy in GE, it is similarly not invertible; the approaches are not equivalent.

Thermodynamic stability requires that the Gibbs free energy be a concave function of the stress [96], or equivalently that the negative Gibbs free energy $\mathcal{G}$ be convex. So we require

$$\frac{\partial^2 \mathcal{G}}{\partial P^2} = \frac{3}{4}(BP)^{-\frac{1}{2}}\left(\beta + \frac{\sigma_s^2}{P^2}\right) \geq 0 \tag{3.134}$$

$$\frac{\partial^2 \mathcal{G}}{\partial \sigma_s^2} = 2(BP)^{-\frac{1}{2}} \geq 0 \tag{3.135}$$

$$\frac{\partial^2 \mathcal{G}}{\partial P^2}\frac{\partial^2 \mathcal{G}}{\partial \sigma_s^2} - \left(\frac{\partial^2 \mathcal{G}}{\partial P \partial \sigma_s}\right)^2 = \frac{3}{2}(BP)^{-1}\left(\beta + \frac{\sigma_s^2}{P^2}\right) - (BP)^{-1}\frac{\sigma_s^2}{P^2} = \frac{1}{2}(BP)^{-1}\left(3\beta + \frac{\sigma_s^2}{P^2}\right) \geq 0 \tag{3.136}$$

According to condition 3.135, the constant B must be positive. If we consider the case of pure compression ($\sigma_s = 0$), condition 3.134 or 3.136 dictates that the constant β must also be positive. Since σ_s^2/P^2 is always positive, $\mathcal{G}$ is convex everywhere, and does not possess the thermodynamically unstable region of GE. While this was identified as a feature of GE, and provided a clear definition of the yield angle, we have seen that the values obtained were always unrealistic, with no clear method of relaxing that constraint. This analogous Gibbs free energy potential, lacking such a constraint, may then prove to be a better model for granular statics.

In GE, the thermodynamic stability condition on the stress invariants was identical to a surface beyond which there were no elastic solutions whatsoever. While $\mathcal{G}$ lacks a similar thermodynamic constraint, it similarly possesses a region of no solutions outside a Drucker-Prager type yield surface. Identifying

$$\frac{\partial \mathcal{G}}{\partial P} = \Delta = \frac{3}{2}\eta\left(\frac{P}{B}\right)^{\frac{1}{2}} - \frac{\sigma_s^2}{2BP^{\frac{3}{2}}} \tag{3.137}$$

and solving for σ_s,

$$\sigma_s = \sqrt{3\beta P^2 - 2\Delta B^{\frac{1}{2}} P^{\frac{3}{2}}} \tag{3.138}$$

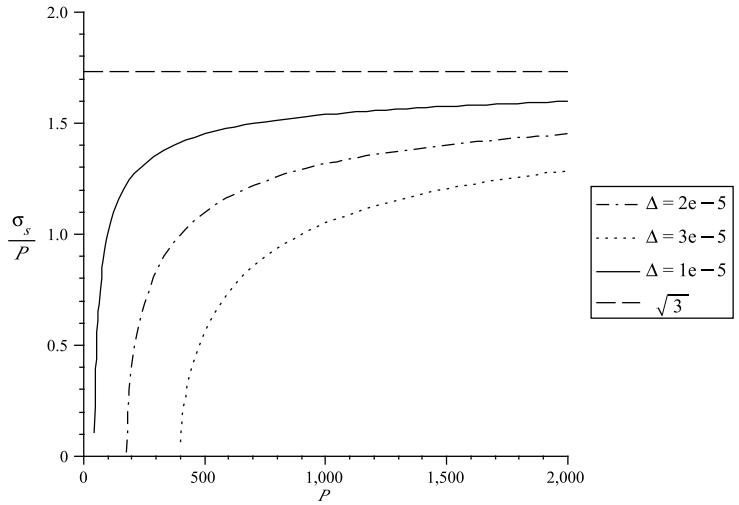

Figure 3.10. The stress ratio σ_s/P as a function of pressure, for $\beta = 1$ and B =1e12 (arbitrary units).

which we can rewrite in terms of the stress ratio as

$$\frac{\sigma_s}{P} = \sqrt{3\beta - \frac{2\Delta B^{\frac{1}{2}}}{P^{\frac{1}{2}}}} \tag{3.139}$$

The critical stress ratio is not tangent to the stress paths as in GE, but is approached in the limit:

$$\lim_{P\to\infty} \frac{\sigma_s}{P} = \sqrt{3\beta} \tag{3.140}$$

Stress paths for various values of Δ are shown in figure 3.10. The strain paths can be determined by solving

$$\frac{\partial \mathcal{G}}{\partial \sigma_s} = u_s = 2\sigma_s \left(BP\right)^{-\frac{1}{2}} \tag{3.141}$$

for σ_s,

$$\sigma_s = \frac{1}{2} u_s \left(BP\right)^{\frac{1}{2}} \tag{3.142}$$

and substituting into equation 3.137 to obtain

$$\Delta = \frac{3}{2}\beta \left(\frac{P}{B}\right)^{\frac{1}{2}} - \frac{u_s^2 B^{\frac{1}{2}}}{8P^{\frac{1}{2}}} \tag{3.143}$$

Some strain paths are plotted in figure 3.11, revealing that the Einav-Puzrin (EP) model similarly predicts shear dilation. Unlike the stress ratio, and lacking the stability condition on the strains of GE, there do not appear to be values of u_s/Δ that are strictly off limits.

Having established this limit on the stress invariants, we turn our attention again to the infinite plane problem (figure 3.4), in order to ascertain what restrictions may be placed on the yield angle. The plane problem is more complicated in this case, as differentiating the free energy now gives the strains as functions of the stresses. Defining the stress ratio in terms of the strain ratio will require inverting the system. Consider

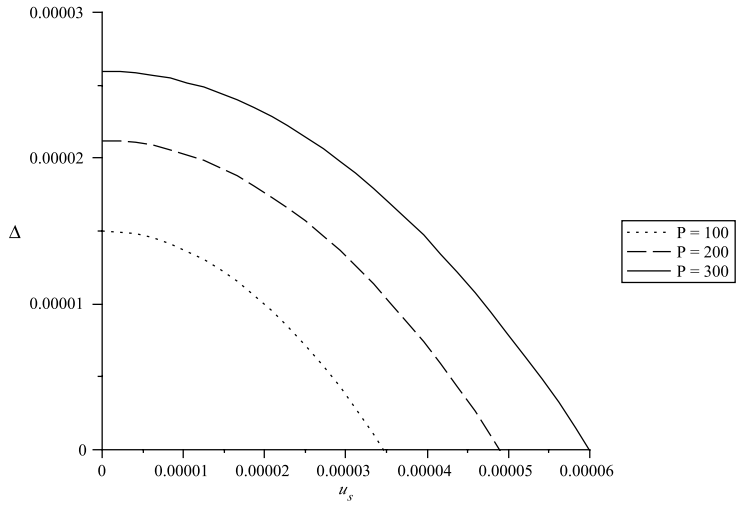

Figure 3.11. EP model strain paths for $B = 1e12$ and $\beta = 1$ (arbitrary units).

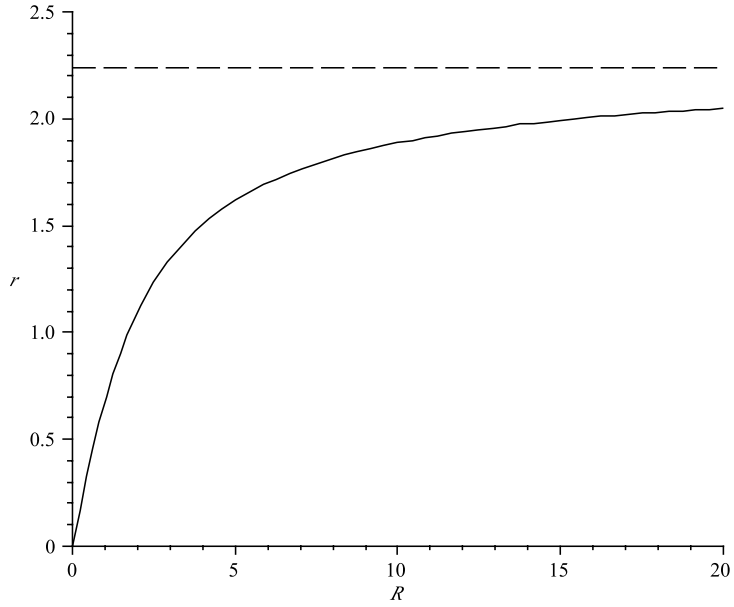

Figure 3.12. The stress ratio τ_4/σ_2 as a function of the strain ratio γ_4/u_2 for plane stress in the EP model. τ_4/σ_2 approaches the limit $\sqrt{5/3}$ as γ_4/u_2 becomes large.

the case of plane stress, in which $\sigma_3 = \tau_5 = \tau_6 = 0$ and $u_3 = \gamma_5 = \gamma_6 = 0$; we wish to obtain the ratio τ_4/σ_2. Recall that $u_1 = 0$, though σ_1 is not; the first step, then, in the solution process is to solve $u_1 = 0$ for σ_1, and substitute into the remaining two equations. There are two solutions for σ_1 (see appendix D); one stable and one unstable ($P < 0$). The stable solution gives a limiting strain ratio $r = \gamma_4/u_2$ for increasing stress ratio $R = \tau_4/\sigma_2$ (figure 3.12), with

$$\lim_{\frac{\tau_4}{\sigma_2}\to\infty} \frac{\gamma_4}{u_2} = \sqrt{\frac{2}{3}(\beta + 6)} \tag{3.144}$$

This does not provide any definition of the yield angle. Nevertheless, it is standard praxis in granular mechanics to impose a yield condition external to the elastic model itself. The simplification provided by GE, defining the yield angle with the stability condition, has proved too strict for modeling real problems. The EP model thus far succeeds in providing for non-linearity, thermodynamic consistency, and shear dilation without this over-constraint, and will be further evaluated in sections 4 and 5.

3.6.3 Model of Houlsby, Amorosi, and Rojas

The final model we will consider is that recently proposed by Houlsby, Amorosi, and Rojas (HAR) [76]. They initially propose three different potentials. The first is a Helmholtz free energy of precisely the form of GE (equation 3.36). They do not pursue this form any further, nor apparently are they aware of the previous work of Jiang and Liu [68]. They also consider the EP model; but curiously, they consider the limiting stress ratio, present in GE, EP, and essentially the defining characteristic of granular materials, to

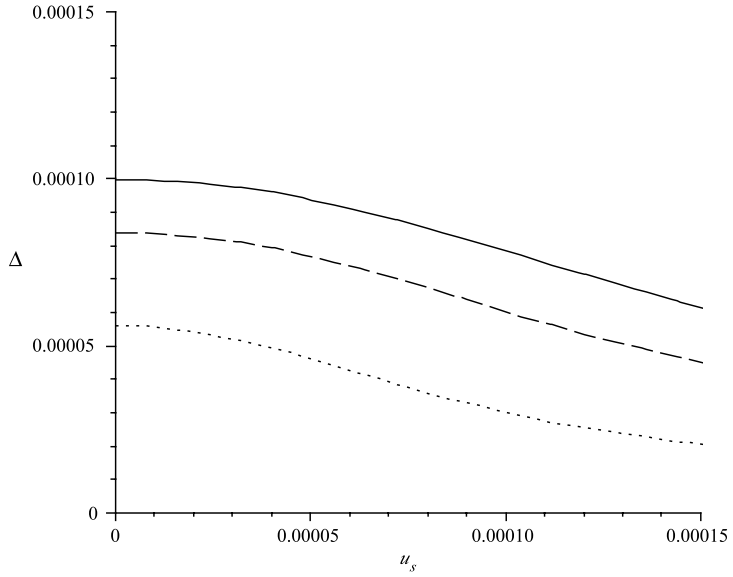

Figure 3.13. Δ vs. u_s for $\alpha = 1$ and $P^2/\left(9A^2\right)$ =1e-17 (dot), 5e-17 (dash), and 1e-16 (solid).

be a drawback to this type of model. Citing additionally the desire for ease of manipulation, particularly the ability to convert between Helmholtz and Gibbs free energy forms, they propose

$$\mathcal{F} = A\left(\alpha\Delta^2 + u_s^2\right)^n \tag{3.145}$$

Taking $n = 3/2$,

$$\mathcal{F} = A\left(\alpha\Delta^2 + u_s^2\right)^{\frac{3}{2}} \tag{3.146}$$

achieves the desired pressure dependence for dry granular materials. This potential is convex everywhere, has solutions everywhere, and the complementary energy can be obtained via the Legendre transform [67, 76]. For $n = 3/2$ it is (see appendix E)

$$\mathcal{G} = \frac{2}{3\sqrt{3A}}\left(\frac{1}{\alpha}P^2 + \sigma_s^2\right)^{\frac{3}{4}} \tag{3.147}$$

Contrary to the GE and EP models, the HAR model allows for pure shear ($\sigma_s \neq 0$ when $P = 0$) and tensile solutions. It does, however, feature shear dilation. The relationship is obtained (for $n = 3/2$) by taking

$$\frac{\partial\mathcal{F}}{\partial\Delta} = P = 3A\alpha\Delta\sqrt{\alpha\Delta^2 + u_s^2} \tag{3.148}$$

or

$$\frac{P^2}{9A^2\alpha^3} = \Delta^4 + \frac{1}{\alpha}\Delta^2 u_s^2 \tag{3.149}$$

Some strain paths for varying values of P are shown in figure 3.13. Note that in this model, the constant A has units of pressure, and α is dimensionless.

4 Elastic Moduli

4.1 Pressure Dependence

It was noted previously that dry, cohesionless granular materials invariably possess elastic moduli that vary approximately as $P^{1/2}$ [37–57]. This sort of stress dependence is built into the GE-C, EP, and HAR models by choosing $a = 1$, $m = 1/2$, and $n = 3/2$, respectively. Consider the case of pure compression, in which $\sigma_s, u_s = 0$. The bulk modulus is given by

$$K = \frac{P}{\Delta} = \frac{1}{\Delta}\frac{\partial \mathcal{F}}{\partial \Delta} \tag{4.1}$$

or equivalently

$$\frac{1}{K} = \frac{\Delta}{P} = \frac{1}{P}\frac{\partial \mathcal{G}}{\partial P} \tag{4.2}$$

For the GE-C (equation 3.81), EP (equation 3.133), and either form of the HAR model (equations 3.146 and 3.147), this leads to

$$K = \sqrt{\frac{6\xi\tilde{G}}{5}}\sqrt{P} \tag{4.3}$$

$$K = \frac{2\sqrt{B}}{3\beta}\sqrt{P} \tag{4.4}$$

$$K = \sqrt{3A}\alpha^{\frac{3}{4}}\sqrt{P} \tag{4.5}$$

So all three models give a bulk (as well as shear) modulus that indeed varies with the square root of pressure. However, triaxial tests and other studies [47, 49–52, 55, 56] have identified more specific stress dependence, which we investigate in this section.

4.2 Stress Induced and Inherent Anisotropy

A defining characteristic of granular materials is anisotropy. They are typically anisotropic in two fundamentally different ways, which are “inherent” or “fabric” anisotropy, and stress-induced anisotropy. Fabric anisotropy presumably arises from inhomogeneities in the particle contact network, such that even for isotropic stress states, the material possesses different stiffness in different directions. This type of anisotropy depends strongly on the deformation history or sample preparation, e.g. the method of pouring a sandpile or triaxial specimen. On the other hand, granular materials are observed to become anisotropic under anisotropic stress conditions, even if initially isotropic under isotropic stress conditions. This is referred to as stress-induced anisotropy. We may account for fabric anisotropy in linear elasticity by introducing elastic

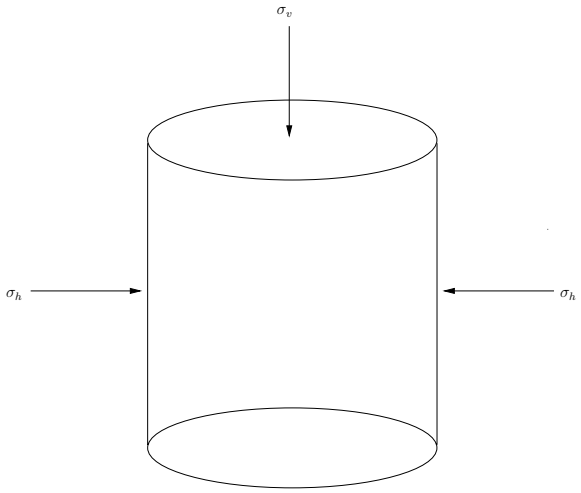

Figure 4.1. The triaxial test configuration. The stress component into the page is also equal to σ_h; in the "true" triaxial test, this third stress component may differ from the other two.

constants for each direction, e.g. a compliance matrix of the form

$$\begin{bmatrix} \frac{1}{E_1} & -\frac{\nu_{21}}{E_2} & -\frac{\nu_{31}}{E_3} & 0 & 0 & 0 \\ -\frac{\nu_{12}}{E_1} & \frac{1}{E_2} & -\frac{\nu_{32}}{E_3} & 0 & 0 & 0 \\ -\frac{\nu_{13}}{E_1} & -\frac{\nu_{23}}{E_2} & \frac{1}{E_3} & 0 & 0 & 0 \\ 0 & 0 & 0 & \frac{1}{G_{12}} & 0 & 0 \\ 0 & 0 & 0 & 0 & \frac{1}{G_{23}} & 0 \\ 0 & 0 & 0 & 0 & 0 & \frac{1}{G_{13}} \end{bmatrix} \tag{4.6}$$

Stress-induced anisotropy, on the other hand, implies not only that the elasticity is not linear (i.e. the moduli are functions of stress), but that there is a dependence on individual stress components, not just the stress invariants or mean stress. Though the free energies under consideration are given in terms of the invariants, the components of the stiffness matrix (or compliance matrix) indeed exhibit stress-induced anisotropy; they depend on both the invariants Δ and u_s, but also on the individual strains u_i. A term-by-term comparison of the compliance matrix from anisotropic linear elasticity (equation 4.6) and the non-linear models under consideration may give the specific stress dependence of the elastic moduli. In addition, these models possess what Einav and Puzrin [73] call *stress-induced cross anisotropy*. This is evidenced by the non-zero $\partial^2\mathcal{G}/\partial\sigma_i\partial\tau_j$ terms present in the non-linear models, which are the source of their shear dilatancy.

The triaxial test serves as an important simplification and test case for non-linear models. In the triaxial test, beginning from an isotropic stress state, an additional axial load is applied to a cylindrical specimen (see figure 4.1). All three shear stress components are zero, which eliminates the cross-anisotropic terms from the nonlinear models. The two horizontal components of stress (σ_1 and σ_3) are equal, so we may write

the anisotropic linear elasticity compliance matrix as

$$\begin{bmatrix} \frac{1}{E_h} & -\frac{\nu_{vh}}{E_v} & -\frac{\nu_{hh}}{E_h} \\ -\frac{\nu_{hv}}{E_h} & \frac{1}{E_v} & -\frac{\nu_{hv}}{E_h} \\ -\frac{\nu_{hh}}{E_h} & -\frac{\nu_{vh}}{E_v} & \frac{1}{E_h} \end{bmatrix} \tag{4.7}$$

In the absence of shear components, the non-linear compliance matrices similarly simplify to 3 x 3, now allowing for direct comparison of the terms; the Young's moduli may be determined directly from the diagonal terms. Many recent experiments [47, 49–52, 55, 56] have examined the reversible elastic regime in the triaxial test, and offer a point of direct comparison for the theories presented here, and some insight into the difference between fabric and stress-induced anisotropy. The experiments find that the Young's moduli do not just vary with the mean stress, but with the stress in a particular direction; e.g. the vertical Young's modulus is a function of the vertical stress, but is largely independent of the horizontal stress. The experimental data are well fitted by the following expressions:

$$E_v = C_v \sigma_v^n \tag{4.8}$$

$$E_h = C_h \sigma_h^n \tag{4.9}$$

where n is never far from 1/2, and here the constants C must have units of $P^{1/2}$. $C_v \neq C_h$ implies some degree of fabric anisotropy, as then $E_v \neq E_h$ even when $\sigma_v = \sigma_h$; conversely, if $C_v = C_h$, the Young's moduli are equal if the stresses are equal, but anisotropic stress states induce anisotropy. This is illustrated by considering the ratio E_v/E_h as a function of the stress ratio σ_v/σ_h, as in the data of Hoque and Tatsuoka, figure 4.2. The hyperelastic models considered here do not incorporate fabric anisotropy, though they do not preclude doing so. It would be difficult to establish the anisotropic constants with any certainty, as they appear to depend on the details of the sample formation. Even in the rather simple case of the triaxial test, where some consistent difference between C_v and C_h might be discernible, there does not appear to be one; in some experiments [49, 52, 55, 56], $C_v > C_h$, while in others [47] $C_h > C_v$.

4.3 Comparison of Theories and Experiment

4.3.1 Young's Modulus

As a first point of comparison, we note that for $C_v = C_h$, i.e. an "inherently isotropic" material, the usual experiment data fits give the following measure of stress-induced anisotropy:

$$\frac{E_v}{E_h} = \left(\frac{\sigma_v}{\sigma_h}\right)^n \tag{4.10}$$

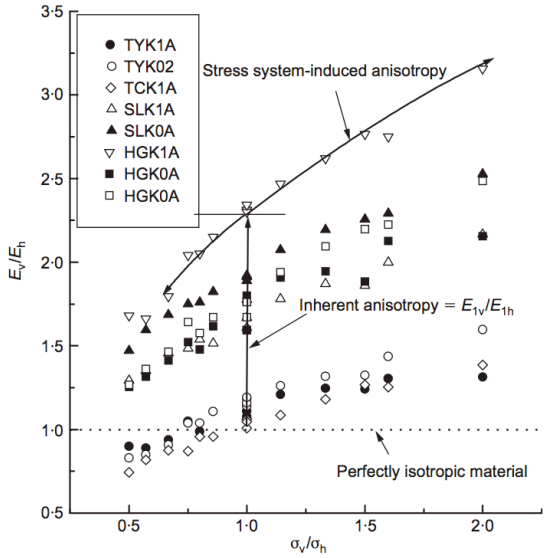

Figure 4.2. Experiment data from [56] illustrating the difference between "stress-induced" and "inherent" anisotropy. Here E_{1v} and E_{1h} are constants equivalent to C_v and C_h in equations 4.8-4.9.

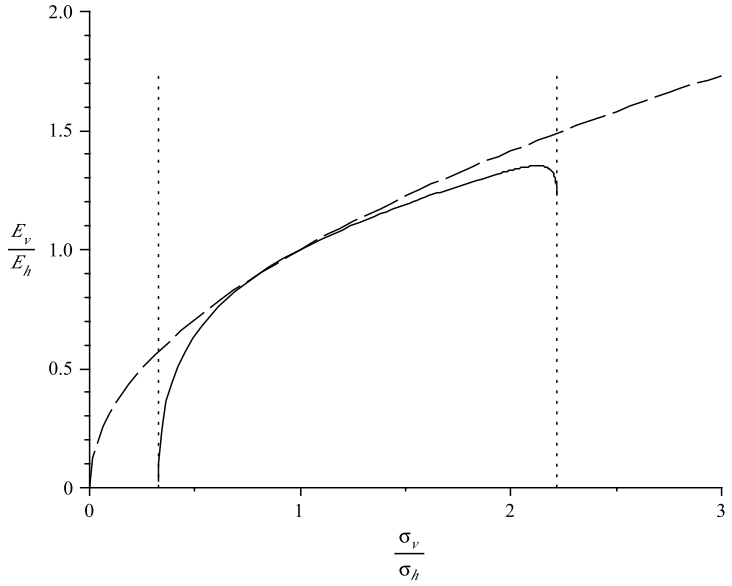

Figure 4.3. The ratio of Young's moduli E_v/E_h as a function of the stress ratio σ_v/σ_h for the GE-C model (solid line) and the empirical fit (dashed line). Here $\xi = 5/3$, in order to give the highest possible value of the yield angle for this model ($\sim 17°$). The dotted lines mark the stability limits of GE-C.

The advantage of using a Gibbs free energy formulation for comparison of the Young's moduli is apparent, since this relationship is easily obtained by differentiating:

$$\frac{E_v}{E_h} = \frac{\dfrac{\partial^2 \mathcal{G}}{\partial \sigma_1^2}}{\dfrac{\partial^2 \mathcal{G}}{\partial \sigma_2^2}} \tag{4.11}$$

Here the vertical component is σ_2 and the horizontal component is σ_1. The result for the EP and HAR models, respectively, is

$$\frac{E_v}{E_h} = \frac{(\beta+30)\left(\frac{\sigma_v}{\sigma_h}\right)^2 + (4\beta+60)\left(\frac{\sigma_v}{\sigma_h}\right) + 4\beta + 54}{(\beta+6)\left(\frac{\sigma_v}{\sigma_h}\right)^2 + (4\beta+36)\left(\frac{\sigma_v}{\sigma_h}\right) + 4\beta + 102} \tag{4.12}$$

$$\frac{E_v}{E_h} = \frac{\left(63\alpha^2+30\alpha+1\right)\left(\frac{\sigma_v}{\sigma_h}\right)^2 + \left(-126\alpha^2+30\alpha+4\right)\left(\frac{\sigma_v}{\sigma_h}\right) + 63\alpha^2 + 48\alpha + 4}{(36\alpha^2+12\alpha+1)\left(\frac{\sigma_v}{\sigma_h}\right)^2 + (-72\alpha^2+12\alpha+4)\left(\frac{\sigma_v}{\sigma_h}\right) + 36\alpha^2 + 84\alpha + 4} \tag{4.13}$$

For GE and related Helmholtz free energy models, the situation is more complicated. Here we have a stiffness matrix of strain dependent terms, and equations for the stresses σ_v and σ_h, also in terms of the strains. There is not a simple expression for the ratio of the Young's moduli as functions of stress, but inverting the stiffness matrix at least gives E_v and E_h in terms of the strains. With both σ_v/σ_h and E_v/E_h given as functions of the strain ratio u_v/u_h, we may at least plot their relationship parametrically. The result, for GE-C, is shown in figure 4.3. GE-C matches well near the isotropic stress state, but E_v/E_h falls off sharply with increasing

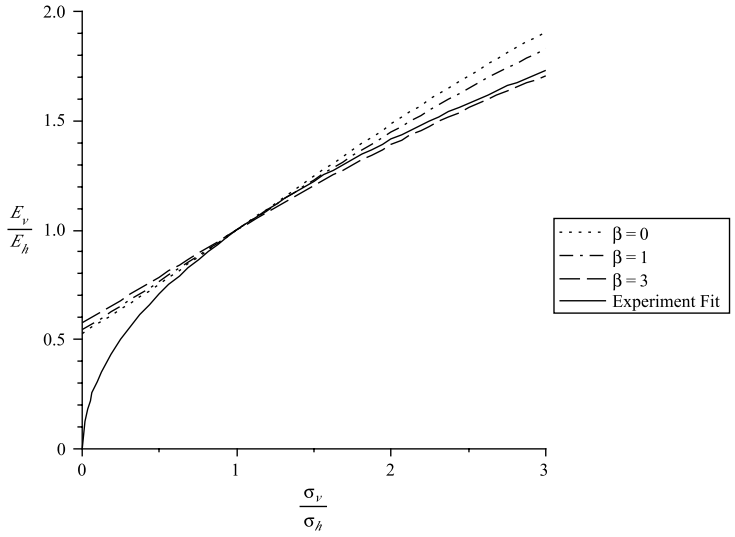

Figure 4.4. The ratio of Young's moduli E_v/E_h as a function of the stress ratio σ_v/σ_h for the EP model, at varying values of β, and empirical fit.

anisotropy. The dotted lines in figure 4.3 mark the loss of stability (convexity) in GE-C; while this stability condition imposes a severe constraint on the yield angle in the plane problem ($\phi_y \lesssim 17°$), the limits here are not unrealistic; the elastic regime is not found to extend far beyond $\sigma_v/\sigma_h \approx 2.2$ [55]. The values given by the EP model (equation 4.12) and the HAR model (equation 4.13) are shown in figures 4.4 and 4.5, respectively. In the EP model, E_v/E_h is not strongly influenced by the value of β, and the curves are slightly flatter than the fit to experiment data, but there are no large discrepancies within the experimentally determined elastic range $0.4 \lesssim \sigma_v/\sigma_h \lesssim 2.5$. The HAR model appears reasonable for smaller values of α ($\sim 1/3$), but has some rather unphysical implications for higher values of α. In this case, there is a region $\sigma_v/\sigma_h < 1$ where the ratio E_v/E_h has a minimum, and *increases* with *decreasing* σ_v/σ_h. There is no such trend observable in the experiment data. This, at least, places some restrictions on allowable values of α.

Another noteworthy aspect of the experiment data fits (equations 4.8-4.9) is the assumption that the vertical Young's modulus is a function of *only* the vertical stress, and similarly the horizontal Young's modulus is a function of *only* the horizontal stress. While there is no discernible relationship between E_v and σ_h (or E_h and σ_v), there is some scatter in the data. Data of Hoque and Tatsuoka [49, 52] sometimes indicate E_v increasing slightly with σ_h, sometimes decreasing (figure 4.6). Bellotti et al. [47] actually plot E_v vs. σ_h, again finding them to be relatively independent, though perhaps E_v decreases with σ_h (figure 4.7). Kuwano and Jardine [55] do not present their data in this fashion, but find $\sim 10\%$ variation in their data taken at different stress ratios, when plotting E_v vs. σ_v and E_h vs. σ_h (figure 4.8). This sort of independence is not apparent in the hyperelastic models, which all appear to depend on all the stress components. A suitable model should at least possess a weak relationship between the Young's modulus in a given direction and the

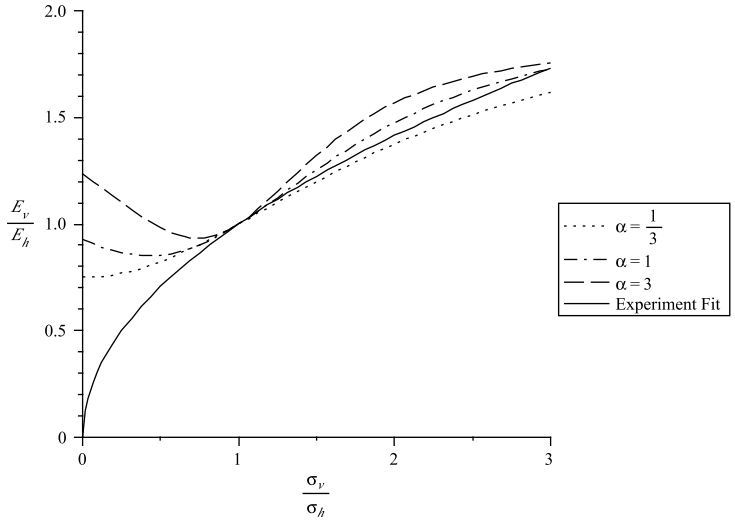

Figure 4.5. The ratio of Young's moduli E_v/E_h as a function of the stress ratio σ_v/σ_h for the HAR model, at varying values of α, and empirical fit.

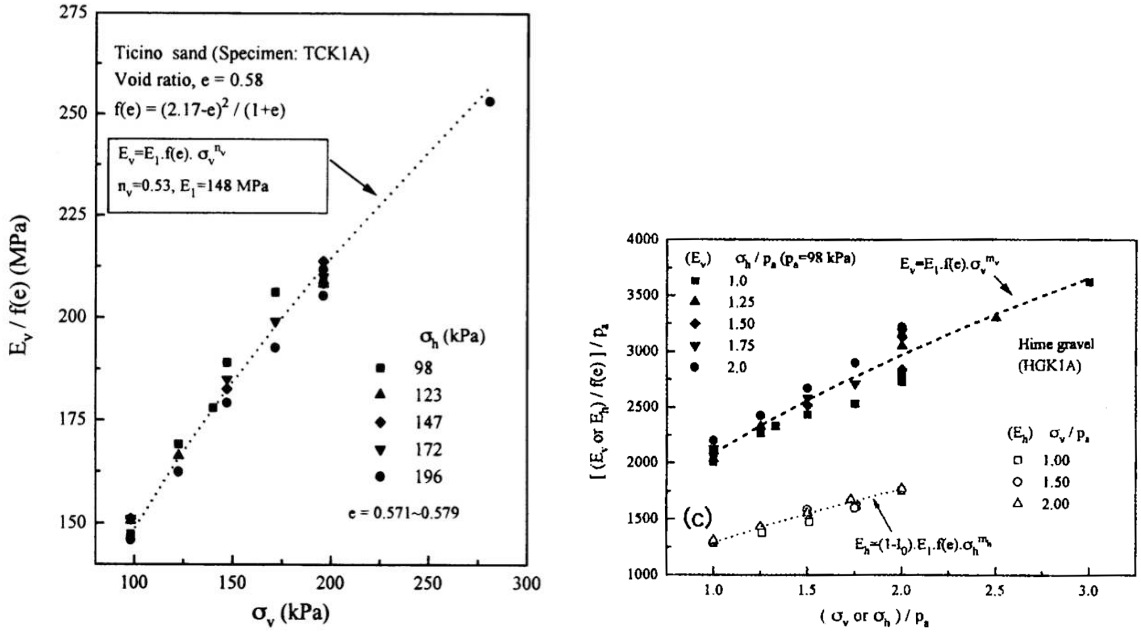

Figure 4.6. Data of Hoque and Tatsuoka, showing no discernible relationship between E_v and σ_h. On the left, E_v appears to decrease slightly with σ_h ([49], reprinted, with permission, from the Geotechnical Testing Journal, Vol. 19, No. 4, copyright ASTM International, 100 Barr Harbor Drive, West Conshohocken, PA 19428). On the right, it increases slightly with σ_h [52].

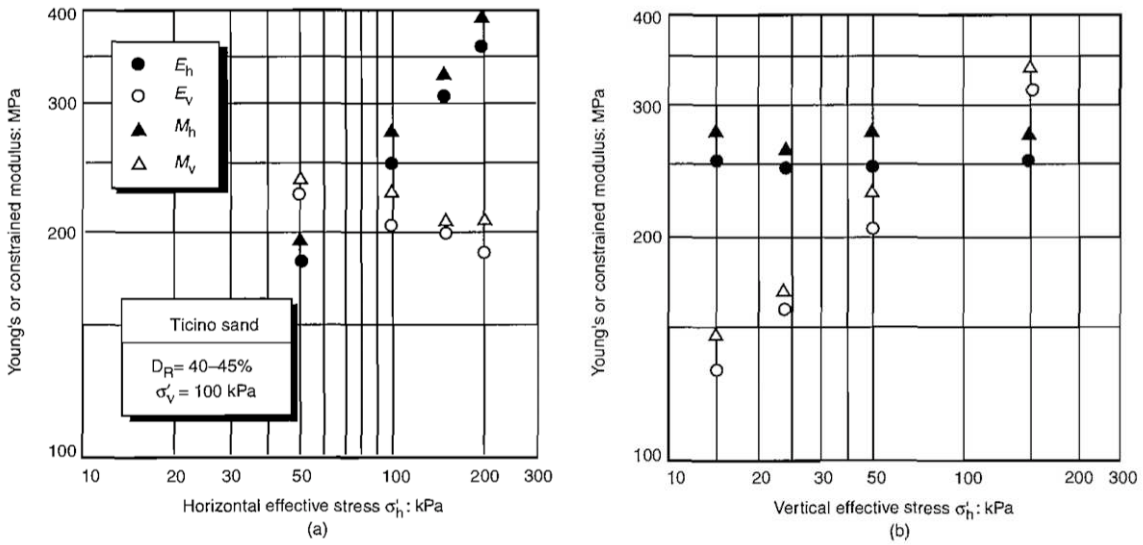

Figure 4.7. Young's modulus as a function of stress as determined by Bellotti et al. [47]. E_v perhaps decreases slightly with σ_h (left); there is no clear dependence of E_h on σ_v (right; note the mislabeling of the x axis).

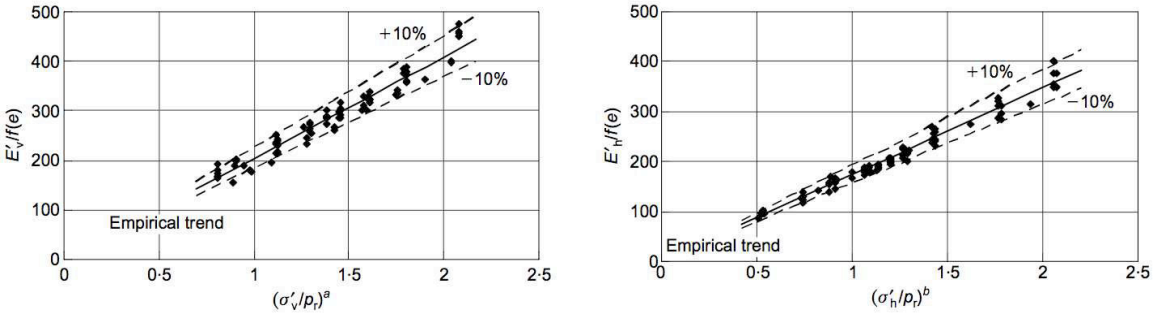

Figure 4.8. Data of Kuwano and Jardine [55] showing a ±10% scatter about the data fits; E_v is assumed to be independent of σ_h, and E_h independent of σ_v.

stresses perpendicular to that direction. Consider, then, the expressions for E_v and E_h resulting from the various hyperelastic models. For Helmholtz free energy models such as GE and GE-C, once again we have E, σ in terms of the strains and must resort to parametric plotting (figure 4.9) in lieu of a simple solution $E(\sigma)$. For the EP (figure 4.10) and HAR (figure 4.11) models, we have

$$\frac{E_v}{B} = \frac{4\sqrt{3}\left(2\frac{\sigma_h}{B} + \frac{\sigma_v}{B}\right)^{\frac{5}{2}}}{(\beta+6)\left(\frac{\sigma_v}{B}\right)^2 + (4\beta+36)\left(\frac{\sigma_v}{B}\right)\left(\frac{\sigma_h}{B}\right) + (4\beta+102)\left(\frac{\sigma_h}{B}\right)^2} \tag{4.14}$$

$$\frac{E_v}{A} = \frac{18\alpha^{\frac{3}{4}}\left((6\alpha+1)\left(\frac{\sigma_v}{A}\right)^2 + (-12\alpha+4)\left(\frac{\sigma_v}{A}\right)\left(\frac{\sigma_h}{A}\right) + (6\alpha+4)\left(\frac{\sigma_h}{A}\right)^2\right)^{\frac{5}{4}}}{(36\alpha^2+12\alpha+1)\left(\frac{\sigma_v}{A}\right)^2 + (-72\alpha^2+12\alpha+4)\left(\frac{\sigma_v}{A}\right)\left(\frac{\sigma_h}{A}\right) + (36\alpha^2+84\alpha+4)\left(\frac{\sigma_h}{A}\right)^2} \tag{4.15}$$

It is apparent that both the GE-C and HAR models predict large variations in E_v with σ_h, in stark contrast with experiment data, in which there is no clear relationship. In the EP model, though E_v is not explicitly independent of σ_h, there is very little variation over the entire range of stress ratios in the elastic regime. Of course, we expect similar independence of E_h and σ_v; for the EP model,

$$\frac{E_h}{B} = \frac{4\sqrt{3}\left(2\frac{\sigma_h}{B} + \frac{\sigma_v}{B}\right)^{\frac{5}{2}}}{(\beta+30)\left(\frac{\sigma_v}{B}\right)^2 + (4\beta+60)\left(\frac{\sigma_v}{B}\right)\left(\frac{\sigma_h}{B}\right) + (4\beta+54)\left(\frac{\sigma_h}{B}\right)^2} \tag{4.16}$$

and for the HAR model,

$$\frac{E_h}{A} = \frac{18\alpha^{\frac{3}{4}}\left((6\alpha+1)\left(\frac{\sigma_v}{A}\right)^2 + (-12\alpha+4)\left(\frac{\sigma_v}{A}\right)\left(\frac{\sigma_h}{A}\right) + (6\alpha+4)\left(\frac{\sigma_h}{A}\right)^2\right)^{\frac{5}{4}}}{(63\alpha^2+30\alpha+1)\left(\frac{\sigma_v}{A}\right)^2 + (-126\alpha^2+30\alpha+4)\left(\frac{\sigma_v}{A}\right)\left(\frac{\sigma_h}{A}\right) + (63\alpha^2+48\alpha+4)\left(\frac{\sigma_h}{A}\right)^2} \tag{4.17}$$

Figures 4.12, 4.13, and 4.14 indicate that E_h is quite independent of σ_v in the EP model, but there are significant variations in the HAR and GE-C models.

Finally, we expect that Young's modulus should vary approximately with the square root of the in-plane stress component, as observed in experiments (equations 4.8-4.9). Equations 4.14 and 4.15 for E_v are plotted against σ_v in figures 4.15 and 4.16, and the parametric plot for GE-C is shown in figure 4.17. The scaling here is arbitrary, so it is the shape, not the magnitude, of the curves that is of interest. While none of the models are exactly linear on the log-log plots, it is clear that the EP model is the best of the three at capturing this behavior. As noted previously, the HAR model is a worse match to experiment data for increasing values of α, and once again we have fixed $\xi = 5/3$ for GE-C in order to achieve the maximum (but still too low) yield angle $\sim 17°$.

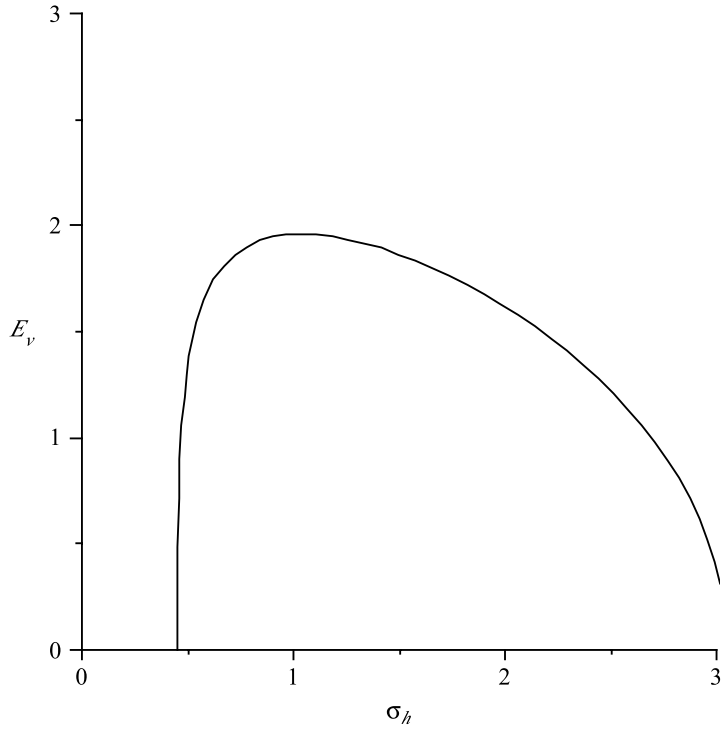

Figure 4.9. The vertical Young's modulus E_v as a function of the horizontal stress σ_h for the GE-C model. Values are normalized with respect to $\tilde{G}$; $\sigma_v = 1$ and $\xi = 5/3$. E_v varies substantially with σ_h, in contrast with experiment data.

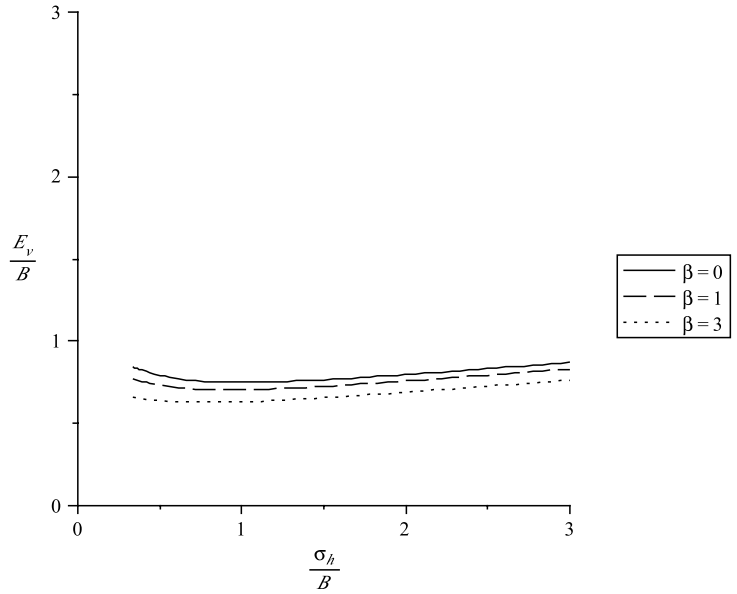

Figure 4.10. The vertical Young's modulus E_v as a function of the horizontal stress σ_h for the EP model, $\sigma_v/B = 1$. E_v varies only slightly with σ_h, in relative agreement with experiment data, where there is no clear dependence of E_v on σ_h.

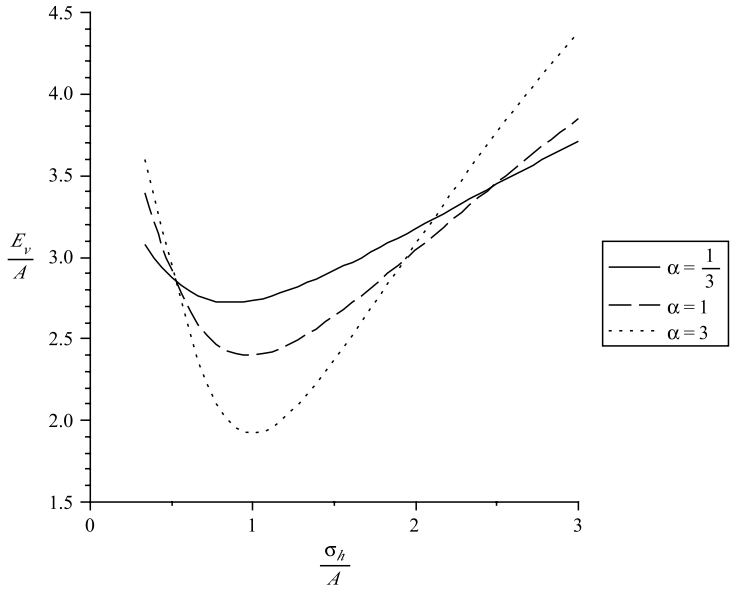

Figure 4.11. The vertical Young's modulus E_v as a function of the horizontal stress σ_h for the HAR model, $\sigma_v/A = 1$. E_v varies substantially with σ_h, in contrast with experiment data. In particular, as noted previously, results become more unphysical for increasing values of α.

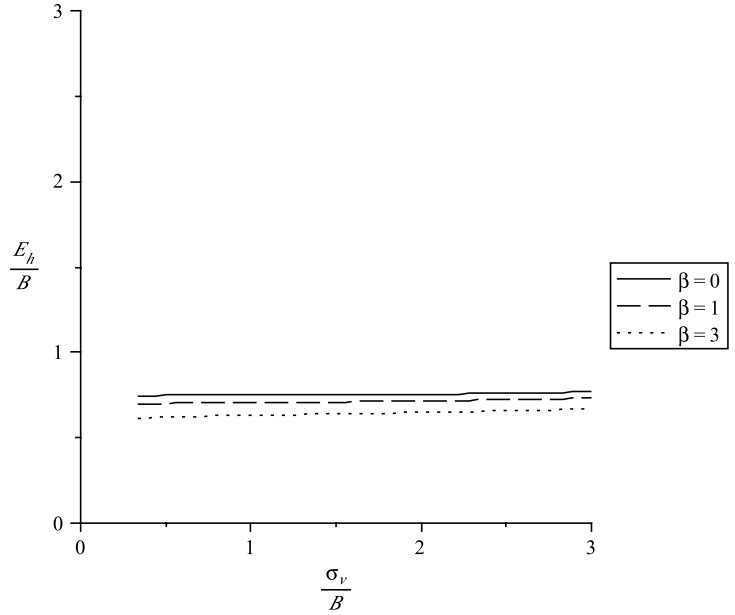

Figure 4.12. The horizontal Young's modulus E_h as a function of the vertical stress σ_v for the EP model, $\sigma_h/B = 1$. Once again, E_h varies only slightly with the out of plane stress σ_v, in agreement with experiment data.

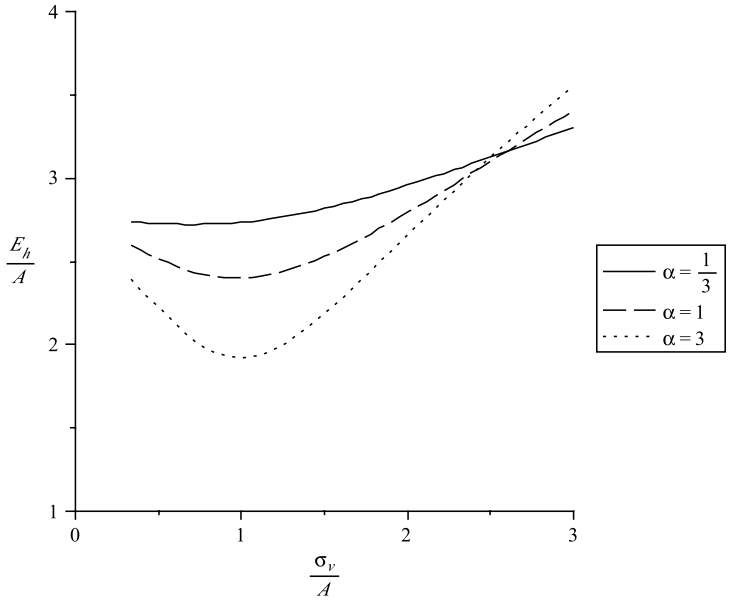

Figure 4.13. The horizontal Young's modulus E_h as a function of the vertical stress σ_v for the HAR model, $\sigma_h/A = 1$. E_h varies substantially with the out of plane stress σ_v, particularly for larger values of α.

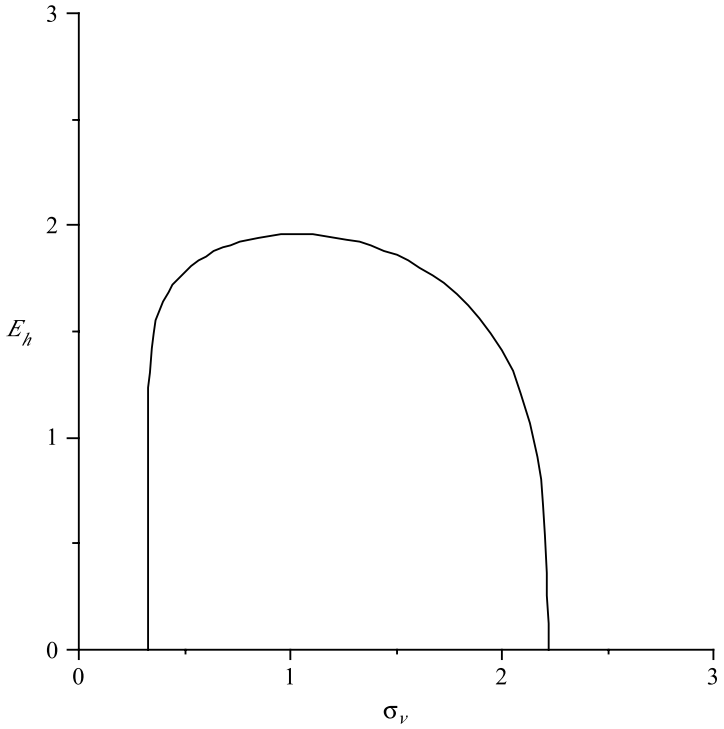

Figure 4.14. The horizontal Young's modulus E_h as a function of the vertical stress σ_v for the GE-C model. Values are normalized with respect to $\tilde{G}$; $\sigma_h = 1$ and $\xi = 5/3$. E_h varies substantially with σ_v, in contrast with experiment data.

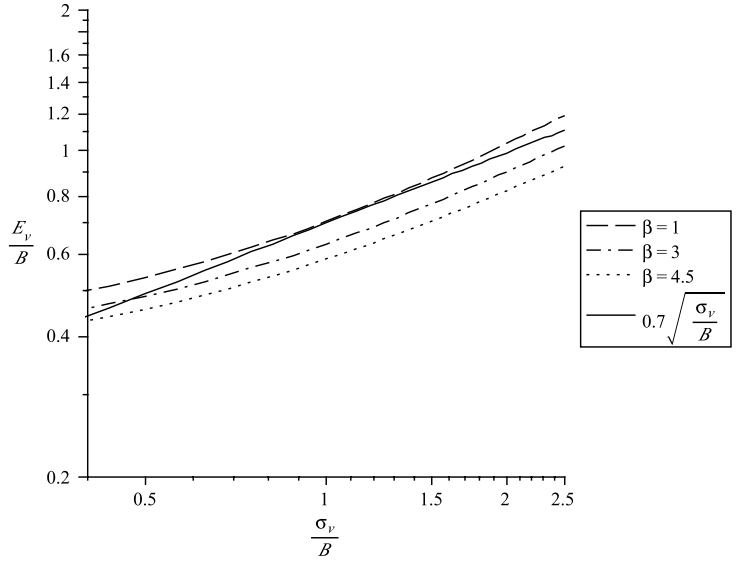

Figure 4.15. E_v vs. σ_v for the EP model, and experiment fit.

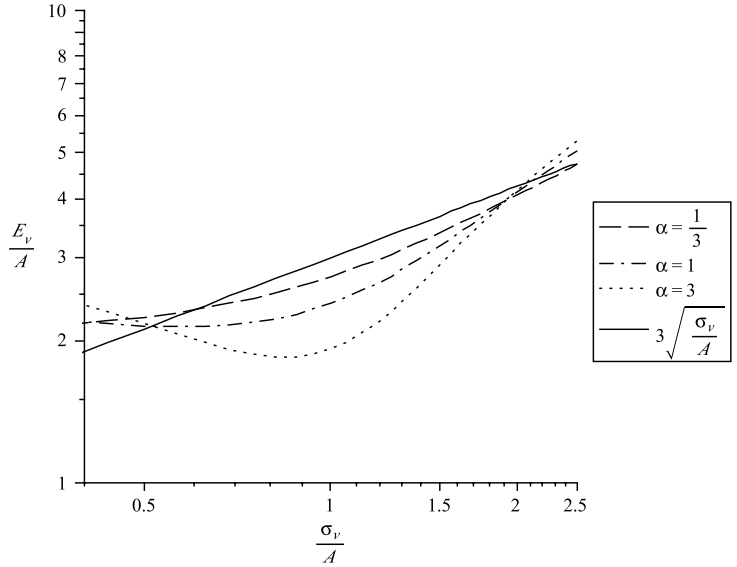

Figure 4.16. E_v vs. σ_v for the HAR model, and experiment fit.

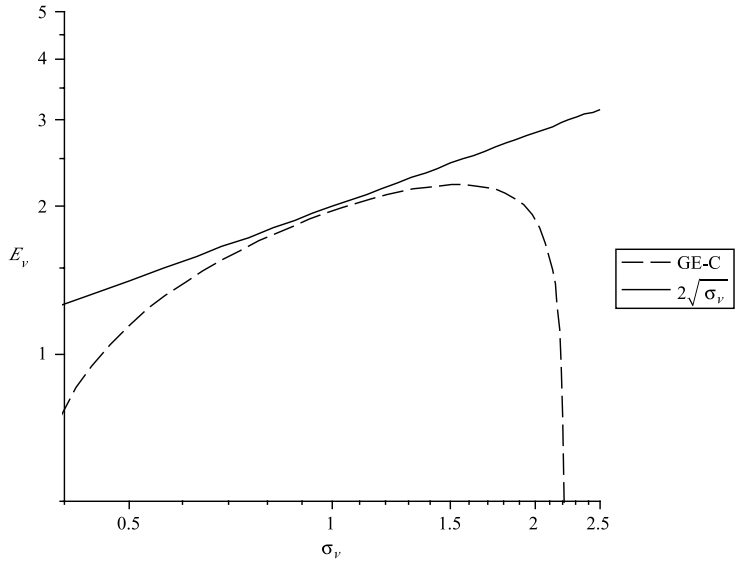

Figure 4.17. E_v vs. σ_v (normalized to $\tilde{G}$) for the GE-C model, and experiment fit.

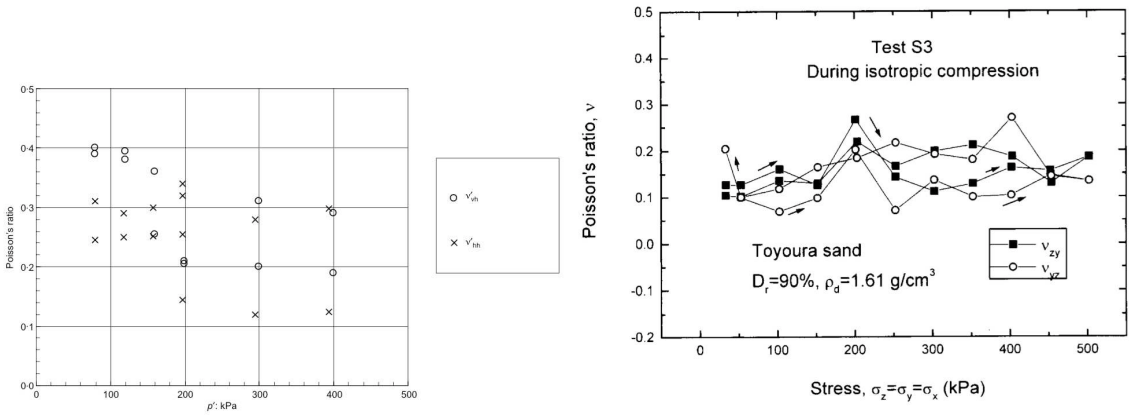

Figure 4.18. Measured values of Poisson's ratio, from [55] (left) and [97] (right). Poisson's ratio is assumed to be independent of the isotropic stress, though there is a large amount of scatter in the data.

4.3.2 Poisson's Ratio

In conducting triaxial tests, many researchers [49, 50, 52, 55–57, 97, 98] have also measured Poisson's ratio. Though there is typically a large amount of scatter in these data, two general features are apparent. First, Poisson's ratio does not vary significantly with the mean stress (see figure 4.18). Second, there is a power law relationship between Poisson's ratio and the stress ratio (figure 4.19), i.e.

$$\nu_{vh} \sim \left(\frac{\sigma_v}{\sigma_h}\right)^{\frac{n}{2}} \tag{4.18}$$

This trend is deduced from the Young's moduli, equations 4.8-4.9, and by noting that symmetry in the compliance matrix (equation 4.6)[1] requires

$$\frac{\nu_{vh}}{E_v} = \frac{\nu_{hv}}{E_h} \tag{4.19}$$

or

$$\frac{\nu_{vh}}{\nu_{hv}} = \frac{E_v}{E_h} = \frac{C_v}{C_h}\left(\frac{\sigma_v}{\sigma_h}\right)^{\frac{1}{2}} \tag{4.20}$$

This could be satisfied by any number of expressions for ν_{vh} and ν_{hv}, but it is *assumed* that [49, 52, 56]

$$\nu_{vh} = \nu_0 \left(\frac{C_v}{C_h}\right)^{\frac{1}{2}} \left(\frac{\sigma_v}{\sigma_h}\right)^{\frac{1}{4}} \tag{4.21}$$

$$\nu_{hv} = \nu_0 \left(\frac{C_h}{C_v}\right)^{\frac{1}{2}} \left(\frac{\sigma_h}{\sigma_v}\right)^{\frac{1}{4}} \tag{4.22}$$

where ν_0 is a constant. For an isotropic material, $C_v = C_h$, and

$$\nu_{vh} = \nu_0 \left(\frac{\sigma_v}{\sigma_h}\right)^{\frac{1}{4}} \tag{4.23}$$

[1]It is interesting to note that this symmetry is implied by the existence of the free energy, which is pointed out by AnhDan and Koseki [97]; as the present work has made apparent, the stress-strain relation and elastic moduli also proceed from this free energy, though this is never considered when choosing forms to fit the experimental data.

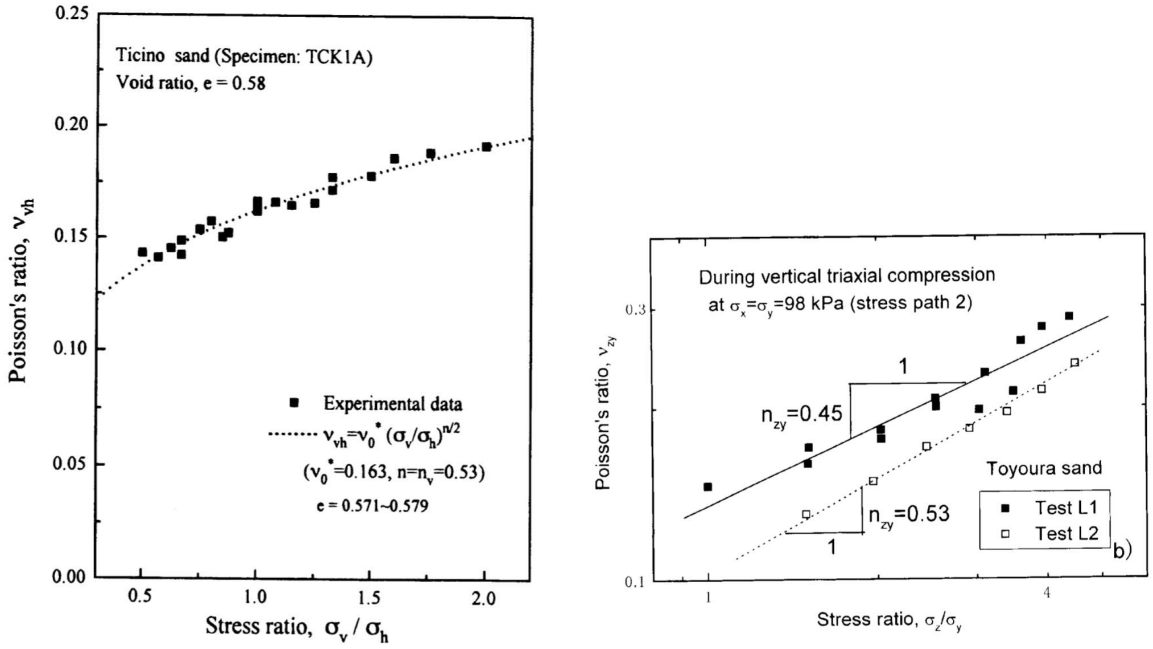

Figure 4.19. Experiment data for Poisson's ratio vs. stress ratio, from [97] (right) and [49] (left: reprinted, with permission, from the Geotechnical Testing Journal, Vol. 19, No. 4, copyright ASTM International, 100 Barr Harbor Drive, West Conshohocken, PA 19428).

$$\nu_{hv} = \nu_0 \left(\frac{\sigma_h}{\sigma_v} \right)^{\frac{1}{4}} \tag{4.24}$$

Others observe a stronger dependence of ν_{vh} on σ_v/σ_h ([97, 98], figure 4.19), $\nu_{vh} \sim (\sigma_v/\sigma_h)^{1/2}$, even when $E \sim \sigma^{1/2}$. For the hyperelastic models, it is apparent from the form of the compliance matrix (equation 4.6) that

$$\nu_{ij} = \frac{\dfrac{\partial^2 \mathcal{G}}{\partial \sigma_j \partial \sigma_i}}{\dfrac{\partial^2 \mathcal{G}}{\partial \sigma_i^2}} \tag{4.25}$$

Thus, we may similarly obtain analytical expressions for Poisson's ratio from the Gibbs free energy in the EP and HAR models. For the GE-C model, we must continue to resort to parametric plotting, as we can only obtain the stiffness matrix (inverse compliance matrix) and stresses as functions of the strains. In every case, the scale constants $\tilde{G}$, A, B cancel, so Poisson's ratio depends only on the stresses and the dimensionless constants ξ, α, and β. So, for the EP and HAR models, the experimental data on Poisson's ratio should give some idea what the appropriate range of values is for β and α; for GE-C, we have already fixed $\xi = 5/3$ based on yield angle constraints.

For the case of isotropic stress, $\sigma_1 = \sigma_2 = \sigma_3$, all three models give a constant Poisson's ratio:

$$\nu_{iso} = \frac{18\xi - 5}{36\xi + 5} \tag{4.26}$$

$$\nu_{iso} = \frac{8 - \beta}{16 + \beta} \tag{4.27}$$

$$\nu_{iso} = \frac{6\alpha - 1}{12\alpha + 1} \tag{4.28}$$

for the GE-C, EP, and HAR models, respectively. Some experimental data indicate ν_{iso} is as small as 0.1-0.2; if we take $\nu_{iso} = 0.163$ [49], this implies $\xi \approx 0.479$, for which equation 3.80 indicates there are no solutions. This is further evidence of the over-constraint resulting from the the convexity requirement of GE and GE-C. For the EP and HAR models, there are no such restrictions, and we are free to choose β and α to match experimental values of Poisson's ratio. The isotropic values given above give some idea what range of values for α and β are appropriate for real materials. We do not in practice encounter negative Poisson's ratios in granular materials, so we do not expect $\beta > 8$ or $\alpha < 1/6$. For isotropic, linear elastic materials, thermodynamics requires $\nu < 0.5$; there is no such restriction on anisotropic materials [99], and some values of ν greater than 0.5 have been observed [98]. The isotropic value is typically lower, however, than 0.5. For the EP model this merely implies $\beta > 0$, which is required by thermodynamics. The relationship between β and ν_{iso} is plotted in figure 4.20. ν_{iso} is equal to 0.5 in the limit $\alpha \to \infty$ in the HAR model, though it already reaches a value of 0.44 at $\alpha = 2$ (figure 4.21). So, $1/6 < \alpha < 2$ is probably a reasonable range to investigate.

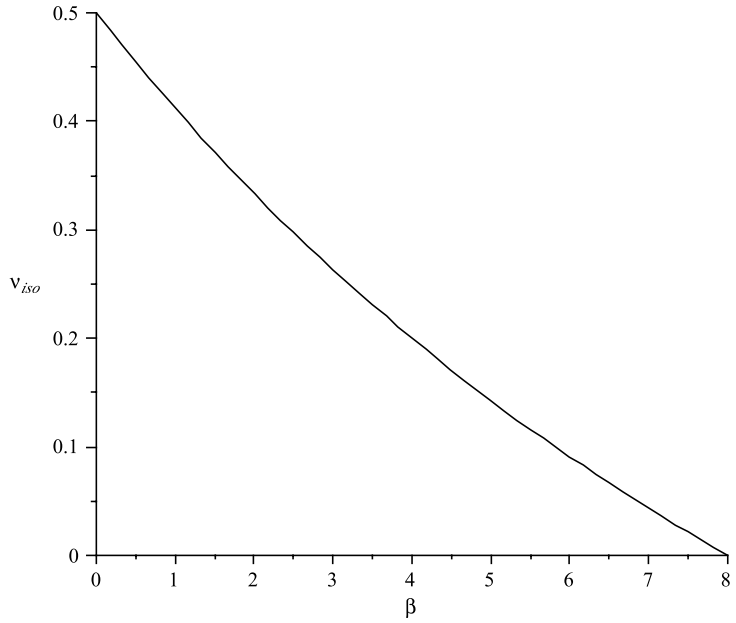

Figure 4.20. The isotropic Poisson's ratio as a function of dimensionless material constant β in the EP model.

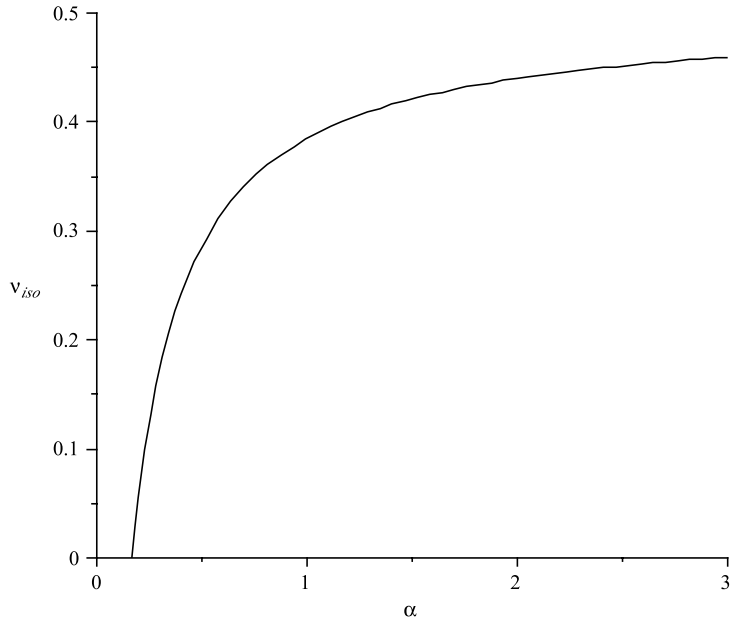

Figure 4.21. The isotropic Poisson's ratio as a function of dimensionless material constant α in the HAR model.

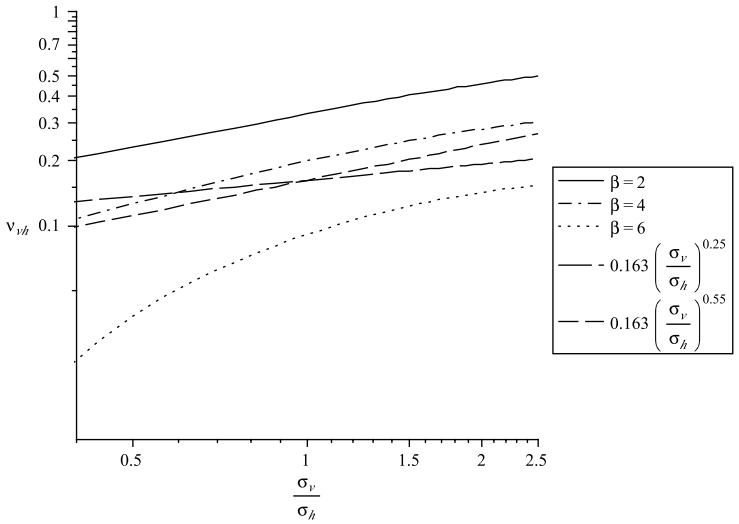

Figure 4.22. Poisson's ratio, ν_{vh}, as a function of the stress ratio σ_v/σ_h, for the EP model.

For anisotropic stress states, ν_{ij} varies with the stress ratio. From equation 4.25, we obtain

$$\nu_{vh} = \frac{(6-\beta)\left(\frac{\sigma_v}{\sigma_h}\right)^2 + (48-4\beta)\left(\frac{\sigma_v}{\sigma_h}\right) + 18 - 4\beta}{(\beta+6)\left(\frac{\sigma_v}{\sigma_h}\right)^2 + (4\beta+36)\left(\frac{\sigma_v}{\sigma_h}\right) + 4\beta + 102} \tag{4.29}$$

for the EP model, and

$$\nu_{vh} = \frac{\left(18\alpha^2-3\alpha-1\right)\left(\frac{\sigma_v}{\sigma_h}\right)^2 + \left(-36\alpha^2+51\alpha-4\right)\left(\frac{\sigma_v}{\sigma_h}\right) + 18\alpha^2+6\alpha-4}{(36\alpha^2+12\alpha+1)\left(\frac{\sigma_v}{\sigma_h}\right)^2 + (-72\alpha^2+12\alpha+4)\left(\frac{\sigma_v}{\sigma_h}\right) + 36\alpha^2+84\alpha+4} \tag{4.30}$$

for the HAR model. These are plotted along with observed experimental relationships in figures 4.22 and 4.23. The EP model indicates that ν_{vh} has close to a power law variation with σ_v/σ_h, except for large values of β (e.g. $\beta = 6$), though such low values of Poisson's ratio are not observed in practice. The power law scaling is closer to the value 0.55, observed in some experiments, than 0.25. The HAR model deviates slightly from this power law scaling, with curves similarly steeper than $(\sigma_v/\sigma_h)^{0.25}$. They also have a peak for relatively high values of the stress ratio (~ 2), after which ν_{vh} decreases slightly. No such trend is discernible from the experiment data.

4.3.3 Shear Modulus

It is apparent from the comparisons of Young's modulus and Poisson's ratio that of the three hyperelastic models considered, the EP model seems to best capture the physics observed experimentally. Finally, we consider the shear modulus obtained from the models and experiments. This is frequently measured by shear

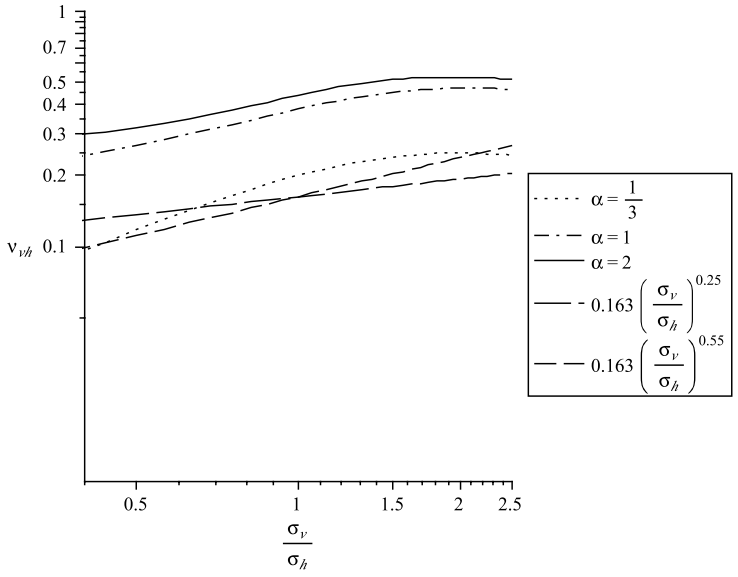

Figure 4.23. Poisson's ratio, ν_{vh}, as a function of the stress ratio σ_v/σ_h, for the HAR model.

wave propagation [42, 47, 55], often in a triaxial geometry. The shear modulus is identified as

$$G_{ij} = \frac{\delta\tau_{ij}}{\delta\gamma_{ij}} = \frac{1}{\dfrac{\partial^2\mathcal{G}}{\partial\tau_{ij}^2}} \tag{4.31}$$

according to equation 4.6. This results in a shear modulus for the EP model of

$$G = \frac{\sqrt{BP}}{4} \tag{4.32}$$

and for the HAR model,

$$G = \frac{\sqrt{3A}\left(\frac{1}{\alpha}P^2 + \sigma_s^2\right)^{\frac{5}{4}}}{2\left(\tau_4^2 + \frac{1}{\alpha}P^2 + \sigma_s^2\right)} \tag{4.33}$$

There is no stress-induced anisotropy in the shear moduli in either case, i.e.

$$G = G_{12} = G_{23} = G_{13} \tag{4.34}$$

In the EP model, the shear modulus simply depends on the square root of the mean normal stress P. This, of course, was the idea behind all the hyperelastic forms presented here, and the shear modulus (just as with the bulk and Young's moduli) is indeed found to vary with the square root of pressure [40, 42, 55]. Roesler [42] and others [47, 55, 57], however, find a more specific relationship between the shear modulus and stress; they find that the shear modulus does not depend on the normal stress acting on the plane of shear, e.g.

$$G_{12} \neq f(\sigma_3) \tag{4.35}$$

This independence is illustrated by the shear wave measurements of Roesler ([42], figure 4.24). More specifically, they find that

$$G_{12} \sim (\sigma_1\sigma_2)^{\frac{1}{4}} \tag{4.36}$$

Thus the shear modulus still varies with the square root of the mean stress (figure 4.25), but the EP model predicts an equal dependence of the shear modulus on each component of normal stress (figure 4.26). This is a notable shortcoming of the EP model, but is present also in the HAR model. The HAR model also gives a shear modulus that is a function of the shear stresses. HongNam et al. [57] have made measurements where one shear stress component is non-zero, and the normal stresses are isotropic, e.g.

$$\sigma \equiv \sigma_1 = \sigma_2 = \sigma_3 \tag{4.37}$$

$$\tau \equiv \tau_4 \tag{4.38}$$

$$\tau_5 = \tau_6 = 0 \tag{4.39}$$

This gives, for the HAR model,

$$G = \frac{\sqrt{3A}}{2}\frac{\left(\frac{1}{\alpha}\sigma^2 + 2\tau^2\right)^{\frac{5}{4}}}{\left(\frac{1}{\alpha}\sigma^2 + 3\tau^2\right)} \tag{4.40}$$

Figure 4.27 shows that the HAR shear modulus has only a small dependence on the shear stress τ, either increasing or decreasing depending on the value of α; HongNam et al. find little variation in the shear modulus with shear stress (figure 4.28).

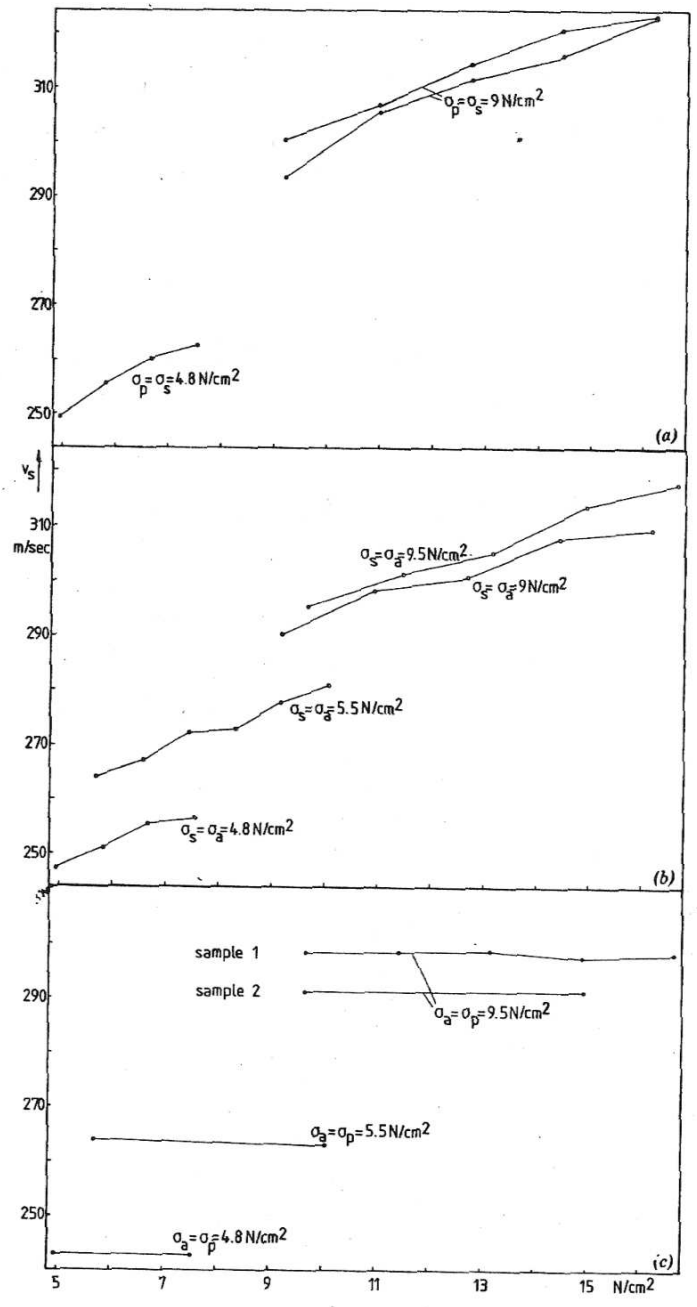

Figure 4.24. Shear wave velocities, from [42] (with permission from ASCE), as a function of each of the normal stresses, here labeled σ_a, σ_p, and σ_s. The shear modulus ($\sim v_s$) is independent of the normal stress in the planes of shear, σ_s.

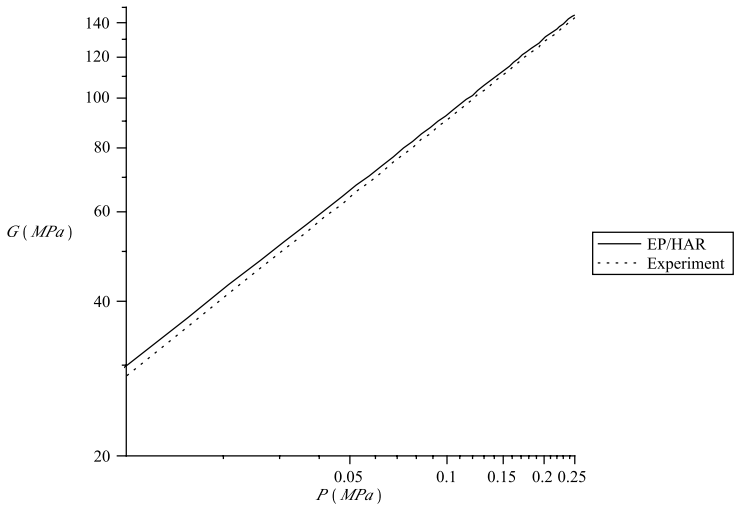

Figure 4.25. The shear modulus as a function of pressure, for isotropic stress. Here the EP and HAR models are identical, with $\sigma_s = 0$, and $\sqrt{B}/4 = \sqrt{3A}/2\alpha^{1/4} = 286.6\ MPa^{1/2}$. The experiment fit [55] is $G_{hh} = 286.6\sigma_v^{-0.04}\sigma_h^{0.53}$.

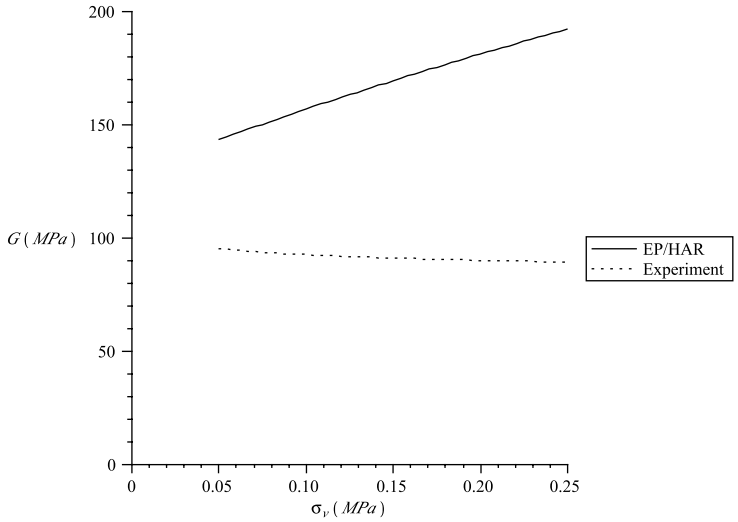

Figure 4.26. The shear modulus G_{hh} as a function of the vertical stress σ_v. Here the EP and HAR models are identical, with $\sigma_s = 0$, and $\sqrt{B}/4 = \sqrt{3A}/2\alpha^{1/4} = 286.6\ MPa^{1/2}$. The experiment fit [55] is $G_{hh} = 286.6\sigma_v^{-0.04}\sigma_h^{0.53}$.

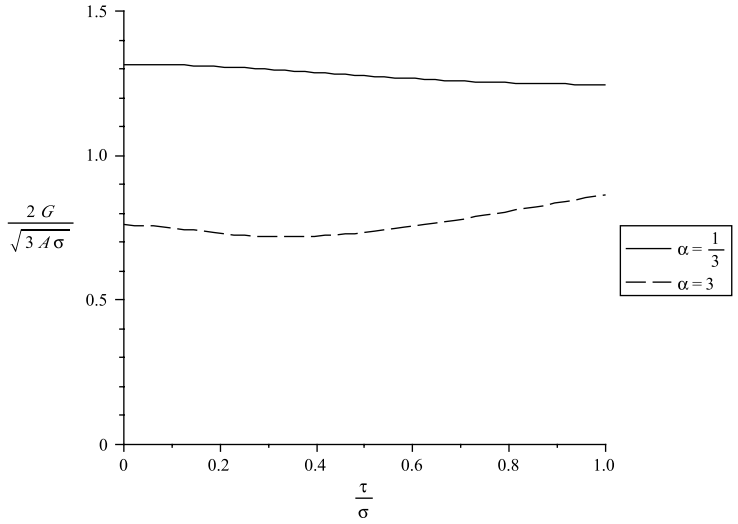

Figure 4.27. The effect of shear stress τ on the shear modulus in the HAR model.

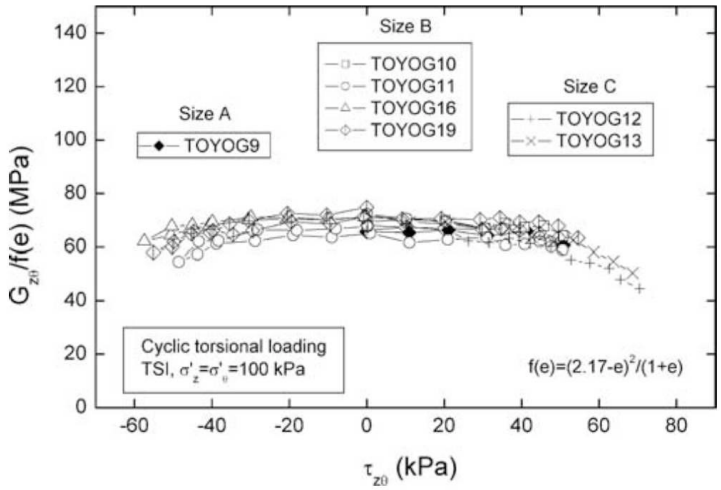

Figure 4.28. The effect of shear stress on the shear modulus [57]. No significant trend is identified; the decreasing values at larger shear are attributed to increasing plastic deformations. Reprinted, with permission, from the Geotechnical Testing Journal, Vol. 19, No. 4, copyright ASTM International, 100 Barr Harbor Drive, West Conshohocken, PA 19428.

5 Stress Distributions

GE has been implemented in finite element codes and employed to calculate stress distributions in sand piles [25], silos, and granular layers subject to a point load [71], and agrees relatively well with experiment data. As the EP model provides better analytical results for the elastic moduli, without the over-constraint on the yield angle of GE, we shall similarly implement it in the finite element code Abaqus [100] and test it against experiment data and published results of GE, along with the HAR model.

5.1 Abaqus Implementation of Non-linear Elastic Models

One may implement any desired material behavior in Abaqus through the user material (UMAT) subroutine. In the present case of non-linear, small strain elasticity, this simply requires providing the stiffness matrix, and updating the stresses. For GE and HAR, this is straightforward; as both possess a closed form of the Helmholtz free energy, the stiffness matrix may be obtained by differentiating:

$$M_{ijk\ell} = \frac{\partial^2 \mathcal{F}}{\partial u_{ij} \partial u_{k\ell}} \tag{5.1}$$

For the EP model, differentiating the Gibbs free energy gives the compliance matrix,

$$C_{ijk\ell} = \frac{\partial^2 \mathcal{G}}{\partial \sigma_{ij} \partial \sigma_{k\ell}} \tag{5.2}$$

The compliance matrix must be inverted to obtain the stiffness matrix for Abaqus, which gives the stiffness matrix in terms of the stresses, whereas the stiffness matrix obtained directly from the Helmholtz free energy in GE and HAR is a function of the strains. Either is equally acceptable for Abaqus. The three problems of interest can all be treated with either plane strain or axisymmetric simplifications, in which there is only one component of shear stress and shear strain. Additional plane stress and 3D implementations of the EP model are given in appendices F.4 and F.5. For the axisymmetric case, the EP compliance matrix simplifies to

$$C_{ij} = \begin{bmatrix} & & & \frac{2\tau_4}{3\sqrt{BP^3}} \\ & \hat{C} & & \frac{2\tau_4}{3\sqrt{BP^3}} \\ & & & \frac{2\tau_4}{3\sqrt{BP^3}} \\ \frac{2\tau_4}{3\sqrt{BP^3}} & \frac{2\tau_4}{3\sqrt{BP^3}} & \frac{2\tau_4}{3\sqrt{BP^3}} & \frac{4}{\sqrt{BP}} \end{bmatrix} \tag{5.3}$$

with

$$\hat{C}_{ij} = \frac{1}{12\sqrt{BP}} \left(\frac{\sigma_s^2}{P^2} + \frac{4(\sigma_i + \sigma_j)}{P} + \beta + 24\delta_{ij} \right) \tag{5.4}$$

and its inverse is

$$M = \sqrt{BP}\begin{bmatrix} & \hat{M} & \begin{matrix}\frac{\tau_4(P-\sigma_1)}{(3\beta P^2+\sigma_s^2)}\\ \frac{\tau_4(P-\sigma_2)}{(3\beta P^2+\sigma_s^2)}\\ \frac{\tau_4(P-\sigma_3)}{(3\beta P^2+\sigma_s^2)}\end{matrix} \\ \frac{\tau_4(P-\sigma_1)}{(3\beta P^2+\sigma_s^2)} & \frac{\tau_4(P-\sigma_2)}{(3\beta P^2+\sigma_s^2)} & \frac{\tau_4(P-\sigma_3)}{(3\beta P^2+\sigma_s^2)} & \frac{\left(4\tau_4^2+3\beta P^2+\sigma_s^2\right)}{4(3\beta P^2+\sigma_s^2)} \end{bmatrix} \tag{5.5}$$

with

$$\hat{M} = \begin{bmatrix} \frac{\left(3(P-\sigma_1)^2+3\beta P^2+\sigma_s^2\right)}{3(3\beta P^2+\sigma_s^2)} & \frac{\left(6(P-\sigma_1)(P-\sigma_2)-3\beta P^2-\sigma_s^2\right)}{6(3\beta P^2+\sigma_s^2)} & \frac{\left(6(P-\sigma_1)(P-\sigma_3)-3\beta P^2-\sigma_s^2\right)}{6(3\beta P^2+\sigma_s^2)} \\ \frac{\left(6(P-\sigma_2)(P-\sigma_1)-3\beta P^2-\sigma_s^2\right)}{6(3\beta P^2+\sigma_s^2)} & \frac{\left(3(P-\sigma_2)^2+3\beta P^2+\sigma_s^2\right)}{3(3\beta P^2+\sigma_s^2)} & \frac{\left(6(P-\sigma_2)(P-\sigma_3)-3\beta P^2-\sigma_s^2\right)}{6(3\beta P^2+\sigma_s^2)} \\ \frac{\left(6(P-\sigma_3)(P-\sigma_1)-3\beta P^2-\sigma_s^2\right)}{6(3\beta P^2+\sigma_s^2)} & \frac{\left(6(P-\sigma_3)(P-\sigma_2)-3\beta P^2-\sigma_s^2\right)}{6(3\beta P^2+\sigma_s^2)} & \frac{\left(3(P-\sigma_3)^2+3\beta P^2+\sigma_s^2\right)}{3(3\beta P^2+\sigma_s^2)} \end{bmatrix} \tag{5.6}$$

The Abaqus UMAT subroutine for EP plane strain and axisymmetric stress is given in appendix F.2. For GE, the stiffness matrix is

$$M = \tilde{G}\begin{bmatrix} \frac{38\Delta^2-24\Delta u_1-3u_s^2}{12\Delta^{\frac{3}{2}}} & \frac{14\Delta^2-12\Delta(u_1+u_2)-3u_s^2}{12\Delta^{\frac{3}{2}}} & \frac{14\Delta^2-12\Delta(u_1+u_3)-3u_s^2}{12\Delta^{\frac{3}{2}}} & \frac{-\gamma_4}{2\sqrt{\Delta}} \\ \frac{14\Delta^2-12\Delta(u_2+u_1)-3u_s^2}{12\Delta^{\frac{3}{2}}} & \frac{38\Delta^2-24\Delta u_2-3u_s^2}{12\Delta^{\frac{3}{2}}} & \frac{14\Delta^2-12\Delta(u_2+u_3)-3u_s^2}{12\Delta^{\frac{3}{2}}} & \frac{-\gamma_4}{2\sqrt{\Delta}} \\ \frac{14\Delta^2-12\Delta(u_3+u_1)-3u_s^2}{12\Delta^{\frac{3}{2}}} & \frac{14\Delta^2-12\Delta(u_3+u_2)-3u_s^2}{12\Delta^{\frac{3}{2}}} & \frac{38\Delta^2-24\Delta u_3-3u_s^2}{12\Delta^{\frac{3}{2}}} & \frac{-\gamma_4}{2\sqrt{\Delta}} \\ \frac{-\gamma_4}{2\sqrt{\Delta}} & \frac{-\gamma_4}{2\sqrt{\Delta}} & \frac{-\gamma_4}{2\sqrt{\Delta}} & \sqrt{\Delta} \end{bmatrix} \tag{5.7}$$

with the UMAT subroutine given in appendix F.1; for the HAR model,

$$M = A\begin{bmatrix} & \hat{M}_{ij} & \begin{matrix}\frac{-\gamma_4((3\alpha-1)\Delta-3u_1)}{2\sqrt{\alpha\Delta^2+u_s^2}}\\ \frac{-\gamma_4((3\alpha-1)\Delta-3u_2)}{2\sqrt{\alpha\Delta^2+u_s^2}}\\ \frac{-\gamma_4((3\alpha-1)\Delta-3u_3)}{2\sqrt{\alpha\Delta^2+u_s^2}}\end{matrix} \\ \frac{-\gamma_4((3\alpha-1)\Delta-3u_1)}{2\sqrt{\alpha\Delta^2+u_s^2}} & \frac{-\gamma_4((3\alpha-1)\Delta-3u_2)}{2\sqrt{\alpha\Delta^2+u_s^2}} & \frac{-\gamma_4((3\alpha-1)\Delta-3u_3)}{2\sqrt{\alpha\Delta^2+u_s^2}} & \frac{\frac{1}{2}\gamma_4^2+\alpha\Delta^2 ls+u_s^2}{2\sqrt{\alpha\Delta^2+u_s^2}} \end{bmatrix} \tag{5.8}$$

where the diagonal terms $\hat{M}_{ii}$ (no summation implied) are given by

$$\hat{M}_{ii} = \frac{\left(18\alpha^2+1\right)\Delta^2 + (9\alpha+6)\,u_s^2 + 6\,(1-3\alpha)\,\Delta u_i + 9u_i^2}{3\sqrt{\alpha\Delta^2+u_s^2}} \tag{5.9}$$

and the off diagonal terms by

$$\hat{M}_{ij} = \frac{(3-9\alpha)\left(\Delta\,(u_i+u_j)-u_s^2\right) + 9\left(u_iu_j+\alpha\Delta^2\,(2\alpha-1)\right)}{3\sqrt{\alpha\Delta^2+u_s^2}} \tag{5.10}$$

The HAR UMAT subroutine is given in appendix F.3.

5.2 Abaqus UMAT Benchmarks

As a benchmark for the subroutines, we investigate some constant strain cases, for which analytical results may be readily obtained ($u_{ij} = \partial\mathcal{G}/\partial\sigma_{ij}$, or $\sigma_{ij} = \partial\mathcal{F}/\partial u_{ij}$) and compare with single-element results from

σ_1	σ_2	Analytical	Abaqus
1000	500	σ_3 = -4.122e2 u_1 = -1.424e-5 u_2 = -2.127e-6	σ_3 = -4.122e2 u_1 = -1.425e-5 u_2 = -2.129e-6
1000	1000	σ_3 = -5.2e2 u_1 = -1.034e-5 u_2 = -1.034e-5	σ_3 = -5.200e2 u_1 = -1.035e-5 u_2 = -1.035e-5
1000	1500	σ_3 = -6.628e2 u_1 = -6.796e-6 u_2 = -1.687e-5	σ_3 = -6.628e2 u_1 = -6.801e-6 u_2 = -1.689e-5

Table 5.1. Abaqus GE results for a single quadratic, reduced integration, plane strain element.

Abaqus. For the EP and HAR models, $\alpha = 1$, $\beta = 3$ and $A = B = 1e11$ (arbitrary units), and various normal forces are applied in each direction. A square element is tested for the plane strain case (tables 5.1, 5.2, and 5.4); a rectangular element for axisymmetric stress (the triaxial test, table 5.3). Abaqus results agree well with analytical values provided that the loads are applied in reasonably small increments; 0.001-0.0001 of the total time is used here. Since the stresses and strains are initially zero, $1/P$ and $1/\Delta$ terms in the stiffness matrix will result in floating point errors due to division by zero in the first time step, or if tension is present at any point in the problem. This necessitates restricting P and Δ to some small, non-zero, positive value. The value itself does not affect the result provided this initial increment is small; $1e-6$ is used here.

5.3 Sand Piles and the Stress Dip

Next we turn our attention to the sand pile experiments of Vanel et al. [19]. Recall that they found a stress dip in conical and wedge shaped piles poured from a point source, but not for those poured rain-like from a sieve. GE reasonably matches the cases without a stress dip [25], so we shall make the same comparison with the EP and HAR models here. Note that GE produced a stress dip when a non-uniform density was applied, with a lower density center core; this is a plausible explanation for the stress dip, but quantitatively the result is not particularly meaningful, as the density distribution was arbitrary. The piles considered by Vanel et al. are 8 cm high, 26 cm in diameter or width, and 20 cm thick in the case of the wedge. The density of the material is not reported, and results are normalized with respect to it. Following Krimer et al. [25], the density is taken here to be 2660 kg/m^3, typical of the sand used in experiments [55]. At the bottom of the pile, the r and z displacements are set to zero. In addition to gravity, a small pressure is applied to the free surface at the top of the pile. Though analytically stable, at the surface where $P = 0$, the $1/P$ and $1/\Delta$ terms in the stiffness matrix diverge. The pressure applied at the surface ensures numerical stability, but does

σ_1	σ_2	Analytical	Abaqus
1000	500	σ_3 = -1.902e2 u_1 = -2.158e-4 u_2 = -8.254e-5	σ_3 = -1.894e2 u_1 = -2.179e-4 u_2 = -8.336e-5
1000	1000	σ_3 = -2.301e2 u_1 = -1.786e-4 u_2 = -1.786e-4	σ_3 = -2.290e2 u_1 = -1.803e-4 u_2 = -1.803e-4
1000	1500	σ_3 = -2.983e2 u_1 = -1.453e-4 u_2 = -2.488e-4	σ_3 = -2.969e2 u_1 = -1.467e-4 u_2 = -2.513e-4

Table 5.2. Abaqus EP results for a single quadratic, reduced integration, plane strain element.

$\sigma_1 = \sigma_3$	σ_2	Analytical	Abaqus
1000	500	u_1 = -1.698e-4 u_2 = -6.025e-5	u_1 = -1.714e-4 u_2 = -6.083e-5
1000	1000	u_1 = -1.5e-4 u_2 = -1.5e-4	u_1 = -1.514e-4 u_2 = -1.514e-4
1000	1500	u_1 = -1.290e-4 u_2 = -2.215e-4	u_1 = -1.302e-4 u_2 = -2.237e-4

Table 5.3. Abaqus EP results for a single quadratic, reduced integration, axisymmetric stress element.

σ_1	σ_2	Analytical	Abaqus
1000	500	σ_3 = -4.286e2 u_1 = -3.737e-5 u_2 = -4.672e-6	σ_3 = -4.286e2 u_1 = -3.741e-5 u_2 = -4.676e-6
1000	1000	σ_3 = -5.714e2 u_1 = -2.572e-5 u_2 = -2.572e-5	σ_3 = -5.714e2 u_1 = -2.574e-5 u_2 = -2.574e-5
1000	1500	σ_3 = -7.143e2 u_1 = -1.500e-5 u_2 = -4.124e-5	σ_3 = -7.143e2 u_1 = -1.501e-5 u_2 = -4.127e-5

Table 5.4. Abaqus HAR results for a single quadratic, reduced integration, plane strain element.

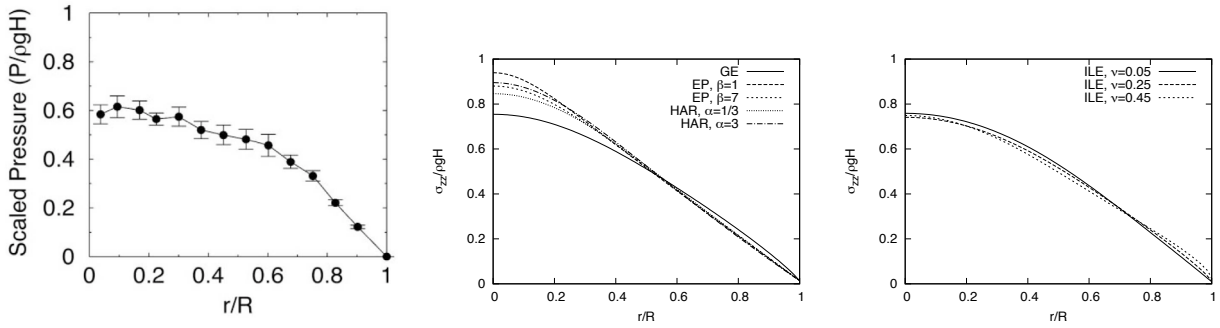

Figure 5.1. Experimental (left: reprinted figure with permission from [101], copyright 1999 by the American Physical Society) and Abaqus (center, right) results for the stress at the bottom of a conical sand pile.

not impact the stress distributions away from the surface in any meaningful way, provided it is sufficiently small (10-20 Pa is used here). This is the same method employed in calculating stress distributions with GE [25, 71]. Note, however, that this creates a problem if the objective is to predict yielding in the pile. Say, for example, that a pile is sufficiently steep that shear stresses exceed a critical fraction of the normal stresses, and we expect yielding to occur. Application of an additional normal stress at the surface will lower the stress ratio and provide stability in this case as well. This is particularly problematic in GE, where there is a thermodynamic limit on the stress ratio; it is worth noting that while the GE yield angle can be at most 26.5°, the model is applied to 33° sand piles without difficulty, presumably due to this additional normal force.

Unlike GE, in which ξ is fixed by the maximum yield angle, we are free to pick the values of the material constants α and β. The same applies to A and B, though their values are not relevant for the current comparison; they scale the strains but do not change the stresses. Lacking any strain measurements from the current experiments, their value cannot be determined. The stress distribution for conical piles is shown in figure 5.1 along with experiment data; plane strain results for wedge-shaped piles are compared to experimental results and GE calculations in figure 5.2. As we are free to choose α and β in the HAR and EP models, several different values are tried for both conical and wedge-shaped piles. Their values do not strongly influence the stress distribution at the bottom of the pile in either case. The increase in stress from the edge of the pile toward the center is quite linear, as opposed to the experiments in which there is a significant leveling off. GE provides slightly more realistic profiles for both conical and wedge-shaped piles, though it still slightly overestimates the peak height. Interestingly, none of the non-linear models is appreciably different from isotropic linear elasticity (ILE) in this case; ILE is similarly independent of Young's modulus E, and only weakly dependent on Poisson's ratio ν. It gives a better match to experiment data than the EP and HAR models, particularly for the conical pile, though it still overestimates the peak height. Of course, when poured from a funnel, there is a stress *dip* at the center; whether due to density inhomogeneity or some other effect, the flattening of the curves for the sieved piles might be due to a similar,

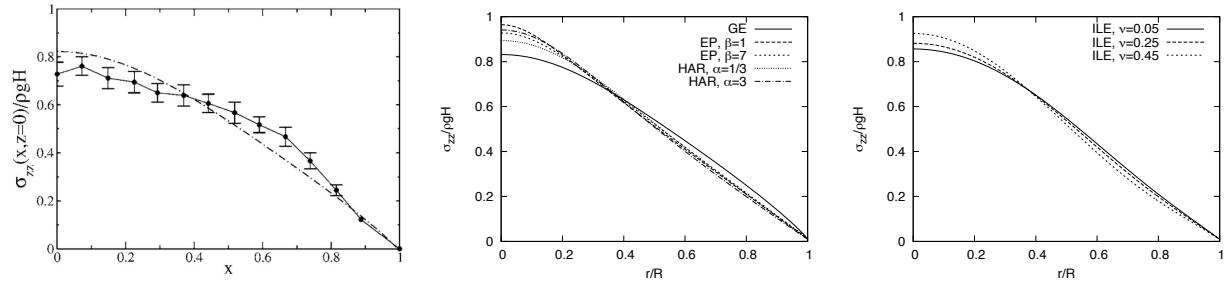

Figure 5.2. Experimental (left, points), GE (left, dashed line), and Abaqus (center, right) plane strain results for the stress at the bottom of a sand wedge. Left figure reprinted with permission from [25]. Copyright 1999 by the American Physical Society.

but less pronounced, effect; without any knowledge of the actual density distribution, it is difficult to draw any further conclusions from this case.

5.4 The Janssen Silo Problem

A widely used approximate method for stress calculations in cylindrical silos was developed by Janssen [30]. He assumes that a vertical force applied to a cylindrical slice generates a proportional horizontal force $k_J\sigma_{zz}$, i.e.

$$\sigma_{rr} = k_J\sigma_{zz} \tag{5.11}$$

and furthermore that the horizontal wall friction is "fully mobilized", and takes the maximum possible amount of static friction,

$$\tau_{rz} = \mu_f\sigma_{rr} = \mu_f k_J\sigma_{zz} \tag{5.12}$$

As noted by de Gennes [1] and Duran [14], this is questionable, since the shear may take *any* value less than this maximum. Under these assumptions, a horizontal slice of area A is subject to a downward force due to its own weight of $\rho gAdz$, where we take $z = 0$ at the top surface of the silo, and upward forces due to the change in pressure and wall friction of $Ad\sigma_{zz}$ and $k_J\mu_f p\sigma_{zz}dz$, respectively, where p is the perimeter of the silo. So we may write the force balance

$$Ad\sigma_{zz} + k_J\mu_f p\sigma_{zz}dz = \rho gAdz \tag{5.13}$$

or

$$\frac{d\sigma_{zz}}{dz} = \rho g - k_J\mu_f\frac{p}{A}\sigma_{zz} = \rho g - \frac{2k_J\mu_f}{R}\sigma_{zz} \tag{5.14}$$

for silo radius R. This leads to a solution for σ_{zz} [1, 9, 14]

$$\sigma_{zz} = \frac{\rho gR}{2k_J\mu_f}\left(1 - exp\left(\frac{-2k_J\mu_f}{R}z\right)\right) + \sigma_0 exp\left(\frac{-2k_J\mu_f}{R}z\right) \tag{5.15}$$

where σ_0 is the vertical stress at $z = 0$, the top of the silo. In practice this is zero, but again we take a small normal force to ensure numerical stability. 100 Pa is sufficient for this purpose in the present case, much

smaller than even the value reported by Bräuer et al. [71]. The analytical form above results in a vertical pressure saturating with depth, in contrast with the usual "hydrostatic pressure". The Janssen coefficient k_J is frequently assumed to obey the empirical formula [31, 102, 103]

$$k_J = \sin\phi \tag{5.16}$$

Bräuer et al. [71] have performed calculations for a silo with wall friction and find the Janssen model well matched by GE, with σ_{zz} saturating for large depths z, and the ratio σ_{rr}/σ_{zz} becoming approximately constant; they find $k_J \sim 0.4$. With $\xi = 5/3$ fixed by the yield angle, the Janssen constant is fixed as well, though it is in practice found to vary by material [104]. The Abaqus implementation of GE produces results consistent with published values, which are shown in figure 5.3.

The EP and HAR models essentially produce the same behavior, see figure 5.4. Here the silo dimensions are $H = 36$ m and $R = 1$ m, with a wall friction coefficient μ_f =0.2. This is a very tall, narrow "silo", but such dimensions are necessary to observe the "saturating" behavior. The Janssen model for σ_{zz} at the top of each figure is equation 5.15, with the value of k_J taken from the numerical results at the point $r/R = 0.5$ and $z/H = 0.5$. There is slightly more variation in $k_J = \sigma_{rr}/\sigma_{zz}$ radially, particularly for the EP model; note the larger scale in figure 5.4. As reported for GE , the friction coefficient does not strongly influence the value of k_J, see figure 5.5.

While k_J is fixed at ~ 0.4 for GE, in the EP and HAR models, we are free to choose β and α. The results are qualitatively similar to those in figure 5.4, but with k_J dependent on β or α. The relationships (shown in figure 5.6) are similar to the variation of the isotropic Poisson's ratio, ν_{iso}, obtained analytically (equations 4.27-4.28) and plotted in figures 4.20-4.21. That the Janssen concept of "vertical force redirection" is related to Poisson's ratio is perhaps not surprising; indeed, for isotropic linear elasticity, Ovarlez et al. [105] obtain for large z

$$k_J = \frac{\nu}{1-\nu} \tag{5.17}$$

As isotropic linear elasticity successfully reproduces that Janssen model, perhaps a better test of any model for granular statics is a variation on the Janssen problem that his model, and ILE, fail to reproduce. There has been some recent experimental work on the silo problem [101, 105–107], and one such effect has been clearly identified. Consider the case in which a pressure equal to the saturation stress is applied at the surface of the silo. The Janssen model, equation 5.15, gives $\sigma_{zz}/\sigma_{sat} = 1$, independent of z. In the experiments, there is a significant "overshoot" of the saturated value, up to 20% ([105, 107], figure 5.7). While ILE similarly produces an overshoot, it is 30-40 times smaller than the one observed experimentally, what Ovarlez et al. refer to as a "giant overshoot effect" [105]. They go on to speculate that stress-induced anisotropy may play a role in the overshoot, with a greater stiffness in the vertical direction due to the applied load. As the hyperelastic models possess stress-induced anisotropy, the EP model in particular producing stress-induced anisotropy in relative agreement with measurements of stress-dependent elastic moduli, we

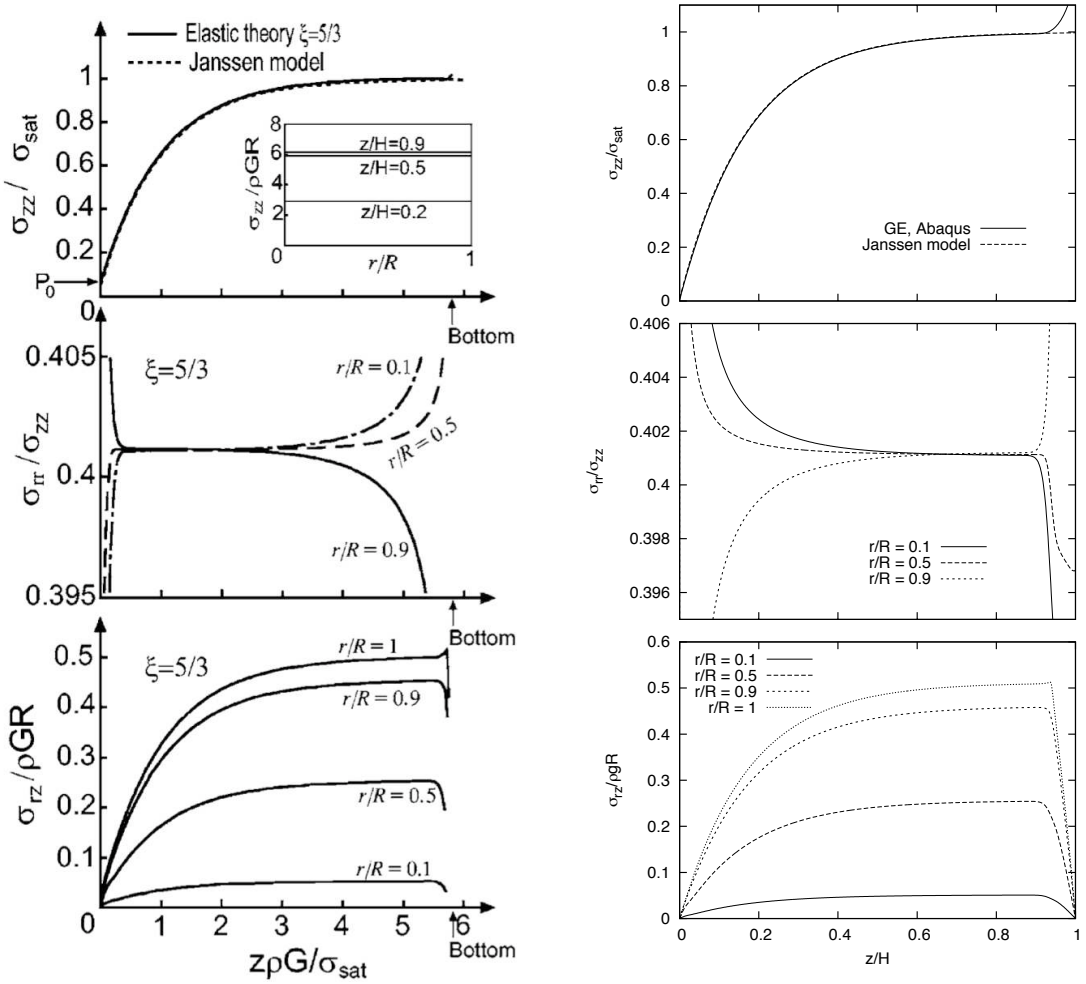

Figure 5.3. Published GE results for silo stresses (left), and Abaqus implementation (right). Note the published result for the Janssen constant is plotted backwards, from bottom to top. Left figure reprinted with permission from [71]. Copyright 1999 by the American Physical Society.

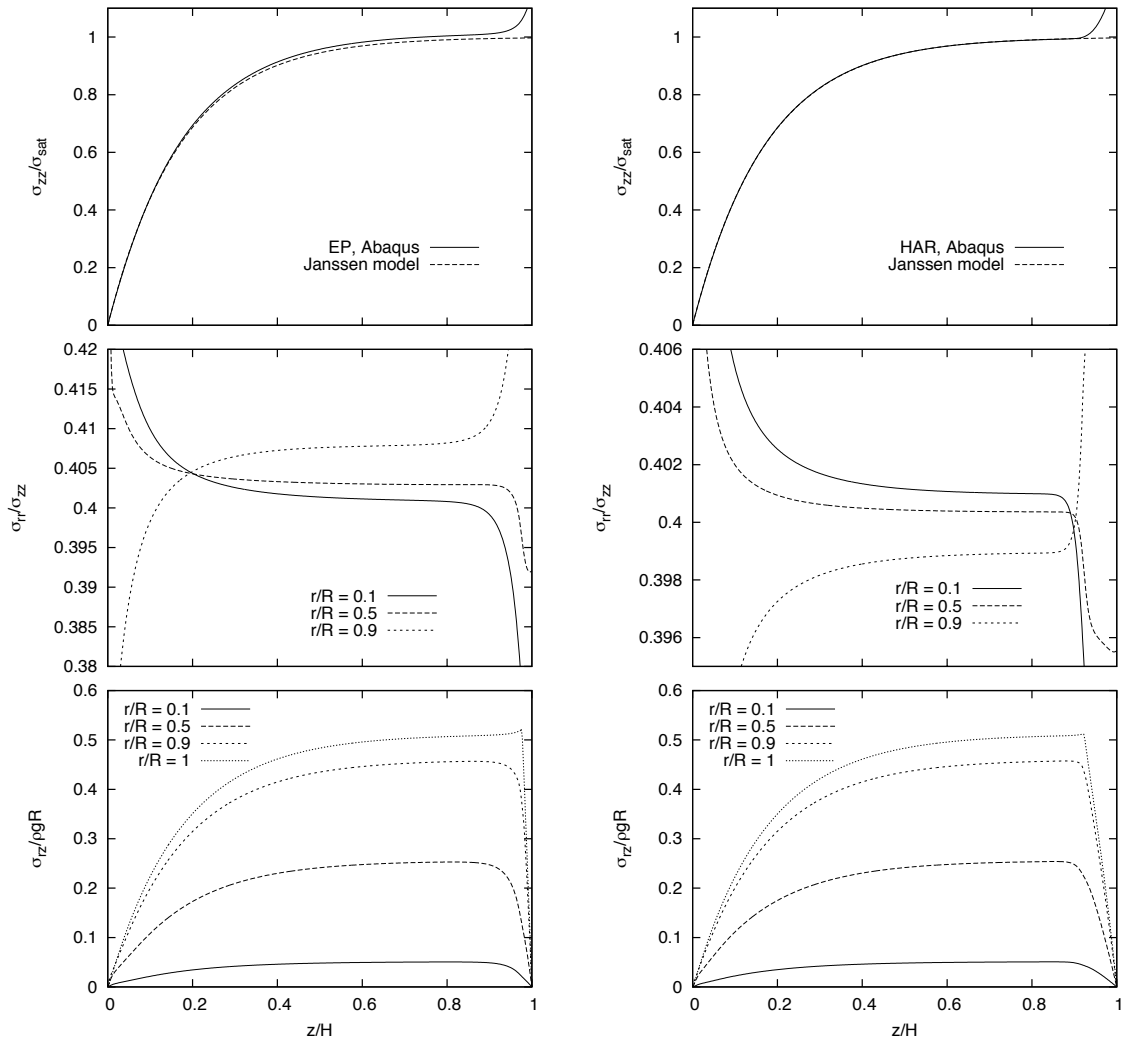

Figure 5.4. Abaqus results for silo stresses using the EP model ($\beta = 3/2$, left) and HAR model ($\alpha = 1$, right).

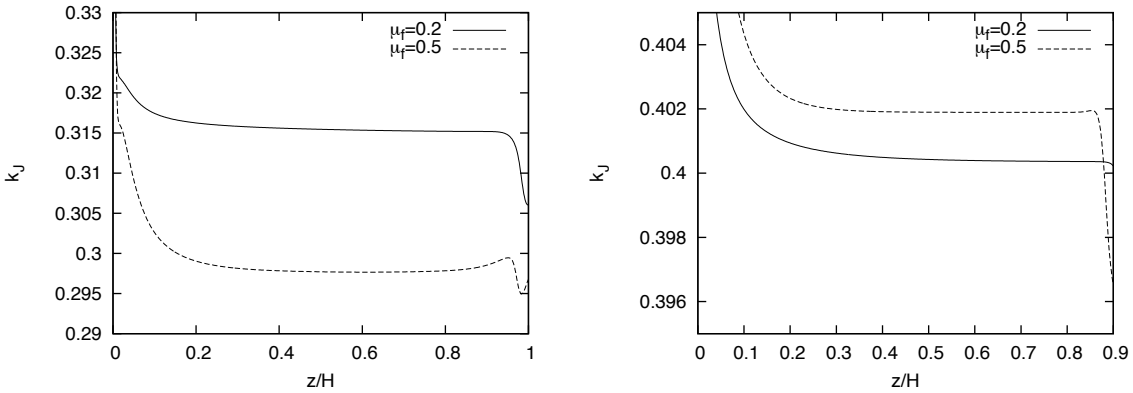

Figure 5.5. The Janssen constant for different friction coefficients: EP model ($\beta = 2$, left) and HAR model ($\alpha = 1$, right).

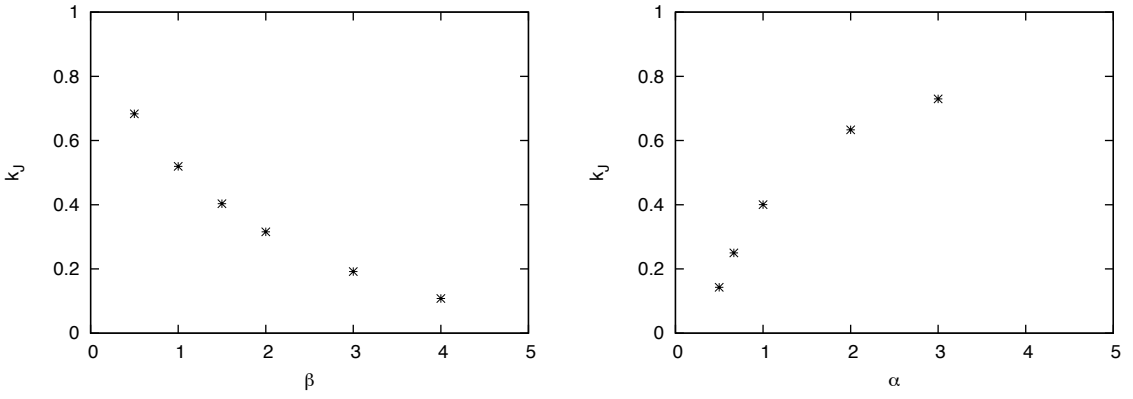

Figure 5.6. Janssen's constant as a function of the materials constant β for the EP model (left) and α for the HAR model (right). Values are taken at $r/R = 0.5$ and $z/H = 0.5$.

might expect them to reproduce the effect. But the Abaqus results reveal that the overshoot in all three hyperelastic models is closer to that predicted by linear elasticity than observed in experiments. The GE and HAR models produce similar results, while in the EP model the decrease to the saturated value is much more gradual than for any of the other elastic models.

In a subsequent paper, Ovarlez et al. [107]showed that anisotropic linear elasticity (ALE) similarly failed to account for the magnitude of the overshoot. Thus, it remains an open issue. As with the stress dip in sand piles, one wonders if density inhomogeneity might play a role here. In particular, it is more likely in this case that some rearrangement of grains is taking place when a stress equal to σ_{sat} is applied to the surface. Whether non-uniform density in the context of elasticity alone might resolve the discrepancy, i.e. the issue of whether irreversible, plastic deformations are still safely ignorable in this case, is not known.

5.5 Layer Under a Point Load

The response function or Green's function of a granular material subject to a localized force perturbation has been established as a simple test of granular mechanics. Here there was an interest in resolving whether or not such systems were governed by elliptic, parabolic, or hyperbolic equations. While hyperbolic equations (such as IFE and FPA) predict a double peaked response function in 2D and a "ring" peak in 3D (as the forces propagate along characteristics), elliptic equations predict a single peak, with the half width increasing linearly with depth. Parabolic equations similarly possess a single peak, but with the half width increasing as $\sqrt{h}$. While hyperbolic behavior can be observed in systems that are highly ordered (i.e. the particles are arranged in a lattice structure), frictionless, or far from the continuum limit, and parabolic behavior has been reported for another very particular arrangement, experiments find for frictional, disordered systems the behavior is invariably elliptic [24, 108–110].

The first point of comparison here is the analytical solution for an infinite elastic half space, due to Boussinesq [111] and Cerutti [112] (see also[28]). With a force F applied to a point on its surface,

$$\sigma_{zz} = \frac{3F}{2\pi} \frac{h^3}{(r^2 + h^2)^{\frac{5}{2}}} \tag{5.18}$$

Here and throughout, we report instead the renormalized value

$$C \equiv \frac{h^2 \sigma_{zz}}{F} = \frac{1}{\left(\frac{r^2}{h^2} + 1\right)^{\frac{5}{2}}} \tag{5.19}$$

such that

$$\int_0^\infty 2\pi C(r') r' dr' = 1 \tag{5.20}$$

Some experimental data are compared with the Boussinesq-Cerutti solution in figure 5.8. While the behavior is qualitatively similar, the magnitude of the peak depends strongly on the preparation of the layer.

The Boussinesq-Cerutti solution depends only on the perturbing force and position; it has no dependence on the elastic constants. A finite system should be qualitatively similar, but will have some dependence on

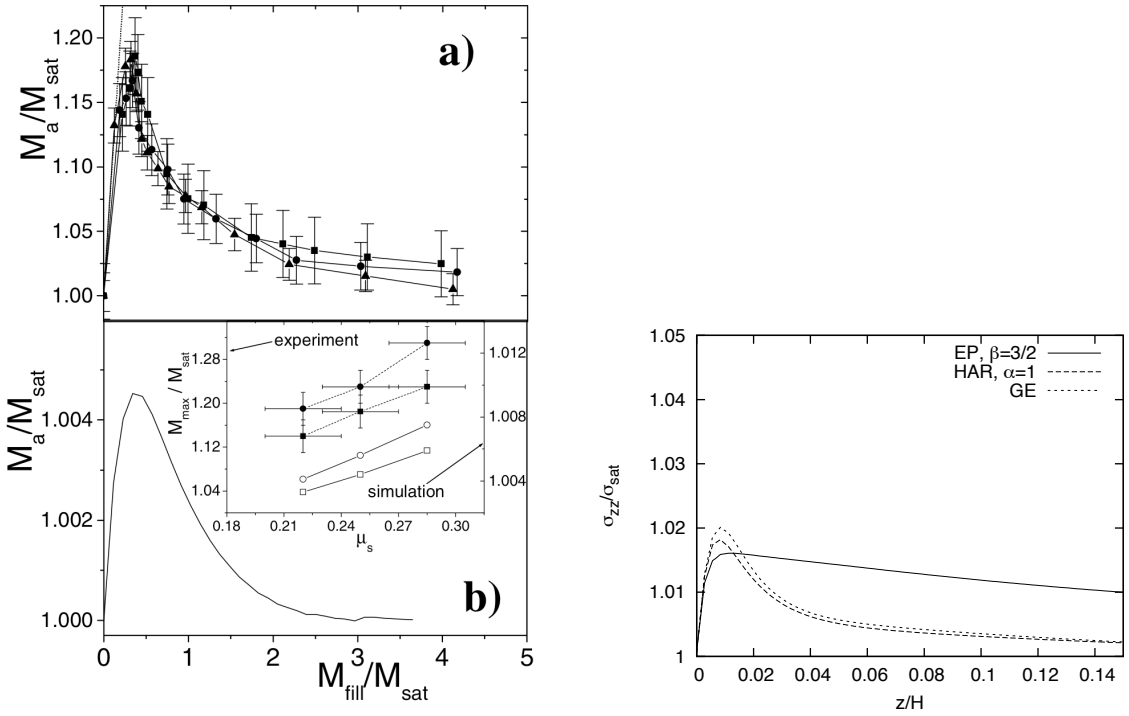

Figure 5.7. Experimental data (a) and linear elastic model (b) for the "overshoot" in stress when a load equal to σ_{sat} is applied to the surface of the silo (from [107], with kind permission from the European Physical Journal (EPL)). Hyperelastic models (right) similarly underestimate the overshoot; the decrease to the saturated value is much slower for the EP model.

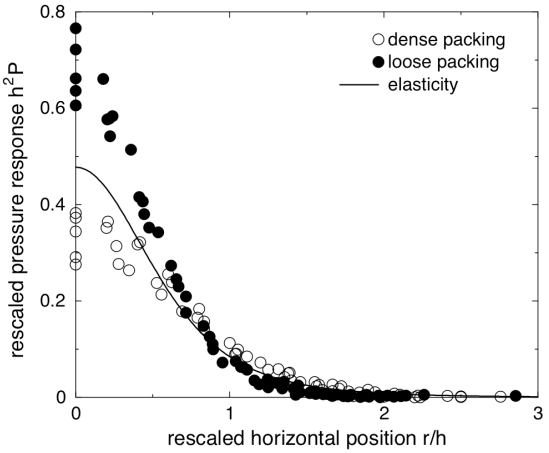

Figure 5.8. Experimental measurements of the response function for granular materials ([109], with kind permission from the European Physical Journal (EPL)). "Elasticity" here is the Boussinesq-Cerutti solution for an infinite half space.

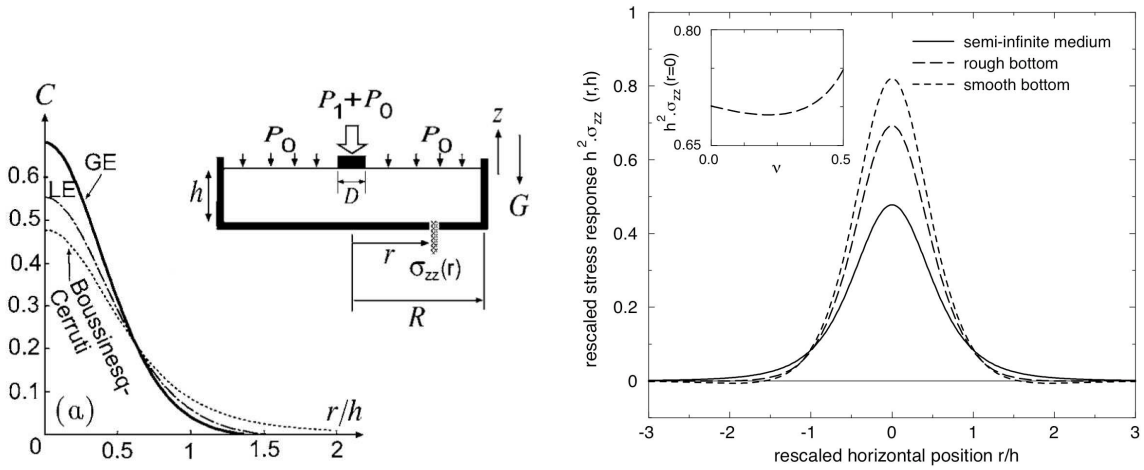

Figure 5.9. Calculations of the response function for GE (left) and linear elasticity (right). Note that the peak values for GE and ILE reported in [71] are lower than those reported in [109] and in the present work (see figure 5.10). Left figure reprinted with permission from [71], copyright 1999 by the American Physical Society. Right figure [109] reprinted with kind permission from the European Physical Journal (EPL).

the elastic constants (i.e. Poisson's ratio) and the applied boundary conditions. As the shape of the profile found in experiments indicates elliptic governing equations, there have been attempts to model the problem using linear elasticity (both isotropic [109, 110] and anisotropic [24]) and GE [71]. Serero et al. [109] find that the effect of a finite system size is primarily that it narrows the stress response (figure 5.9). The bottom boundary condition has a significant effect on the peak; in both cases, the z displacement, U_z, is zero, but a "smooth" bottom ($\sigma_{rz} = 0$) produces a sharper peak than a "rough" bottom ($U_r = 0$). Curiously, Bräuer et al. claim that this boundary condition has little effect [71]; their curve for linear elasticity (figure 5.9) is also noticeably lower than both cases given by Serero et al. [109]. They find a response function for GE that is qualitatively similar, and narrower than the ILE and Boussinesq-Cerutti solutions. Of course, with ξ fixed by the yield angle in GE, there are no parameters to adjust that would affect the shape or height of the peak. It is not clear then how GE might account for variations of the type observed experimentally, as seen in figure 5.8. Then again, Serero et al. find that the response function is not strongly influenced by the value of Poisson's ratio (see inset, figure 5.9), except for thermodynamically inadmissible values greater than 1/2. Thus, isotropic linear elasticity was considered ill-suited to describe granular media, though qualitatively the behavior is indeed elliptic.

Following the problem description given by Bräuer et al., Abaqus results have been obtained for the response function of the ILE, GE, EP, and HAR models. A small piston of diameter $D = 1.456$ cm applies a pressure $P_1 = 500$ Pa at the surface of a granular disc of height h =8 cm. The radius of the disc R need only be large enough that the presence of the side walls does not significantly influence the response function at h =8 cm; $R = 16$ cm is found to be sufficient, and the walls are considered rigid and smooth. In reality,

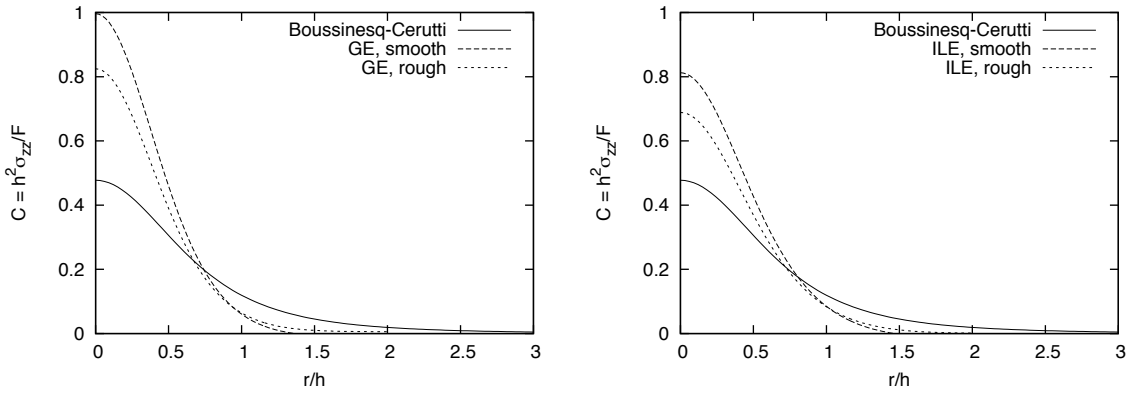

Figure 5.10. Abaqus calculations of the response function for GE (left) and ILE (right). The presence of boundaries increases the peak height, and a frictionless bottom surface results in a higher peak than a rough surface (glued grains).

the surface of the layer outside the piston is a free surface; but as before, this is problematic in the present hyperelastic models, where zero pressure boundaries cannot be handled numerically. A surface force $P_0 = 150$ Pa is applied to avoid these issues, and the stress normalized accordingly:

$$C \equiv \frac{4h^2}{P_1 \pi D^2} \left(\sigma_{zz} - P_0 - \rho g h\right) \tag{5.21}$$

Results for GE and ILE are shown in figure 5.10. The ILE results are in quantitative agreement with those of Serero et al. [109], the curve narrowing due to finite system size and significantly more so for the smooth boundary condition. The same effects are evident in the GE calculation, in contrast with the claims of Bräuer et al. [71]. Both the GE and ILE peaks are higher than their published values.

As the rough bottom boundary more accurately reflects the experiment conditions, this condition is employed in the EP and HAR calculations. Even so, both the EP and HAR models give peak heights significantly higher than predicted by GE and ILE, and observed in experiments. The HAR model gives more reasonable results for increasing values of α, though recall it was *smaller* values of α that gave more physical results for the elastic moduli. The EP model dramatically overestimates the peak height, by about an order of magnitude compared with the dense packing of figure 5.8. Just as the ILE response proved insensitive to the value of ν, the EP response function varies little over the entire range of allowable values for β. Recall that $\beta = 0$ is a thermodynamic limit for the EP model and corresponds to $\nu_{iso} = 1/2$, while $\beta > 8$ implies $\nu_{iso} < 0$, which while theoretically admissible is not expected here.

So, of the hyperelastic models considered here, the EP model, which seemed to best capture the type of stress-induced anisotropy observed in experiments, gives the least accurate response function by a wide margin. As the shape is relatively insensitive to the only adjustable constant β, there is no obvious way to resolve the discrepancy. The similar inability of isotropic linear elasticity to account for the range of observed data has prompted suggestions that fabric anisotropy be included in an anisotropic, linear elastic

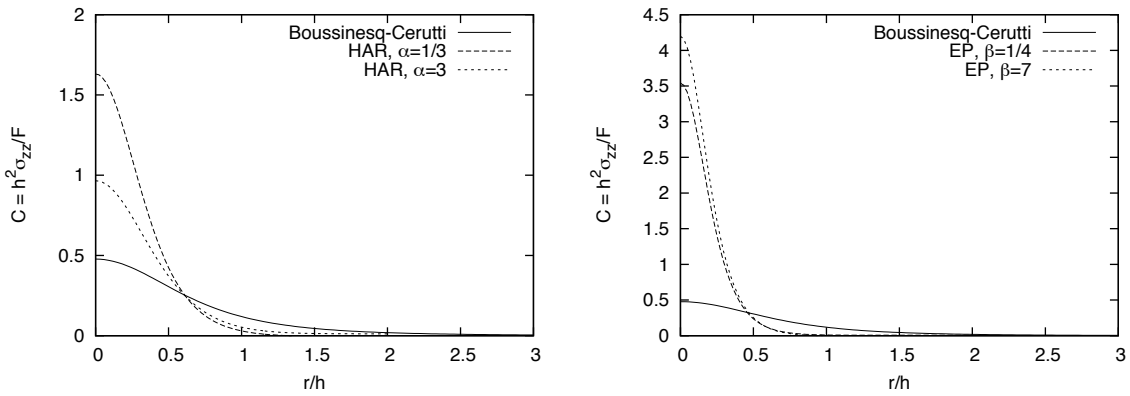

Figure 5.11. Abaqus calculations of the response function for the HAR (left) and EP (right) models. The EP model predicts a much narrower response function than is observed, and is not particularly sensitive to the value of β.

(ALE) model [24, 108, 109]. The simplest case would be a material possessing two Young's moduli, two Poisson's ratios, and a shear modulus. A similar "fabric" anisotropy could easily be incorporated into any of the hyperelastic models presented here. But the caution of Serero et al. applies equally well here: taking five constants as fit parameters will almost certainly produce a good match to the experiment data. Without any reason to prescribe this sort of inherent anisotropy, there is probably little insight to be gained with such a model.

6 Summary and Conclusions

Several recently proposed hyperelastic models for granular materials have been investigated and compared with experiment data. The hyperelastic formalism begins with a scalar free energy function, which ensures energy conservation and path independence, unlike many "elastic" and "hypoelastic" models for granular statics. It is also relatively simple; the entire constitutive behavior of the material is given by the free energy, which gives analytical forms for the stress-strain relation and stiffness matrix by simple differentiation.

As even the quasi-elastic regime of granular materials is non-linear, the hyperelastic forms considered here are all designed to capture the widely observed dependence of the elastic moduli on the square root of pressure. The three models considered are the "granular elasticity" (GE) theory of Jiang and Liu [25, 63, 68–72], with the Helmholtz free energy given by

$$\mathcal{F} = \tilde{G}\Delta^a \left(\frac{2}{5}\xi\Delta^2 + u_s^2 \right) \tag{6.1}$$

a similar form based on the Gibbs free energy due to Einav and Puzrin (EP) [73],

$$\mathcal{G} = \sqrt{\frac{P^3}{B}} \left(\beta + \frac{\sigma_s^2}{P^2} \right) \tag{6.2}$$

and the model of Houlsby, Amorosi, and Rojas (HAR) [67, 76], which has closed forms of both the Helmholtz and Gibbs free energy:

$$\mathcal{F} = A \left(\alpha\Delta^2 + u_s^2 \right)^{\frac{3}{2}} \tag{6.3}$$

$$\mathcal{G} = \frac{2}{3\sqrt{3A}} \left(\frac{1}{\alpha}P^2 + \sigma_s^2 \right)^{\frac{3}{4}} \tag{6.4}$$

An immediate consequence of incorporating the non-linearity into the free energy is that all these forms possess a shear-volumetric coupling due to $P\sigma_s$ or Δu_s terms. This leads to shear dilatancy, the well known characteristic of granular materials, which undergo volumetric expansion when sheared.

A "feature" unique to GE is the fact that $\mathcal{F}$ is not convex everywhere. In fact, the convex region is enclosed by a conical surface that is the well known Drucker-Prager variant of the Coulomb yield condition. This turns out to have some rather unphysical implications for the angle of repose. Considering an infinite granular layer, the thermodynamic yield condition gives an expression for the yield angle in terms of only the material constant ξ. The curve has a maximum; taking $a = 1/2$ to reflect "Hertz contacts" gives $\phi_{max} \approx 25.5°$, implying that no material possesses a higher yield angle, regardless of its value of ξ. This is, of course, significantly lower than typical values of 30°-40°. Perhaps a more logical choice is $a = 1$, as a large body of experimental evidence finds this relationship, in contrast with the Hertz theory. Making this change to GE compounds the aforementioned difficulty with the yield angle, resulting in $\phi_{max} \approx 17°$. Two generalizations proposed by Jiang and Liu similarly fail to resolve this issue. In particular, incorporating a dependence on the third invariant of the strain tensor results in still lower maximum yield angles.

Thus, the yield condition supplied by GE in the form of a thermodynamic stability requirement, while an intuitive description of what amounts to a phase transition, proves to be something of an over-constraint. Independently (and apparently unaware) of Jiang and Liu, Einav and Puzrin (EP) and Houlsby, Amorosi, and Rojas (HAR) proposed a similar hyperelastic formalism, though preferring models based on the Gibbs free energy. This is certainly easier to work with in some situations, as experiment data on granular elastic moduli invariably describe them as functions of the stresses. Thus, the Gibbs free energy gives analytical forms for the elastic moduli as functions of the stresses, making for a simple and direct comparison. While they do not consider convexity explicitly, both forms are found here to be uniformly convex. The EP model, however, has a limiting value of σ_s/P beyond which there are no solutions. Curiously, Houlsby et al. cite this as a drawback of the EP model in motivating their own work, though such a limit is essentially the defining characteristic of granular materials. The present work indicates that the limit places no similar restrictions on the yield angle as in GE, and thus it is not likely that any realizable stress states are off limits in the EP model.

While all three models are designed to have a power law dependence of the elastic moduli on the mean normal stress, they are found in experiments to have a more specific dependence on the individual components of stress. In particular, in the triaxial geometry, Young's modulus in a given direction is found to be a power law function of the normal stress in that direction, and independent of the other normal stresses; i.e.

$$E_v = C\sqrt{\sigma_v} \neq f(\sigma_h) \tag{6.5}$$

While the analytical forms for the Young's moduli are not explicitly independent of the out-of-plane normal stresses for any of these hyperelastic models, the EP model approximates this behavior; E_v varies little with σ_h, and vice versa. It similarly seems to best match the forms of the ratio E_v/E_h, and the Poisson's ratios.

We might expect, then, that the EP model would best match experimental data for stress distributions as well. But this is not the case! Several simple configurations have emerged as benchmarks for models of granular mechanics, and all three hyperelastic models have been implemented in the finite element code Abaqus for comparison with these experiments.

The first problem of interest is the stress distribution under a granular pile. This is known to be dependent on the method of preparation; piles poured from a point source (e.g. a funnel) may possess a dip at the center, a counter-intuitive result. Rain-like pouring from a sieve, on the other hand, produces a center peak as expected. All three hyperelastic models predict a center peak, with a value higher than observed experimentally, even for sieved piles. The peak value and shape of the curve are insensitive to the values of the elastic constants.

The silo is of obvious industrial importance, and a simple model for calculating stresses therein due to Janssen has been employed for over a century. The hyperelastic models match the Janssen behavior, with the vertical stress saturating with depth due to wall friction. But linear elasticity predicts this as well, so this

is perhaps not a noteworthy success of these models. If a pressure equal to the saturated value is added to the surface of the silo, the Janssen model gives $\sigma_{zz}/\sigma_{sat} = 1$ everywhere, while a substantial "overshoot" (up to 20%) of the saturated stress is observed in experiments. Linear elasticity predicts a very small overshoot, less than 1%. All three hyperelastic models give an overshoot of around 2%, closer to the linear elastic case than reality.

An experiment to determine the "response function" of a granular layer to a point force perturbation was proposed to settle the issue of whether hyperbolic or elliptic systems governed granular statics. The experiments clearly support the elliptic (elastic) model for sufficiently large and disordered systems. But the response function varied significantly based on the layer construction, and was found to be much broader for more densely packed layers. The finiteness of the layer introduces some dependence on the elastic constants, but not enough to account for the difference; this was previously found to be the case for linear elasticity, and the results presented here for all three hyperelastic models are similar. Paradoxically, the EP model, which gives the best analytical forms for the elastic moduli, grossly overestimates the peak in the response function, for the entire range of realistic β.

So, while hyperelastic models seem to be better descriptors of granular statics in some ways, they fail to describe some simple experiments in the same fashion as isotropic linear elasticity. It is clear that the static behavior of granular materials depends strongly on the preparation of the material, and this is not explicitly accounted for in the hyperelastic models. Of course, accounting for this preparation dependence is the idea behind stress-only models such as FPA and the Janssen model, which impose a relationship between stress components presumed to be "frozen in" at preparation. But these do not extend naturally beyond the simple configurations they were designed for, and completely ignoring deformations seems an oversimplification in many cases. In addition, the qualitative features of the response function strongly support the elastic picture. Rather, we might expect to find these relationships as special cases of a more general theory. Still, this theory must account in some way for the preparation dependence. Here are a few ways this might be accomplished:

- Explicitly considering density variations. A non-uniform density has been proposed as an explanation for the stress dip in sand piles. This is plausible, but not verified experimentally. It would be difficult to do so, and perhaps equally difficult to account for theoretically. A "frozen in" density distribution might explain some observed behavior, but the distribution would not, in general, be known for complex problems. More complicated still would be density changes due to applied stresses. These must be accounted for in the free energy, but are assumed to be small and safely ignorable. It is not clear whether significant density changes could occur within the quasi-elastic regime. Plastic deformations may obviously be significant; it is not clear how much plastic rearrangement is occurring in the experiments.

- Fabric anisotropy. This is not included in any of the hyperelastic models, but could certainly be introduced through a "fabric tensor" of elastic constants. This is best applied with caution; as noted

previously, ad hoc addition of additional "fit parameters" will certainly allow for good fits to experiment data. There should be some justification for assumptions made about the fabric, but this is a challenging problem. For example, in the triaxial tests, in which the specimens are probably prepared in a similar fashion, the "inherent" stiffness does not consistently favor the horizontal or vertical direction.

- Incorporating dependence on the third tensor invariant. This does not necessarily have anything to do with preparation, and of course proved to be an unsuccessful generalization of GE. But recall that experimentally, the shear modulus is independent of one of the normal stresses, while the hyperelastic models possess no such anisotropy in the shear modulus. It appears that this is always the case for two-invariant hyperelastic models. It is not clear why the third invariant ought to be included in such a model, or what its physical significance is, but this a point for further investigation.

Aside from these physics issues, the coupling of elastic, plastic, and flow models (e.g. for the dust pile mobilization problem) is still unresolved, though some discussion is presented in the appendices. Note also that this is the subject of a recent dissertation by Kamrin [65], who coupled a plasticity model with GE. However, the results presented here indicate that the more sophisticated hyperelastic models possess the same failings as isotropic linear elastiticy, and the latter seems to give comparable or better results for the stress distribution in some simple configurations. So, despite its known shortcomings, ILE seems an appropriate choice for engineering models at present, in light of the relative simplicity it affords.

Finally, some comments are in order regarding the proposed coupling for mobilization problems. The problem is initially one of solid-fluid interaction; the static stress distribution in a granular pile or layer may be obtained from linear elasticity. At the initiation of a fluid flow in the vicinity of the pile (or some more general change in forces), the pile will now be stressed in a different manner due to pressure and shear from the flow. These boundary conditions result in a new static stress distribution, which may or may not reach the yield surface. In regions where it does, a transition from static to flowing behavior will occur. It is expected that the type of yield surface employed will strongly influence predicted mobilization; some examples are given in appendix A.2, though this is not intended to be a comprehensive treatment, and it is still not known if more complex surfaces will gives better results than a Coulomb yield condition. It should also be noted that as particles decrease in size, other interactions become important, in particular cohesive forces; some models for cohesive interactions are presented in appendix G. For micron sized particles (particularly graphite) of interest in nuclear systems, electrostatic forces will also be important. It is unclear whether these effects can be appropriately captured by a constant offset to the Coulomb condition 2.1, or whether some more sophisticated modeling is necessary.

A Appendix: Granular Flow

A.1 Preliminaries

We return now to the problem of "dust mobilization". This problem has been considered in previous fusion safety analyses [113, 114]. Takase performed CFD calculations with discrete particle tracking; the particles were subject to drag and buoyancy forces. This method gives some indication of how particles are transported in flows, but it cannot really predict mobilization, as there is no mechanism for particles to interact with each other, or stick to surfaces. It also does not directly give the aerosol concentration, which is obviously of interest for safety analyses. These can both be accounted for more naturally in the continuum approach adopted here.

In the continuum picture, the granular material is static until its stress state reaches the yield surface, at which point it begins to flow; it continues to deform under constant stress. In conventional solids this is plastic deformation, and the same terminology is sometimes employed in describing dense granular flows. While elastic and plastic deformation would be treated concurrently in the conventional solid problem, and some approaches to granular materials such as Hypoplasticity [80] and Granular Solid Hydrodynamics [82, 115] aim to do this, it is expected that the transition will be rather abrupt in the mobilization problem. Here the dust piles are not confined and under heavy loads as would often be the case in soil mechanics. They will deform elastically up to a point (yield), but beyond yield will possess kinetic, not elastic, energy. Thus in this case yield is identified as the threshold for mobilization, and constitutive models for granular flows are employed once the material yields.

Neglecting any "viscoelastic" region, the flowing granular material may be described by the Navier-Stokes equations,

$$\frac{D\underline{v}}{Dt} = -\frac{1}{\rho}\nabla p + \frac{1}{\rho}\nabla \cdot \underline{\underline{\mathbf{T}}} + \underline{A} \tag{A.1}$$

with a non-Newtonian constitutive equation chosen to describe the relevant flow regime. Here v is the particle velocity, ρ is the bulk particle density, p the particle phase pressure, $\mathbf{T}$ is the deviatoric stress tensor, and A the acceleration due to body forces. The four terms are due to inertial, pressure, "viscous", and body forces, respectively. A constitutive relation is required to relate the deviatoric stress tensor $\mathbf{T}$ to the velocity and close the system. The form of this relation will differ depending on the granular flow regime; these may be broadly divided into plastic/frictional and viscous/collisional (Figure A.1). Frictional flows are characterized by enduring contacts between particles in which friction is the dominant momentum transfer mechanism; this is the type of slow, dense particle flow that would immediately follow yield. If the particle volume fraction decreases such that these enduring contacts are lost, momentum transfer is due to particle collisions and the constitutive equation is determined from kinetic theory. If the particles are separated to the point that even collisional contributions are small, $\mathbf{T}$ may be neglected altogether. It is in this limit that traditional aerosol and particle tracking methods apply. The relationship between these methods is clarified in section A.5.

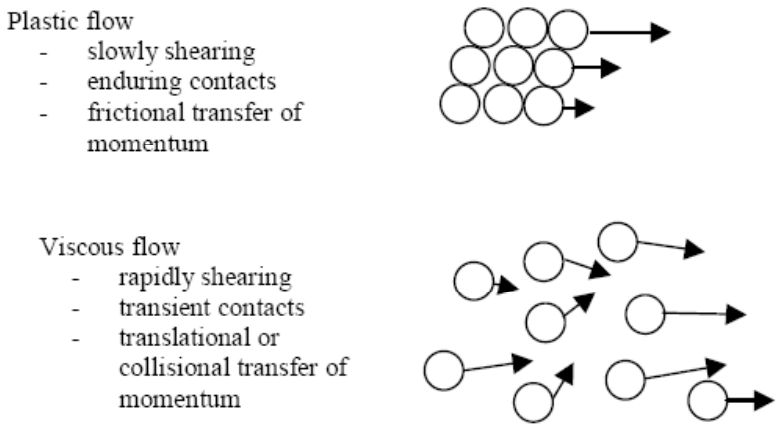

Figure A.1. Comparison of viscous granular flow regimes, from [116].

A.2 Frictional Regime

Constitutive equations for frictional granular flow are typically of the form derived by Schaeffer [117] and are frequently employed in describing flow from silos or hoppers [118, 119]. Two assumptions are made: 1) the stresses are related via the Coulomb yield condition (equation 2.9), and 2) the flow is associated, i.e. the axes of principal stress and strain rate are aligned. In principal stress space (2D), the Coulomb criterion is

$$\frac{\sigma_1}{\sigma_2} = \frac{1+\sin\phi}{1-\sin\phi} \tag{A.2}$$

which forms a wedge in principal stress space in which static solutions lie. Schaeffer extends this to a cone in three dimensions; a von Mises yield condition (Figure A.2), defined by

$$\sum_{i=1}^{3} (\sigma_i - \sigma)^2 \leq 2\sigma^2 \sin^2\phi \tag{A.3}$$

with

$$\sigma = \frac{\sigma_1 + \sigma_2 + \sigma_3}{3} \tag{A.4}$$

Recognizing $\sigma_i - \sigma$ as the deviator of the stress tensor, σ as the granular pressure P, and noting that the equality holds at yield, this can be rewritten as

$$\sqrt{\mathbf{T}:\mathbf{T}} = \sqrt{2}P\sin\phi \tag{A.5}$$

where $\mathbf{T}:\mathbf{T}$ denotes the tensor scalar product (second invariant). The flow rule requires that the principal stresses and strain rates are coaxial:

$$\mathbf{S} = q\mathbf{T} \tag{A.6}$$

where q is a scalar constant and $\mathbf{S}$ is the deviatoric strain rate tensor,

$$\mathbf{S} = \frac{1}{2}\left(\nabla\underline{v} + (\nabla\underline{v})^T\right) - \frac{1}{3}(\nabla\cdot\underline{v})\,\mathbf{I} \tag{A.7}$$

Combining both the yield condition (equation A.5) and the flow rule (equation A.6),

$$\frac{\sqrt{\mathbf{S}:\mathbf{S}}}{q} = \sqrt{\mathbf{T}:\mathbf{T}} \tag{A.8}$$

and

$$q = \frac{\sqrt{\mathbf{S}:\mathbf{S}}}{\sqrt{2}P\sin\phi} \tag{A.9}$$

and the resulting constitutive equation is

$$\mathbf{T} = \frac{\sqrt{2}P\sin\phi}{\sqrt{\mathbf{S}:\mathbf{S}}}\mathbf{S} \tag{A.10}$$

It exhibits a zero-order dependence of stress on the strain rate; i.e., scaling the velocities does not change the stress state. This is an observed behavior of dense granular flows [120]. Note that the flow rule (equation A.6) also implies incompressibility, since

$$\nabla\cdot\underline{v} = Tr(\mathbf{S}) = qTr(\mathbf{T}) \tag{A.11}$$

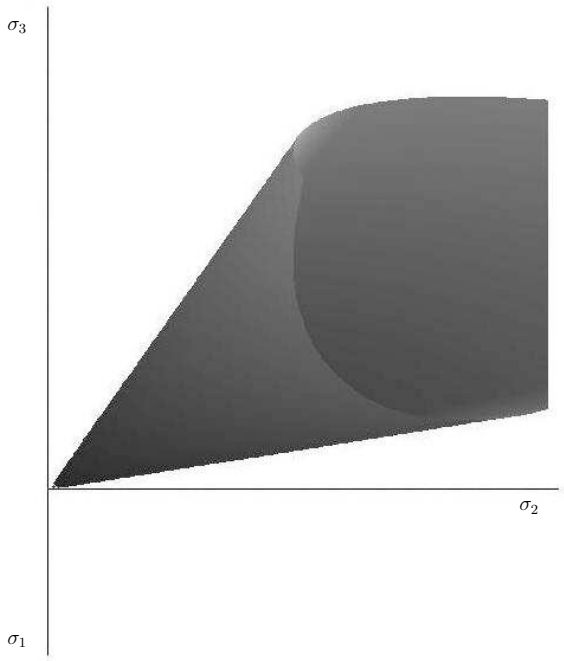

Figure A.2. The von Mises yield cone, or Drucker-Prager yield surface, an extension of the Coulomb condition (equation 2.9) to three dimensions.

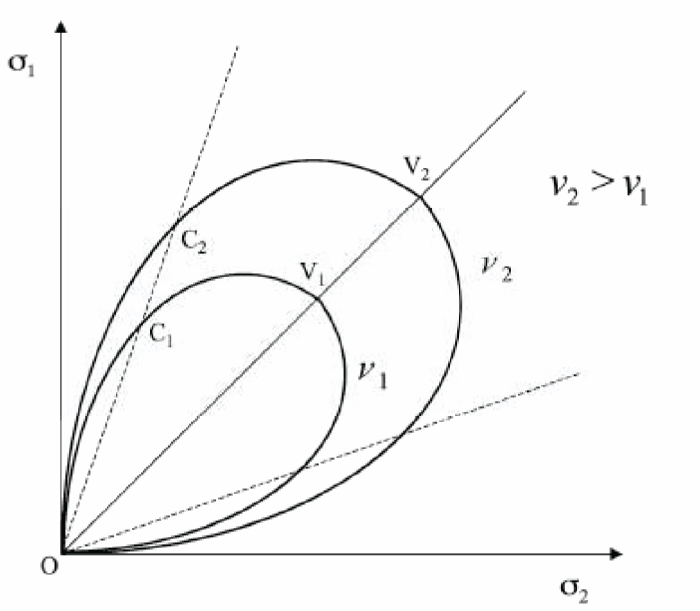

Figure A.3. Yield loci at two different volume fractions ν_1 and ν_2 in principal stress space (reprinted from [118] with permission from Elsevier). Dilation occurs on segments OC_i, while compaction occurs on segments C_iV_i. The dotted lines define the critical state.

and $\mathbf{T}$ is the traceless part of the stress tensor.

There are some practical and physical problems, however, with this approach. Schaeffer [117], following the derivation, showed that in 2D the equations were ill-posed (similar to the backwards heat equation), but that this was not the case in fully three-dimensional flows [121] and that compressibility served to damp the instabilities [122]. The assumption of a von Mises type (conical) yield surface also results in zero dissipation, an un-physical result considering that momentum transfer is dominated by friction. This motivated the development of more sophisticated models which include compressibility and alter the yield surface such that it is convex, ensuring that dissipation is positive and resulting in a yield locus of the type pictured in figure A.3 [118, 120, 122–128]. This type of model better describes the behavior of real granular materials, which, when sheared, dilate at low compression but compact at high compression (figure A.4). At the transition between these two behaviors, deformation occurs at constant volume, and this point is referred to as the critical state [126].

Compressibility allows for a varying bulk density, in which case another equation is required to close the system. For frictional granular flows this is invariably an empirical relationship between the pressure and bulk density, or equivalently, the solid volume fraction. One model originally due to Johnson and Jackson [129] assumes divergence of the pressure at a maximum packing, taken to be "random close packing" [130], which for spheres is $\sim$0.64. This was extended [118] to include a minimum packing fraction below which

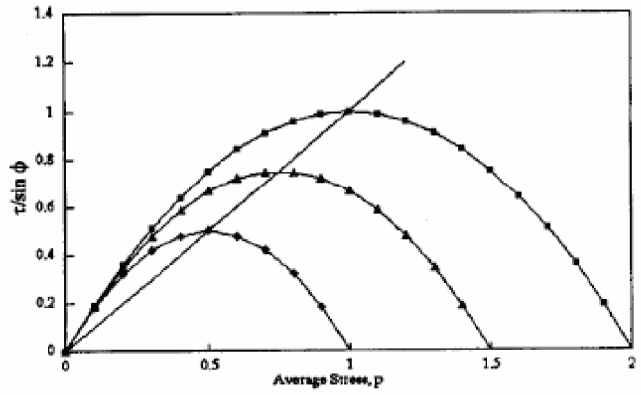

Figure A.4. Generalized yield conditions (reprinted from [128] with permission from Elsevier). At the critical state, $\partial\tau/\partial\sigma = 0$. At lower pressures, the material dilates; at higher pressures, it compacts.

frictional effects are assumed to be unimportant:

$$P = F\frac{(\nu - \nu_{min})^r}{(\nu_{max} - \nu)^s} \tag{A.12}$$

with constants F, r, and s equal to 0.05, 2, and 5, respectively, and $\nu_{min} = 0.5$.

A.3 Modeling

Some comments are in order regarding the transition from static to dynamic behavior, and how it might be modeled. The computational fluid dynamics code Fluent appears capable of handling many of the granular flow regimes discussed previously, and a general solution procedure will be outlined here.

The first step in the solution procedure is determining the stress distribution in the dust pile, e.g. via finite element calculations employing the models described here. Regardless of the method ultimately employed in this calculation, a means of coupling it to the flow calculation will need to be developed. Initially, Fluent may be used to calculate the shear on the surface of the dust pile, which in this case would be defined as a wall. This would be input as a boundary condition in the static problem. If yield is not reached, then the analysis is complete and zero mobilization is predicted. If yield does occur, a transition to the flow problem will have to be made. Ideally, and in keeping with observed behavior discussed in section B.2, this would occur only in the yielding portion of the pile, e.g. on a cell by cell basis. The solid/fluid boundary would change in this case, and yielding solid cells would become fluid cells, with the remainder of the pile stable. The feasibility of implementing such a scheme will need to be determined.

Aside from the possible difficulties of implementation, there is some ambiguity in the physics of this transition as well. It is apparent that equation A.10 diverges when the velocity derivatives (i.e. shear rates) are zero, but this is precisely the condition of the material until the point that it yields. Schaeffer [117] mentions explicitly in the derivation of the equations that they apply to materials that *are deforming* and *were previously* deforming. This is an issue in any granular flow problem which exhibits regions of little or no flow and in practice is avoided by adding a constant in the denominator [118, 119]:

$$\mathbf{T} = \frac{\sqrt{2}P\sin\phi}{\sqrt{\mathbf{S}:\mathbf{S} + \epsilon}}\mathbf{S} \tag{A.13}$$

This avoids divergence but essentially imposes slow flow on regions that would actually be static [118]. In principle such regions would transition back to an elastic description.

Farther from the solid-fluid transition region, equation A.10 should apply. The Schaeffer model for the constitutive equation, with the empirical pressure (equation A.12) attributed to Johnson and Jackson [129], are both available in Fluent. The User Defined Function (UDF) capability allows implementation of any constitutive equation that can be cast as a viscosity:

$$\mathbf{T} = \mu\mathbf{S} \tag{A.14}$$

The viscosity can depend on any of the flow variables, which are accessed via Fluent macros in the user-written C code. In this case the "frictional viscosity" in the Schaeffer model is given by

$$\mu_f = \frac{\sqrt{2}P \sin\phi}{\sqrt{\mathbf{S} : \mathbf{S}}} \tag{A.15}$$

Frictional, collisional, and kinetic models may be used concurrently, in which case their contributions are simply added (the same approach is used elsewhere, see [116, 118, 129]). The contributions from these terms become small as the volume fraction decreases, and transition naturally into the aerosol regime described in section A.5.

All the granular flow models are multi-phase models, and mass, momentum, and energy equations are solved for each phase. They are assumed to be "inter-penetrating continua", coupled by a drag force law (two-way coupling is also possible). A number of drag models are available that are altered to account for high particle volume fraction. These also may be specified via user defined function.

Without a method to calculate yield and connect it to Fluent's granular flow models, there is little to be said at present regarding the accuracy of the various granular flow models in predicting dust transport in mobilization problems. Fluent has been used, however, in modeling the filling of evacuated vessels, as the loss of vacuum accident (LOVA) is of particular interest for dust mobilization. These models are presented alongside experimental and theoretical results in section B.1.

A.4 Kinetic/Collisional regime

Kinetic/collisional closures for the stress tensor are determined by the statistical methods employed in the Chapman-Enskog theory of dense gases [131], adapted to granular materials by a number of researchers [89, 116, 132–134]. These will not be considered in detail here. This regime is typical of fluidized beds and connects the dense frictional regime ($\nu \gtrsim 0.5$) and the dilute non-interacting regime ($\nu \lesssim 0.1$).

A.5 Aerosols and Lagrangian particle tracking

As the particle volume fraction continues to decrease, interactions between particles become insignificant altogether. Then, the viscous terms in the Navier-Stokes equations (A.1) may be neglected:

$$\frac{D\underline{v}}{Dt} = -\frac{1}{\rho}\nabla p + \underline{A} \tag{A.16}$$

Furthermore, as an ensemble of non-interacting particles, the ideal gas law applies; so the pressure term may be rewritten as follows:

$$\frac{D\underline{v}}{Dt} = -\frac{1}{\rho}\nabla nkT + \underline{A} \tag{A.17}$$

Identifying the bulk density as the particle concentration n times the individual particle mass m, and assuming constant temperature,

$$\frac{D\underline{v}}{Dt} = -\frac{kT}{m}\frac{\nabla n}{n} + \underline{A} \tag{A.18}$$

The particles are now dispersed and suspended in a gas, and will experience a body force due to drag. Adding the restriction of low Stokes numbers, where

$$Stk = \frac{\tau U}{L} \tag{A.19}$$

and U and L are the characteristic velocity and length scale of the flow, and τ is the spherical particle relaxation time given by

$$\tau = \frac{\rho_s d^2}{24\mu} \tag{A.20}$$

for fluid viscosity μ, particle diameter d, and solid material density ρ_s. As a ratio of inertial to viscous (drag) forces, low Stokes numbers imply negligible inertia, and the inertial terms in equation A.16 can be discarded accordingly. The drag force is given by Stokes' law, and

$$\underline{A} = \frac{\underline{u} - \underline{v}}{\tau} \tag{A.21}$$

for the particle velocity v relative to the fluid velocity u. The momentum equation simplifies to

$$\frac{\tau kT}{m}\nabla n = n(\underline{u} - \underline{v}) \tag{A.22}$$

Here the particle velocity v can be solved for explicitly. Recognizing the Einstein diffusion coefficient D [135],

$$D = \frac{\tau kT}{m} \tag{A.23}$$

the particle flux is given by

$$n\underline{v} = n\underline{u} - D\nabla n \tag{A.24}$$

Using this expression in the continuity equation,

$$\frac{\partial n}{\partial t} + \nabla \cdot (n\underline{v}) = 0 \tag{A.25}$$

the result is the 'aerosol dynamic equation' as used in aerosol transport phenomena [136]:

$$\frac{\partial n}{\partial t} + \mathbf{v} \cdot \nabla n = D\nabla^2 n \tag{A.26}$$

Thus the aerosol dynamic equation is a special case of a general particle fluid described by the Navier-Stokes equations, in which particle interactions and particle inertia are neglected.

If one neglects diffusion (pressure) rather than inertia (i.e. only inertia and drag force terms are retained), the resulting system is hyperbolic, and its characteristics are the Lagrangian equations of motion [137]. Thus, aerosol dynamics and Lagrangian particle tracking treat two opposite dilute flow regimes: purely diffusive and purely inertial, respectively. Any problem in which both effects may be important (but particles are still non-interacting) should solve the general case that accounts for both (equation A.16).

The problem of dust transport in a loss of vacuum accident cannot be simplified to either of the two cases above *a priori*. Here flow conditions will vary widely in both space and time. The particle relaxation time varies as the particle diameter squared, and this diameter may span several orders of magnitude. Furthermore, local velocity gradients (U/L) will be high in regions near the breach, but lower elsewhere, and will everywhere decrease in time as the vessel fills with air. Rather than selecting a model that may restrict the ability to consider certain particle sizes, materials, and flow regimes, one can treat the general case.

B Appendix: Dust Mobilization Experiments

B.1 The Toroidal Dust Mobilization Experiment

The Toroidal Dust Mobilization eXperiment (TDMX) was developed to investigate the mobilization of dust in fusion-relevant scenarios: Loss of Vacuum Accidents (LOVAs) in a toroidal geometry, using dust characteristic of that produced in tokamaks. TDMX consists of two acrylic cylinders of 15.24 cm (6 in) and 30.48 cm (12 in) diameter, 60.96 cm (24 in) in height (Figure B.1), reproducing the major and minor radii of ITER in approximately 1/50 scale. Numerous diagnostic ports are available on the end caps of the cylinder. Venting occurs through one of two available inlets; a 5.08 cm (2 in) diameter, 50.8 cm (20 in) long tube extending axially from the top of the annular region, or through a 8.26 cm (3.25 in) diameter tube extending radially from the axial midpoint of the outer cylinder. The bottom and top end caps are interchangeable, allowing venting from the top or bottom of the vessel. The end caps can be oriented at an arbitrary angle to the outer cylinder and radial vent; in the experiments and models described below, they are 180° apart, and venting occurs through the axial inlet. Vacuum (to approximately 130 Pa) is held at the inlet by a disk which slides free of the opening to allow unobstructed flow through the inlet. The flow rate is limited as desired for each test by an orifice plate, located at the interface of the inlet tube and annular vessel. The pressurization rate is measured at the top of the chamber with a capacitance manometer.

B.1.1 Pressurization rate

An analytical solution for vessel pressure as a function of time can be obtained under some simplifying assumptions [138, 139]. It is assumed that the gas (air) is ideal with constant specific heat, that the air in the vessel is at rest with spatially uniform thermodynamic properties, and that flow through the inlet is 1-D and isentropic. The cross sectional area of the inlet is constant, and the contents of the vessel are in thermal equilibrium with the surroundings. From here one assumes that the process is either adiabatic or isothermal. Typical vessel filling problems are better approximated by an isothermal solution; for transients on the order of one second or longer [139], high velocities inside the vessel rapidly transfer heat to the walls, resulting in little temperature increase in the gas (note the apparent contradiction with the initial assumption of zero velocity). Flow in TDMX is initially choked since the pressure is well below the critical value, given by

$$P_{r,c} = \left(\frac{2}{\gamma+1}\right)^{\gamma/(\gamma-1)} \tag{B.1}$$

Here the subscript r denotes a "reduced" quantity, normalized with respect to the pressure of the surroundings. The specific heat ratio, γ, is equal to 1.4 for air. Time, t, is normalized with respect to a characteristic time, t_{char}, which is given in terms of the vessel volume V, inlet cross sectional area A, and sound speed (based on the temperature of the surroundings) c:

$$t_{char} = \frac{V}{Ac} \tag{B.2}$$

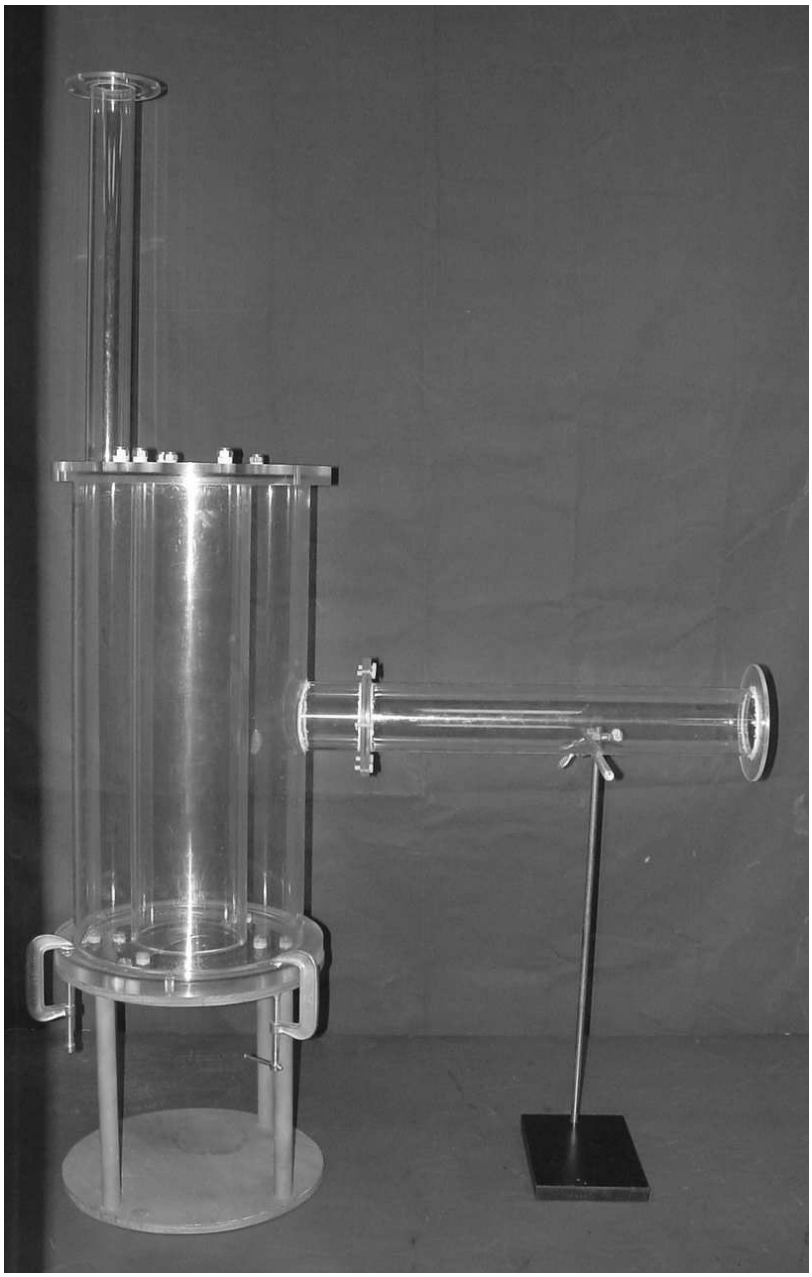

Figure B.1. The Toroidal Dust Mobilization Experiment (TDMX).

The pressurization rate is linear while flow is choked. For isothermal (superscript I) and adiabatic (superscript A) solutions, respectively,

$$P_r^I(t_r) = P_{r,i} + \left(\frac{2}{\gamma+1}\right)^{\frac{\gamma+1}{2(\gamma-1)}} t_r \tag{B.3}$$

$$P_r^A(t_r) = P_{r,i} + \gamma\left(\frac{2}{\gamma+1}\right)^{\frac{\gamma+1}{2(\gamma-1)}} t_r \tag{B.4}$$

where $P_{r,i}$ is the initial reduced pressure in the vessel. Now the time to reach critical pressure, $t_{r,c}$ can be determined:

$$t_{r,c}^I = \left(\frac{2}{\gamma+1}\right)^{1/2} - P_{r,i}\left(\frac{2}{\gamma+1}\right)^{\frac{\gamma+1}{2(1-\gamma)}} \tag{B.5}$$

$$t_{r,c}^A = \frac{1}{\gamma}\left(\frac{2}{\gamma+1}\right)^{1/2} - \frac{P_{r,i}}{\gamma}\left(\frac{2}{\gamma+1}\right)^{\frac{\gamma+1}{2(1-\gamma)}} \tag{B.6}$$

Above the critical pressure, the pressurization rate decreases until it reaches zero when the vessel pressure reaches that of the surroundings:

$$P_r^I(t_r) = \left[1 - \left[\sqrt{1 - P_{r,c}^{\frac{\gamma-1}{\gamma}}} - \sqrt{\frac{\gamma-1}{2\gamma^2}}\left(t_r - t_{r,c}^I\right)\right]^2\right]^{\frac{\gamma}{\gamma-1}} \tag{B.7}$$

$$P_r^A(t_r) = \left[1 - \left[\sqrt{1 - P_{r,c}^{\frac{\gamma-1}{\gamma}}} - \sqrt{\frac{\gamma-1}{2}}\left(t_r - t_{r,c}^A\right)\right]^2\right]^{\frac{\gamma}{\gamma-1}} \tag{B.8}$$

and the total vessel filling times ($t_{r,f}$) are

$$t_{r,f}^I = \sqrt{\left(\frac{2\gamma^2}{\gamma-1}\left(1 - P_{r,c}^{\frac{\gamma-1}{\gamma}}\right)\right)} + t_{r,c}^I \tag{B.9}$$

$$t_{r,f}^A = \sqrt{\left(\frac{2}{\gamma-1}\left(1 - P_{r,c}^{\frac{\gamma-1}{\gamma}}\right)\right)} + t_{r,c}^A \tag{B.10}$$

The times to reach critical and atmospheric pressure are evaluated for TDMX parameters, based on a 5.08 cm (2 in) diameter inlet cross section, in Table B.1.

The filling of TDMX has been modeled in Fluent, in which the evacuated vessel is connected to a large volume at atmospheric (85 kPa) pressure. In the experiments, the initial pressure may be as low as 135 Pa; model results presented here were initialized at 1000 Pa to avoid convergence difficulties and accompanying long computation times that sometimes occur in the Fluent solver at very low pressures. Since the experimental pressure transient is affected by heat transfer from the vessel, this effect must be accounted for in the model as well. Therefore, a convection heat transfer coefficient of 8.4 W/m^{2}K is applied to all chamber walls, derived from the following Nusselt number (Nu) correlation for vertical flat plates:

$$\overline{Nu_L} = \left[0.825 + \frac{0.387 Ra_L^{1/6}}{\left[1 + (0.492/Pr)^{9/16}\right]^{8/27}}\right]^2 \tag{B.11}$$

	Isothermal	Adiabatic
P_i (Pa)	135	135
P_f (Pa)	85000	85000
T_i (K)	293	293
T_f (K)	293	410.2
t_{char} (s)	0.0434	0.0434
t_c (s)	0.0395	0.0282
t_f (s)	0.0950	0.0679

Table B.1. TDMX conditions and vessel fill times.

Ra is the Raleigh number and Pr is the Prandtl number. The correlation is valid for cylinders [140] with diameter D and height L satisfying

$$\frac{D}{L} > \frac{35}{Gr_L^{1/4}} \tag{B.12}$$

where Gr is the Grashof number based on the height L.

Analytical, experimental, and model results for TDMX axial vents (d = 2 in) are compared in Figure B.2. The model, with a heat transfer coefficient of 8.4 W/m^{2}K, matches closely the isothermal analytical solution, with a slightly faster fill time. The model predicts one important flow feature from the experiment that the analytical treatment lacks; oscillating flow after the vessel fills. This feature is of particular interest since it could result in the release of dust from the vessel, which would contribute to the source term in an ITER accident scenario. Compared to the experimental data, this case predicts a longer fill time, with flow oscillations smaller in magnitude, though similar in period. To determine the effect of the applied heat transfer coefficient on the model transient, two similar cases were run; one adiabatic, and the other with a heat transfer coefficient of 4.2 W/m^{2}K, half of the original value. The pressure transients for both these cases were nearly identical; the adiabatic case appears in Figure B.2. This resulted in faster vessel filling, and also increased the magnitude of flow oscillations.

While these models compare reasonably well with analytical and experimental results, these are very fast transients (∼0.1 s), and complete mobilization is expected in this case. Of greater interest is the transition region where only partial mobilization occurs. For piles of 0.5 μm tungsten dust totaling approximately two grams, this transition regime is shown in Figure B.3. For dust piles directly underneath the vent (0° offset), complete mobilization occurs for vent diameters above 3/16", with little mobilization occurring below 1/16". For piles offset a full 180° toroidally, the range of partial mobilization falls between 1/8" and 5/16" entrance diameters.

Modeling the vessel filling for this range of vent diameters has been less successful due to prohibitively long computation times. The small flow passage requires small cells in this region, which in turn requires

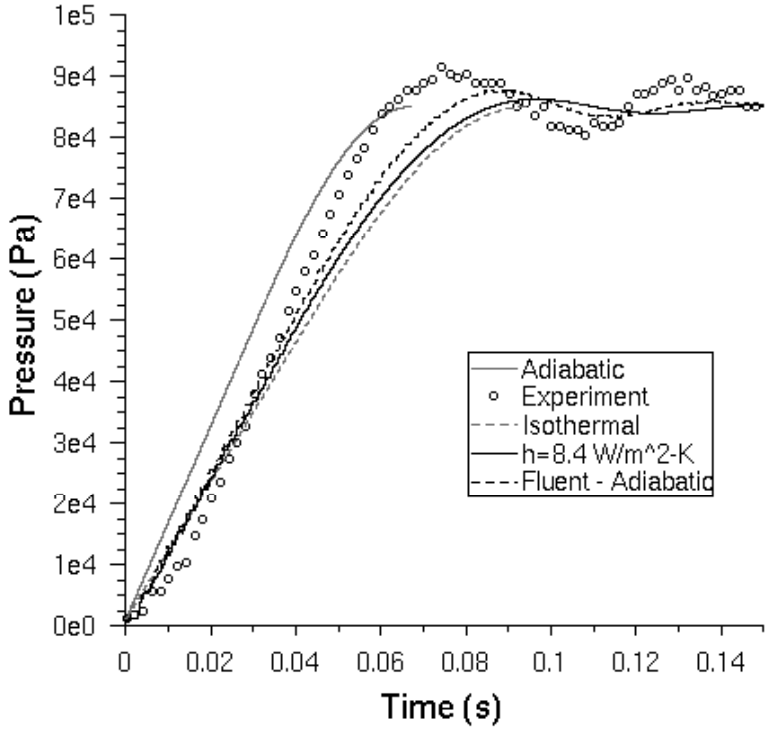

Figure B.2. Comparison of analytical (gray), experimental, and Fluent (black) results.

a small time step; in addition, the fill time for a 1/4 inch diameter vent is more than 50 times longer than for the 2 inch diameter vent described above. Combined, these effects result in extremely long computation times. Addition of multi-phase and granular flow models will not help this situation; high performance computing options will have to be explored if many such models are to be employed.

B.2 Simple pipe mobilization experiment

Given the varied and complex nature of the granular material models that are proposed to model dust mobilization, it was decided that benchmarking such models would be better served by simpler experiments. To that end, a horizontal pipe experiment has been constructed to investigate dust mobilization. It consists of a long acrylic tube, 0.75 inches in diameter, with an approximately ten foot entrance length upstream of a dust pile to establish fully developed flow. Following this entrance length is the test section, where a portion of the tube is cut away and dust may be poured in. The tube extends two feet downstream of the test section and is then exhausted through a HEPA filter. In the present setup, two flow meters in parallel allow for a maximum of 100 standard liters per minute of helium, equivalent to a Reynolds number of about 930. Two materials have been tested thus far; 316 stainless steel of 65 μm diameter (Figure B.4), and graphite of 4 μm diameter (Figure B.5).

The latter is a size and material characteristic of dust sampled from tokamaks [4, 5]. The stainless steel is large for fusion dust, but it is necessary to conduct experiments on cohesionless materials as well, and this implies larger particles. Both were subjected to flows of helium, which were increased in small step changes up to the maximum Reynolds number of 930. The behavior of both materials was similar, and consistent with the "yielding solid" description outlined previously. If the behavior were fluid-like, mobilization would be continual at constant flow rate, with the rate of mobilization increasing with increasing flow rate. Rather, the dust pile is stable at Re$\sim$930, sustaining shear with no observable mobilization as flow continues at that rate. What few changes did occur in the piles were consistent with the idea of yield in a region of the pile; in a few instances, when a small increase in the flow rate was made, a small section of the pile would be mobilized (typically near the top on the leading face), with the rest of the pile remaining unchanged.

These observations suggest that at rest and for relatively low stresses, the behavior of dust piles is in fact solid/elastic; and that mobilization may be identified with yield. But, yield may occur only in small portions of the pile, and mobilization will be partial in this case, with the rest of the pile remaining in a stable configuration.

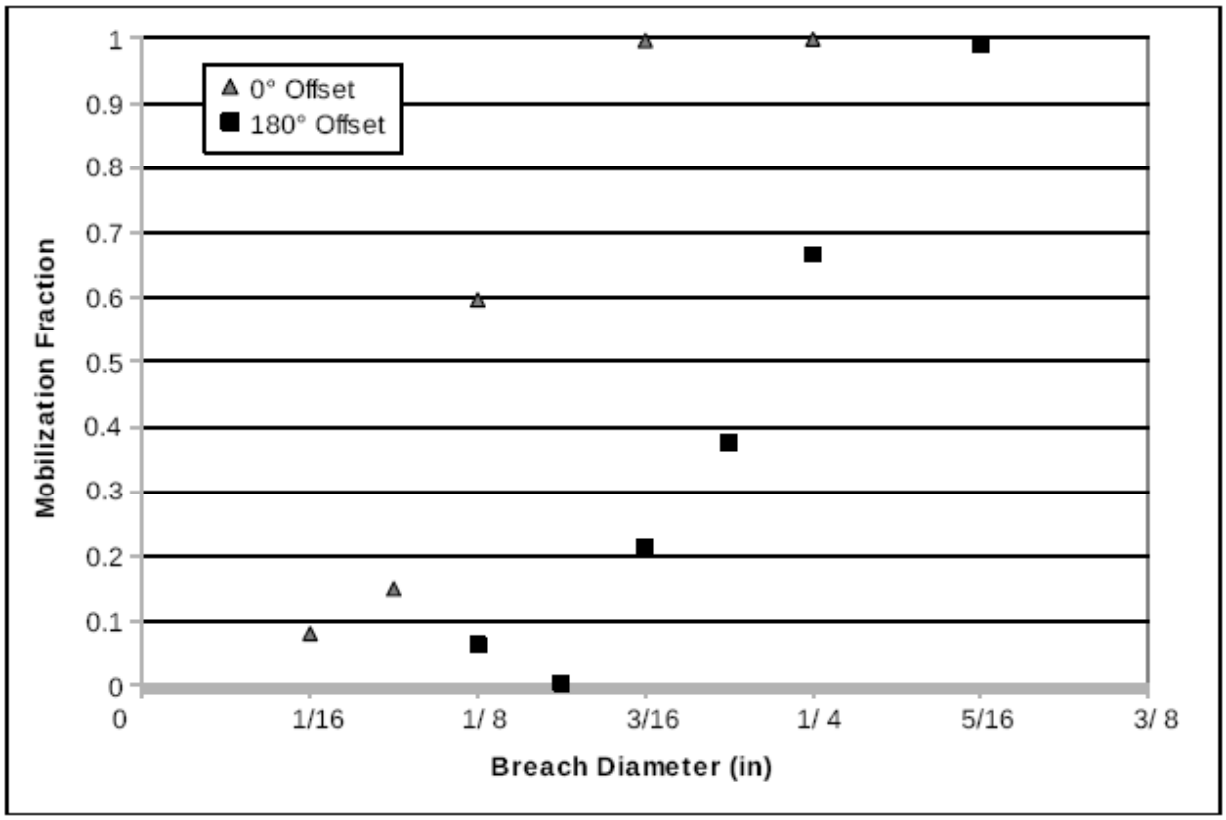

Figure B.3. Mobilized fraction of 2 gram tungsten dust piles directly underneath the vent (0° offset) and offset 180°, for a variety of vent sizes.

Figure B.4. The test section with a pile of 65 μm stainless steel dust following shear by a flow of helium up to Re = 930. There was no observable mobilization, and the pile remained stable.

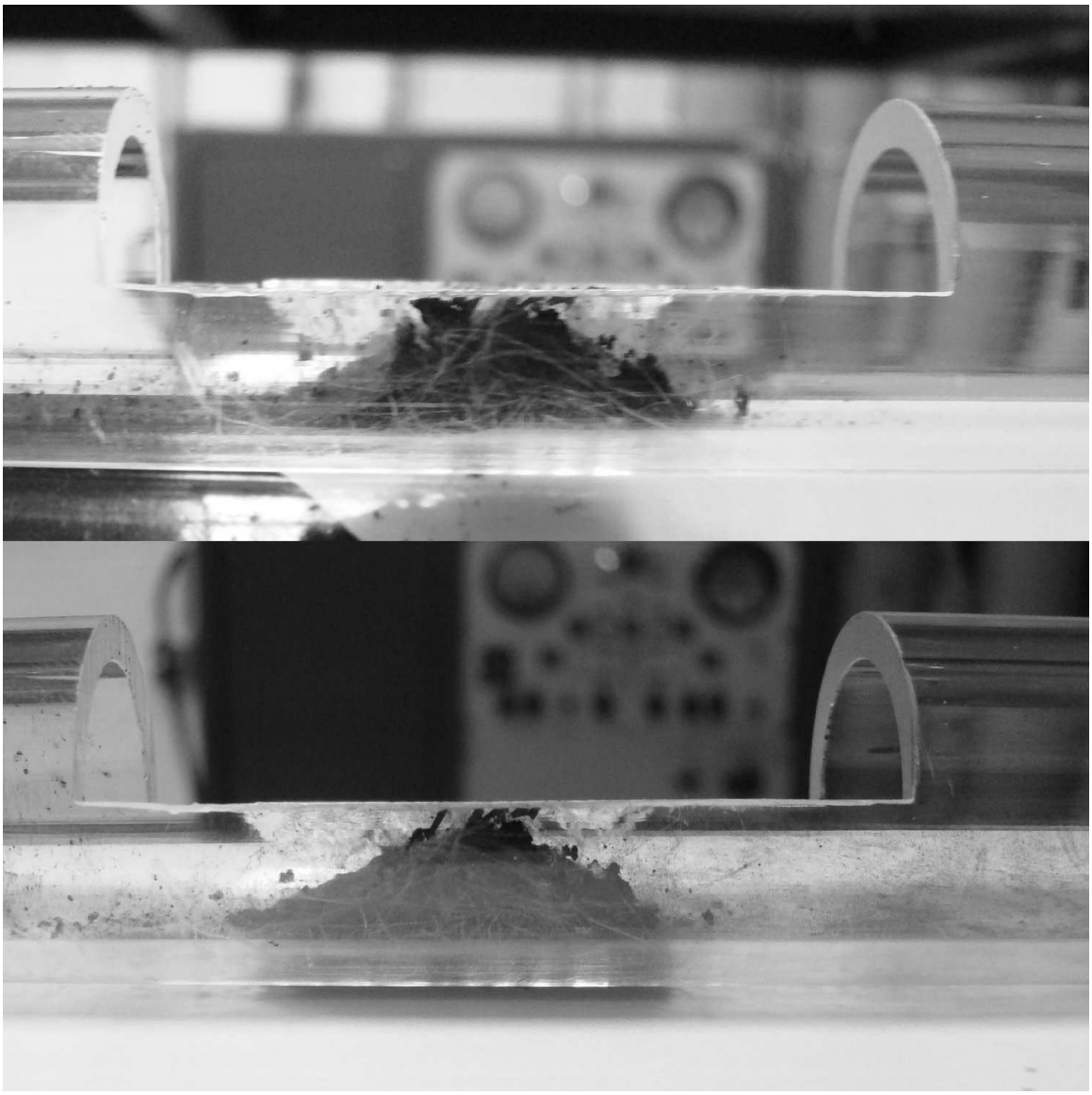

Figure B.5. Piles of 4 μm carbon dust before (top) and after (bottom) shear by a flow of helium up to Re = 930. While the majority of the pile was stable, some mobilization did occur. Note the irregularity of the pile due to cohesive and electrostatic effects, and the visible deposition downstream (right) of the pile.

C Appendix: Maple calculation of eigenvalues for GE-NLS

```
    |\^/|     Maple 10 (IBM INTEL LINUX)
._|\|   |/|_. Copyright (c) Maplesoft, a division of Waterloo Maple Inc. 2005
 \  MAPLE  /  All rights reserved. Maple is a trademark of
 <____ ____>  Waterloo Maple Inc.
      |       Type ? for help.
> with(linalg):
Warning, the protected names norm and trace have been redefined and unprotected
> st:=matrix([[u11,u12,u13],[u21,u22,u23],[u31,u32,u33]]):
> dst:=([[u11-(1/3)*trace(st),u12,u13],[u21,u22-(1/3)*trace(st),u23],
> [u31,u32,u33-(1/3)*trace(st)]]):
> uI:=trace(st):
> uII:=dst[1,1]^2+dst[1,2]^2+dst[1,3]^2+dst[2,1]^2+dst[2,2]^2+dst[2,3]^2+
> dst[3,1]^2+dst[3,2]^2+dst[3,3]^2:
> uIII:=det(dst):
> F:=G*((-uI)^(b+2))*((2/5)*xi+(uII/((-uI)^2))+z*(uIII/((-uI)^3))):
> F:=subs(u11=u1,u22=u2,u33=u3,u12=g4/2,u21=g4/2,u23=g5/2,u32=g5/2,u13=g6/2,
> u31=g6/2,F):
> F:=subs(b=1,F):
> D11:=simplify(diff(diff(F,u1),u1)):
> D12:=simplify(diff(diff(F,u1),u2)):
> D13:=simplify(diff(diff(F,u1),u3)):
> D14:=simplify(diff(diff(F,u1),g4)):
> D15:=simplify(diff(diff(F,u1),g5)):
> D16:=simplify(diff(diff(F,u1),g6)):
> D21:=simplify(diff(diff(F,u2),u1)):
> D22:=simplify(diff(diff(F,u2),u2)):
> D23:=simplify(diff(diff(F,u2),u3)):
> D24:=simplify(diff(diff(F,u2),g4)):
> D25:=simplify(diff(diff(F,u2),g5)):
> D26:=simplify(diff(diff(F,u2),g6)):
> D31:=simplify(diff(diff(F,u3),u1)):
> D32:=simplify(diff(diff(F,u3),u2)):
> D33:=simplify(diff(diff(F,u3),u3)):
```

```
> D34:=simplify(diff(diff(F,u3),g4)):
> D35:=simplify(diff(diff(F,u3),g5)):
> D36:=simplify(diff(diff(F,u3),g6)):
> D41:=simplify(diff(diff(F,g4),u1)):
> D42:=simplify(diff(diff(F,g4),u2)):
> D43:=simplify(diff(diff(F,g4),u3)):
> D44:=simplify(diff(diff(F,g4),g4)):
> D45:=simplify(diff(diff(F,g4),g5)):
> D46:=simplify(diff(diff(F,g4),g6)):
> D51:=simplify(diff(diff(F,g5),u1)):
> D52:=simplify(diff(diff(F,g5),u2)):
> D53:=simplify(diff(diff(F,g5),u3)):
> D54:=simplify(diff(diff(F,g5),g4)):
> D55:=simplify(diff(diff(F,g5),g5)):
bytes used=4000024, alloc=3472772, time=0.05
> D56:=simplify(diff(diff(F,g5),g6)):
> D61:=simplify(diff(diff(F,g6),u1)):
> D62:=simplify(diff(diff(F,g6),u2)):
> D63:=simplify(diff(diff(F,g6),u3)):
> D64:=simplify(diff(diff(F,g6),g4)):
> D65:=simplify(diff(diff(F,g6),g5)):
> D66:=simplify(diff(diff(F,g6),g6)):
> M:=matrix([[D11,D12,D13,D14,D15,D16],[D21,D22,D23,D24,D25,D26],
> [D31,D32,D33,D34,D35,D36],[D41,D42,D43,D44,D45,D46],
> [D51,D52,D53,D54,D55,D56],[D61,D62,D63,D64,D65,D66]]):
> u1:=0:
> u3:=0:
> g5:=0:
> g6:=0:
> S2:=diff(F,u2):
> T4:=diff(F,g4):
> eigvs:=eigenvals(M):
bytes used=8000388, alloc=4455632, time=0.12
> eigv1:=eigvs[1];
```

```
                          /               2   2    2   2 1/2\
                          |      z u2   (z  u2  + z  g4 )   |
                eigv1 := |-u2 - ---- + --------------------| G
                          \       12             4         /
> eigv2:=eigvs[2];
                          /               2   2    2   2 1/2\
                          |      z u2   (z  u2  + z  g4 )   |
                eigv2 := |-u2 - ---- - --------------------| G
                          \       12             4         /
> eigv3:=eigvs[3];
                      4             4            2   2         4           4  2
eigv3 := RootOf(270 _Z  + 7776 xi u2  - 1080 z g4  u2  - 720 u2  z + 240 u2  z
               2  3   2          2   2        2   2   2           2  2   2
     + 108 xi u2  z  g4  - 3240 g4  u2  + 270 z  g4  u2  - 648 xi u2  z  g4
               4  3          4             4              4  2              3
     + 144 xi u2  z  - 4320 u2  - 1296 xi u2  z - 864 xi u2  z  + (-1260 z u2
           2      2       3      2              2             3
     - 90 z  u2 g4  + 15 z  u2 g4  - 540 z u2 g4  - 1296 xi u2  z
            2   3             3              2   2          2           2   3
     - 864 z  u2  xi - 5400 u2  - 324 xi u2 z  g4  - 3240 g4  u2 - 120 z  u2
                  3       3   3
     + 15552 xi u2  + 20 z  u2 ) _Z + (
         2   2            2          2   2         2              2         2
    -45 z  g4  - 324 xi u2  z - 120 z  u2  - 180 u2  z + 9720 xi u2  - 810 g4 )
      2                                      3
    _Z  + (-45 z u2 + 1944 xi u2 + 1350 u2) _Z , label = _L2) G
> req1:=simplify((solve(eigv1=0,g4)[1])^2);
                                            2         2
                                 8 (-3 z + z  - 18) u2
                       req1 := - ----------------------
                                             2
                                          9 z
> req2:=simplify((solve(eigv2=0,g4)[1])^2);
```

```
                                              2         2
                                    8 (-3 z + z  - 18) u2
                          req2 := - ----------------------
                                                2
                                             9 z
> req3:=simplify((solve(eigv3=0,g4)[1])^2);
bytes used=12000792, alloc=5045348, time=0.19
                                  2             2
                              8 u2  (15 + 3 xi z  + 5 z - 27 xi)
                     req3 := - ----------------------------------
                                             2
                                  9 (2 xi z  + 5 z + 10)
> simplify(diff(req3,xi));
                                  2   3
                               40 u2  (z  - 27 z - 54)
                             - ----------------------
                                        2            2
                               9 (2 xi z  + 5 z + 10)
> req3_lim:=limit(req3,xi=infinity);
                                           2   2
                                      4 u2  (z  - 9)
                            req3_lim := - --------------
                                                2
                                           3 z
> tan2phi:=simplify((T4/S2)^2);
                                        2   2         2
                                   900 u2  g4  (-6 + z)
          tan2phi := ------------------------------------------------------
                                2         2        2        2            2 2
                     (-216 xi u2  - 360 u2  - 90 g4  + 40 u2  z + 15 z g4 )
> tan2phi:=simplify(subs(g4=sqrt(req3),tan2phi));
```

```
                      2                    2            2
tan2phi := - 225 (2 xi z  + 5 z + 10) (-6 + z)  (15 + 3 xi z  + 5 z - 27 xi)
       /           2  2                              2
      /  (2 (-162 xi  z  - 270 xi z - 1620 xi - 180 xi z  - 450 z - 900
     /
              3       2 2
     + 15 xi z  + 50 z ) )
> phi:=(180/Pi)*arctan(sqrt(tan2phi));
                     /         2                     2
phi := 180 arctan(15 |- (4 xi z  + 10 z + 20) (-6 + z)
                     \
                2                 /         2  2
    (15 + 3 xi z  + 5 z - 27 xi)  /  (-162 xi  z  - 270 xi z - 1620 xi
                                 /
              2                       3       2 2\1/2
     - 180 xi z  - 450 z - 900 + 15 xi z  + 50 z ) |   /2)/Pi
                                                   /
> phimax:=Optimization:-Maximize(phi,xi=0..2,z=0..2);
      phimax := [17.0238661849957715, [z = 0., xi = 1.66666667152813352]]
> phi_GEL:=simplify(subs(z=0,phi));
                                        1/2 / -5 + 9 xi \1/2
                                      15    |-----------|
                                            |          2|
                                            \(5 + 9 xi) /
                              180 arctan(----------------------)
                                                 2
                 phi_GEL := ---------------------------------
                                              Pi
> quit
bytes used=15157824, alloc=5045348, time=0.24
```

D Appendix: Plane stress solution for the Einav-Puzrin model

```
    |\^/|     Maple 10 (IBM INTEL LINUX)
._|\|   |/|_. Copyright (c) Maplesoft, a division of Waterloo Maple Inc. 2005
 \  MAPLE  /  All rights reserved. Maple is a trademark of
 <____ ____>  Waterloo Maple Inc.
      |       Type ? for help.
> G:=sqrt(P^3/B)*(b+(Ss/P)^2);
                                  /  3 \1/2 /      2\
                                  | P  |    |    Ss |
                             G := |----|    |b + ---|
                                  \ B  /    |     2 |
                                            \    P  /
> G:=subs(Ss=sqrt(s1^2+s2^2+s3^2+2*t4^2+2*t5^2+2*t6^2-3*P^2),P=-(s1+s2+s3)/3,G):
> s3:=0:
> t5:=0:
> t6:=0:
> u2:=diff(G,s2):
> g4:=diff(G,t4):
> sx:=solve(diff(G,s1)=0,s1);
                              2         2       2          2 1/2
        3 s2 + b s2 - (45 s2  + 6 b s2  + 6 t4  b + 36 t4 )
sx := - ----------------------------------------------------,
                                b + 6
                            2         2       2          2 1/2
      3 s2 + b s2 + (45 s2  + 6 b s2  + 6 t4  b + 36 t4 )
    - ----------------------------------------------------
                                b + 6
> s1a:=evalf(subs(b=2,s2=-1000,t4=0,sx[1]));
                                 s1a := 1568.729304
> s1b:=evalf(subs(b=2,s2=-1000,t4=0,sx[2]));
                                s1b := -318.7293044
> u2:=simplify(subs(s1=sx[2],u2));
bytes used=4000052, alloc=3472772, time=0.08
```

```
                2   4   1/2           5         2   3         5       2   5
u2 := - 72 (-3 b  s2  %1    + 270 b s2  + 108 t4  s2  + 324 s2  + 45 b  s2
             4   1/2        2  2   3         2     3      3   5       2   3  3
     - 30 b s2  %1    + 66 t4  b  s2  + 270 t4  b s2  + 2 b  s2  + 4 t4  s2  b
              4  2           4            4  3            4
     + 21 s2 t4  b  + 36 s2 t4  b + 2 s2 t4  b  - 108 s2 t4
           2  2   2   1/2       2     2   1/2        2   2   1/2        4   1/2
     - 2 t4  b  s2  %1    - 6 t4  b s2  %1    + 36 t4  s2  %1    - 36 s2  %1
                                                                 /
            4   1/2    2   1/2   4          1/2   4   1/2   / |
     + 36 t4  %1    + b  %1    t4  + 12 b %1    t4 ) 3     /  |B
                                                         /   |
                                                             \
                              /            1/2 3\1/2\
              1/2 3        2 |  (3 s2 - %1   ) |   |
    (3 s2 - %1   )  (b + 6)  |- ---------------|   |
                              |           3     |   |
                              \    (b + 6)  B   /   /
           2         2       2          2
%1 := 45 s2  + 6 b s2  + 6 t4  b + 36 t4
> g4:=simplify(subs(s1=sx[2],g4));
              /                2         2       2          2 1/2 3\1/2
         1/2 |  (3 s2 - (45 s2  + 6 b s2  + 6 t4  b + 36 t4 )   ) |
g4 := 4 3    |- ------------------------------------------------|    t4
              |                              3                    |
              \                      (b + 6)  B                   /
           2   /               2         2       2          2 1/2 2
    (b + 6)   /  (3 s2 - (45 s2  + 6 b s2  + 6 t4  b + 36 t4 )   )
              /
> r:=simplify(g4/u2);
```

```
                1/2 4              /          2   4   1/2           5
r := (3 s2 - %1    )  (b + 6) t4  /  (18 (-3 b  s2  %1    + 270 b s2
                                  /
              2   3         5       2   5          4   1/2        2  2   3
     + 108 t4  s2  + 324 s2  + 45 b  s2  - 30 b s2  %1    + 66 t4  b  s2
             2     3      3   5       2   3  3           4  2           4
     + 270 t4  b s2  + 2 b  s2  + 4 t4  s2  b  + 21 s2 t4  b  + 36 s2 t4  b
              4  3            4       2  2   2   1/2       2     2   1/2
     + 2 s2 t4  b  - 108 s2 t4  - 2 t4  b  s2  %1    - 6 t4  b s2  %1
            2   2   1/2        4   1/2        4   1/2    2   1/2   4
     + 36 t4  s2  %1    - 36 s2  %1    + 36 t4  %1    + b  %1    t4
              1/2   4
     + 12 b %1    t4 ))
           2         2       2          2
%1 := 45 s2  + 6 b s2  + 6 t4  b + 36 t4
> r:=subs(t4=R*s2,r);
                1/2 4               /          2   4   1/2           5
r := (3 s2 - %1    )  (b + 6) R s2  /  (18 (-3 b  s2  %1    + 270 b s2
                                  /
              2   5         5       2   5          4   1/2       2   5  2
     + 108 R  s2  + 324 s2  + 45 b  s2  - 30 b s2  %1    + 66 R  s2  b
            2   5        3   5      2   5  3        5  4  2        5  4
     + 270 R  s2  b + 2 b  s2  + 4 R  s2  b  + 21 s2  R  b  + 36 s2  R  b
           5  4  3         5  4      2   4  2   1/2      2   4     1/2
     + 2 s2  R  b  - 108 s2  R  - 2 R  s2  b  %1    - 6 R  s2  b %1
           2   4   1/2        4   1/2       4   4   1/2    2   1/2  4   4
     + 36 R  s2  %1    - 36 s2  %1    + 36 R  s2  %1    + b  %1    R  s2
              1/2  4   4
     + 12 b %1    R  s2 ))
           2         2      2   2         2   2
%1 := 45 s2  + 6 b s2  + 6 R  s2  b + 36 R  s2
> r:=subs(s2=1,r);
```

```
            1/2 4             /          2   1/2                2             2
r := (3 - %1   )  (b + 6) R  /  (18 (-3 b  %1    + 270 b + 108 R  + 324 + 45 b
                            /

              1/2       2  2        2        3      2  3       4  2       4
     - 30 b %1    + 66 R  b  + 270 R  b + 2 b  + 4 R  b  + 21 R  b  + 36 R  b
          4  3        4      2  2   1/2      2     1/2       2   1/2        1/2
     + 2 R  b  - 108 R  - 2 R  b  %1    - 6 R  b %1    + 36 R  %1    - 36 %1
           4   1/2    2   1/2  4          1/2  4
     + 36 R  %1    + b  %1    R  + 12 b %1    R ))
                    2         2
%1 := 45 + 6 b + 6 R  b + 36 R
> r_max:=simplify(limit(r,R=infinity));
                                        1/2
                                     2 3    (b + 6)
                            r_max := ---------------
                                                1/2
                                     3 (2 b + 12)
> quit
bytes used=7702360, alloc=4586680, time=0.16
```

E Appendix: Legendre Transform of the HAR Model

As the details of obtaining the Gibbs free energy of the HAR model are not given in [67, 76], they are presented here for clarity. We begin with the Helmholtz free energy,

$$\mathcal{F} = A\left(\alpha\Delta^2 + u_s^2\right)^{\frac{3}{2}} \tag{E.1}$$

and wish to obtain the (negative) Gibbs free energy $\mathcal{G}$ via the Legendre transform,

$$\mathcal{G} = P\Delta + \sigma_s u_s - \mathcal{F} \tag{E.2}$$

First we need to solve for Δ, u_s in terms of the stress invariants. We have

$$\frac{\partial\mathcal{F}}{\partial\Delta} = P = 3A\alpha\Delta\left(\alpha\Delta^2 + u_s^2\right)^{\frac{1}{2}} \tag{E.3}$$

$$\frac{\partial\mathcal{F}}{\partial u_s} = \sigma_s = 3Au_s\left(\alpha\Delta^2 + u_s^2\right)^{\frac{1}{2}} \tag{E.4}$$

which can be rearranged to

$$u_s^2 = \frac{P^2}{9A^2\alpha^2\Delta^2} - \alpha\Delta^2 \tag{E.5}$$

$$\alpha\Delta^2 = \frac{\sigma_s^2}{9A^2u_s^2} - u_s^2 \tag{E.6}$$

Substituting $\alpha\Delta^2$ from the second expression into the first,

$$u_s^2 = \frac{P^2}{9A^2\alpha\left(\frac{\sigma_s^2}{9A^2u_s^2} - u_s^2\right)} - \frac{\sigma_s^2}{9A^2u_s^2} + u_s^2 \tag{E.7}$$

The u_s^2 terms cancel from each side, and

$$\frac{\sigma_s^2}{9A^2u_s^2} = \frac{P^2}{9A^2\alpha\left(\frac{\sigma_s^2}{9A^2u_s^2} - u_s^2\right)} \tag{E.8}$$

Solving for P^2,

$$P^2 = \frac{\sigma_s^2}{9A^2u_s^2}\left(\frac{\alpha\sigma_s^2}{u_s^2} - 9A^2\alpha u_s^2\right) \tag{E.9}$$

or

$$P^2 = \frac{\alpha\sigma_s^4}{9A^2u_s^4} - \alpha\sigma_s^2 \tag{E.10}$$

Solving for u_s, we obtain

$$u_s^4 = \frac{\alpha\sigma_s^4}{9A^2\left(P^2 + \alpha\sigma_s^2\right)} \tag{E.11}$$

$$u_s^2 = \frac{\sigma_s^2}{3A}\sqrt{\frac{\alpha}{\left(P^2 + \alpha\sigma_s^2\right)}} \tag{E.12}$$

and

$$u_s = \frac{\sigma_s}{\sqrt{3A}}\left(\frac{\alpha}{\left(P^2 + \alpha\sigma_s^2\right)}\right)^{\frac{1}{4}} \tag{E.13}$$

Substituting the above expression for u_s^2 into equation E.6,

$$\alpha\Delta^2 = \frac{\sigma_s^2}{9A^2\left(\frac{\sigma_s^2}{3A}\sqrt{\frac{\alpha}{P^2+\alpha\sigma_s^2}}\right)} - \frac{\sigma_s^2}{3A}\sqrt{\frac{\alpha}{P^2+\alpha\sigma_s^2}} \tag{E.14}$$

Canceling σ_s and $3A$ terms gives

$$\alpha\Delta^2 = \frac{1}{\frac{1}{3A}\sqrt{\frac{\alpha}{P^2+\alpha\sigma_s^2}}} - \frac{\sigma_s^2}{3A}\sqrt{\frac{\alpha}{P^2+\alpha\sigma_s^2}} \tag{E.15}$$

which may be rewritten

$$3A\alpha\Delta^2\sqrt{\frac{\alpha}{P^2+\alpha\sigma_s^2}} = 1 - \frac{\alpha\sigma_s^2}{P^2+\alpha\sigma_s^2} \tag{E.16}$$

The right hand side simplifies as follows:

$$1 - \frac{\alpha\sigma_s^2}{P^2+\alpha\sigma_s^2} = \frac{P^2+\alpha\sigma_s^2}{P^2+\alpha\sigma_s^2} - \frac{\alpha\sigma_s^2}{P^2+\alpha\sigma_s^2} = \frac{P^2}{P^2+\alpha\sigma_s^2} \tag{E.17}$$

So,

$$3A\alpha\Delta^2\sqrt{\frac{\alpha}{P^2+\alpha\sigma_s^2}} = \frac{P^2}{P^2+\alpha\sigma_s^2} \tag{E.18}$$

and

$$3A\alpha\Delta^2 = \sqrt{\frac{P^2+\alpha\sigma_s^2}{\alpha}}\frac{P^2}{P^2+\alpha\sigma_s^2} \tag{E.19}$$

which leads to the solution for Δ,

$$\Delta^2 = \frac{P^2}{3A\alpha^{\frac{3}{2}}\sqrt{P^2+\alpha\sigma_s^2}} \tag{E.20}$$

and

$$\Delta = \frac{P}{\sqrt{3A}\alpha^{\frac{3}{4}}\left(P^2+\alpha\sigma_s^2\right)^{\frac{1}{4}}} \tag{E.21}$$

We may now insert the solutions for Δ and u_s (equations E.12, E.13, E.20, and E.21) into the Legendre transform, equation E.2:

$$\mathcal{G} = P\Delta + \sigma_s u_s - A\left(\alpha\Delta^2 + u_s^2\right)^{\frac{3}{2}} \tag{E.22}$$

$$= \frac{P^2}{\sqrt{3A}\alpha^{\frac{3}{4}}\left(P^2+\alpha\sigma_s^2\right)^{\frac{1}{4}}} + \frac{\alpha\sigma_s^2}{\sqrt{3A}\alpha^{\frac{3}{4}}\left(P^2+\alpha\sigma_s^2\right)^{\frac{1}{4}}} - A\left(\frac{\alpha P^2}{3A\alpha^{\frac{3}{2}}\left(P^2+\alpha\sigma_s^2\right)^{\frac{1}{2}}} + \frac{\alpha^{\frac{1}{2}}\sigma_s^2}{3A\left(P^2+\alpha\sigma_s^2\right)^{\frac{1}{2}}}\right)^{\frac{3}{2}} \tag{E.23}$$

$$= \frac{P^2+\alpha\sigma_s^2}{\sqrt{3A}\alpha^{\frac{3}{4}}\left(P^2+\alpha\sigma_s^2\right)^{\frac{1}{4}}} - A\left(\frac{P^2+\alpha\sigma_s^2}{3A\alpha^{\frac{1}{2}}\left(P^2+\alpha\sigma_s^2\right)^{\frac{1}{2}}}\right)^{\frac{3}{2}} \tag{E.24}$$

$$= \frac{\left(P^2+\alpha\sigma_s^2\right)^{\frac{3}{4}}}{\sqrt{3A}\alpha^{\frac{3}{4}}} - A\left(\frac{\left(P^2+\alpha\sigma_s^2\right)^{\frac{1}{2}}}{3A\alpha^{\frac{1}{2}}}\right)^{\frac{3}{2}} \tag{E.25}$$

$$= \frac{\left(P^2+\alpha\sigma_s^2\right)^{\frac{3}{4}}}{\sqrt{3A}\alpha^{\frac{3}{4}}} - A\frac{\left(P^2+\alpha\sigma_s^2\right)^{\frac{3}{4}}}{(3A)^{\frac{3}{2}}\alpha^{\frac{3}{4}}} \tag{E.26}$$

$$= \frac{\left(P^2 + \alpha\sigma_s^2\right)^{\frac{3}{4}}}{\sqrt{3A}\alpha^{\frac{3}{4}}} - \frac{1}{3}\frac{\left(P^2 + \alpha\sigma_s^2\right)^{\frac{3}{4}}}{(3A)^{\frac{1}{2}}\,\alpha^{\frac{3}{4}}} \tag{E.27}$$

which simplifies finally to the form of equation 3.147,

$$\mathcal{G} = \frac{2}{3\sqrt{3A}}\left(\frac{1}{\alpha}P^2 + \sigma_s^2\right)^{\frac{3}{4}} \tag{E.28}$$

F Appendix: Abaqus UMAT implementations

F.1 Granular Elasticity - Plane Strain/Axisymmetric Stress

```
************************************************************************
**  Granular Elasticity umat for abaqus/standard,                     **
**  plane strain and axi-symmetric elements.                          **
************************************************************************
      SUBROUTINE UMAT(STRESS,STATEV,DDSDDE,SSE,SPD,SCD,
     & RPL,DDSDDT,DRPLDE,DRPLDT,
     & STRAN,DSTRAN,TIME,DTIME,TEMP,DTEMP,PREDEF,DPRED,CMNAME,
     & NDI,NSHR,NTENS,NSTATV,PROPS,NPROPS,COORDS,DROT,PNEWDT,
     & CELENT,DFGRD0,DFGRD1,NOEL,NPT,LAYER,KSPT,KSTEP,KINC)
      INCLUDE 'ABA_PARAM.INC'
      CHARACTER*80 CMNAME
      DIMENSION STRESS(NTENS),STATEV(NSTATV),
     & DDSDDE(NTENS,NTENS),DDSDDT(NTENS),DRPLDE(NTENS),
     & STRAN(NTENS),DSTRAN(NTENS),TIME(2),PREDEF(1),DPRED(1),
     & PROPS(NPROPS),COORDS(3),DROT(3,3),DFGRD0(3,3),DFGRD1(3,3)
      parameter (one=1.d0,two=2.d0,three=3.d0,four=4.d0,six=6.d0)
      dimension dstress(4), dds(4,4)
      double precision A,d,d2,us2
c-----------------------------------------------------------------------
c  material properties - specify in problem input
      A = 5.1d9
c  calculate invariants
      d = -(stran(1)+stran(2)+stran(3))
      d2 = d**two
      us2 = stran(1)**two + stran(2)**two + stran(3)**two +
     &     (stran(4)**two)/two - d2/three
      if (d .lt. 1.d-10) then ! ensure positive compression
       d = 1.d-10
       d2 = d**two
      endif
c  stiffness matrix
      do j = 1,3
```

```
          do i = 1,3
           dds(i,j)=A*(14.d0*d2 - 3.d0*us2 - 12.d0*d*(stran(i)+stran(j))) /
     &            (12.d0*d**(three/two))
          end do
         end do
         do i = 1,3
          dds(i,i)=A*(38.d0*d2 - 3.d0*us2 - 24.d0*d*stran(i)) /
     &            (12.d0*d**(three/two))
         end do
         do i = 1,3
          dds(i,4)=-A*stran(4)/(two*dsqrt(d))
          dds(4,i)=dds(i,4)
         end do
         dds(4,4) = A*dsqrt(d)
c  stress increment
         do i = 1,4
          dstress(i)= dds(i,1)*dstran(1) + dds(i,2)*dstran(2) +
     &             dds(i,3)*dstran(3) + dds(i,4)*dstran(4)
         end do
c  update stress
         do i = 1,4
           stress(i) = stress(i) + dstress(i)
         end do
c  Jacobian
         do j = 1,4
          do i = 1,4
           ddsdde(i,j) = dds(i,j)
          end do
         end do
         return
         end
```

F.2 EP Model - Plane Strain/Axisymmetric Stress

```
************************************************************************
**  Einav/Puzrin hyperelastic umat for abaqus/standard,               **
**  plane strain and axi-symmetric elements.                          **
************************************************************************
      SUBROUTINE UMAT(STRESS,STATEV,DDSDDE,SSE,SPD,SCD,
     & RPL,DDSDDT,DRPLDE,DRPLDT,
     & STRAN,DSTRAN,TIME,DTIME,TEMP,DTEMP,PREDEF,DPRED,CMNAME,
     & NDI,NSHR,NTENS,NSTATV,PROPS,NPROPS,COORDS,DROT,PNEWDT,
     & CELENT,DFGRD0,DFGRD1,NOEL,NPT,LAYER,KSPT,KSTEP,KINC)
      INCLUDE 'ABA_PARAM.INC'
      CHARACTER*80 CMNAME
      DIMENSION STRESS(NTENS),STATEV(NSTATV),
     & DDSDDE(NTENS,NTENS),DDSDDT(NTENS),DRPLDE(NTENS),
     & STRAN(NTENS),DSTRAN(NTENS),TIME(2),PREDEF(1),DPRED(1),
     & PROPS(NPROPS),COORDS(3),DROT(3,3),DFGRD0(3,3),DFGRD1(3,3)
      parameter (one=1.d0,two=2.d0,three=3.d0,four=4.d0,six=6.d0)
      dimension dstress(4), dds(4,4)
      double precision B,beta,P,P2,Ss2
c-----------------------------------------------------------------------
c  material properties - specify in problem input
      B = props(1)
      beta = props(2)
c  calculate invariants
       P = -(stress(1)+stress(2)+stress(3))/three
       P2 = P**two
       Ss2 = stress(1)**two + stress(2)**two + stress(3)**two +
     &       two*stress(4)**two - three*P2
      if (P .lt. one) then ! ensure positive compression
       P = one
       P2 = P**two
      endif
c  stiffness matrix
      do j = 1,3
```

```
          do i = 1,3
           dds(i,j)=dsqrt(B*P)*(six*(P-stress(i))*(P-stress(j)) -
     &           three*beta*P2 - Ss2) / (six*(three*beta*P2 + Ss2))
          end do
         end do
         do i = 1,3
          dds(i,i)=dsqrt(B*P)*(three*(P-stress(i))**two+three*beta*P2+Ss2) /
     &          (three*(three*beta*P2 + Ss2))
         end do
         do i = 1,3
          dds(i,4)=dsqrt(B*P)*(stress(4)*(P-stress(i)))/(three*beta*P2+Ss2)
          dds(4,i)=dds(i,4)
         end do
         dds(4,4) = (four*(stress(4))**two + three*beta*P2 + Ss2) *
     &           dsqrt(B*P) / (four*(three*beta*P2 + Ss2))
c  stress increment
         do i = 1,4
          dstress(i)= dds(i,1)*dstran(1) + dds(i,2)*dstran(2) +
     &             dds(i,3)*dstran(3) + dds(i,4)*dstran(4)
         end do
c  update stress
         do i = 1,4
           stress(i) = stress(i) + dstress(i)
         end do
c  Jacobian
         do j = 1,4
          do i = 1,4
           ddsdde(i,j) = dds(i,j)
          end do
         end do
         return
         end
```

F.3 HAR Model - Plane Strain/Axisymmetric Stress

```
************************************************************************
**  Houlsby/Amorosi/Rojas hyperelastic umat for abaqus/standard,       **
**  plane strain and axi-symmetric elements.                          **
************************************************************************
      SUBROUTINE UMAT(STRESS,STATEV,DDSDDE,SSE,SPD,SCD,
     & RPL,DDSDDT,DRPLDE,DRPLDT,
     & STRAN,DSTRAN,TIME,DTIME,TEMP,DTEMP,PREDEF,DPRED,CMNAME,
     & NDI,NSHR,NTENS,NSTATV,PROPS,NPROPS,COORDS,DROT,PNEWDT,
     & CELENT,DFGRD0,DFGRD1,NOEL,NPT,LAYER,KSPT,KSTEP,KINC)
      INCLUDE 'ABA_PARAM.INC'
      CHARACTER*80 CMNAME
      DIMENSION STRESS(NTENS),STATEV(NSTATV),
     & DDSDDE(NTENS,NTENS),DDSDDT(NTENS),DRPLDE(NTENS),
     & STRAN(NTENS),DSTRAN(NTENS),TIME(2),PREDEF(1),DPRED(1),
     & PROPS(NPROPS),COORDS(3),DROT(3,3),DFGRD0(3,3),DFGRD1(3,3)
      parameter (one=1.d0,two=2.d0,three=3.d0,four=4.d0,six=6.d0)
      dimension dstress(4), dds(4,4)
      double precision A,alpha,d,d2,us2
c-----------------------------------------------------------------------
c  material properties - specify in problem input
      A = props(1)
      alpha = props(2)
c  calculate invariants
      d = -(stran(1)+stran(2)+stran(3))
      d2 = d**two
      us2 = stran(1)**two + stran(2)**two + stran(3)**two +
     &     (stran(4)**two)/two - d2/three
      if (d .lt. 1.d-10) then ! ensure positive compression
       d = 1.d-10
       d2 = d**two
      endif
c  stiffness matrix
      do j = 1,3
```

```
        do i = 1,3
         dds(i,j) = A*(9.d0*stran(i)*stran(j) - three*us2 + d2
     &           + three*d*(stran(i)+stran(j)) - 9.d0*alpha*d2
     &           + 18.d0*(alpha**two)*d2 + 9.d0*alpha*us2
     &           - 9.d0*alpha*d*(stran(i)+stran(j)))
     &           / (three*dsqrt(alpha*d2+us2))
        end do
       end do
       do i = 1,3
        dds(i,i) = A*(9.d0*stran(i)**two + six*us2 + d2 + six*stran(i)*d
     &          + 18.d0*(alpha**two)*d2 + 9.d0*alpha*us2
     &          - 18.d0*alpha*stran(i)*d) / (three*dsqrt(alpha*d2+us2))
       end do
       do i = 1,3
        dds(i,4) = -A*(three*alpha*d - three*stran(i) - d) * stran(4)
     &          / (two*dsqrt(alpha*d2+us2))
        dds(4,i) = dds(i,4)
       end do
       dds(4,4) = A*(six*us2 + (three*alpha + one)*d2
     &         - three*(stran(1)**two + stran(2)**two + stran(3)**two))
     &         / (two*dsqrt(alpha*d2+us2))
c  stress increment
       do i = 1,4
        dstress(i)= dds(i,1)*dstran(1) + dds(i,2)*dstran(2) +
     &             dds(i,3)*dstran(3) + dds(i,4)*dstran(4)
       end do
c  update stress
       do i = 1,4
         stress(i) = stress(i) + dstress(i)
       end do
c  Jacobian
       do j = 1,4
        do i = 1,4
         ddsdde(i,j) = dds(i,j)
        end do
```

```
end do
return
end
```

σ_1	σ_2	Analytical	Abaqus
1000	500	u_1 = -2.239e-4 u_2 = -8.250e-5	u_1 = -2.261e-4 u_2 = -8.328e-5
1000	1000	u_1 = -1.837e-4 u_2 = -1.837e-4	u_1 = -1.855e-4 u_2 = -1.855e-4
1000	1500	u_1 = -1.479e-4 u_2 = -2.574e-4	u_1 = -1.493e-4 u_2 = -2.599e-4

Table F.1. Abaqus results for a single quadratic, reduced integration, plane stress element.

F.4 Einav and Puzrin Model - Plane Stress

F.4.1 Compliance and Stiffness Matrices

In the case of plane stress, we have $u_3 = \gamma_5 = \gamma_6 = 0$, and $\sigma_3 = \tau_5 = \tau_6 = 0$ [141]. Substituting the three vanishing components of stress into the compliance matrix, it simplifies to

$$C = \begin{bmatrix} \frac{1}{12\sqrt{BP}}\left(\frac{\sigma_s^2}{P^2} + 8\frac{\sigma_1}{P} + \beta + 24\right) & \frac{1}{12\sqrt{BP}}\left(\frac{\sigma_s^2}{P^2} + \beta - 12\right) & \frac{2\tau_4}{3\sqrt{BP^3}} \\ \frac{1}{12\sqrt{BP}}\left(\frac{\sigma_s^2}{P^2} + \beta - 12\right) & \frac{1}{12\sqrt{BP}}\left(\frac{\sigma_s^2}{P^2} + 8\frac{\sigma_2}{P} + \beta + 24\right) & \frac{2\tau_4}{3\sqrt{BP^3}} \\ \frac{2\tau_4}{3\sqrt{BP^3}} & \frac{2\tau_4}{3\sqrt{BP^3}} & \frac{4}{\sqrt{BP}} \end{bmatrix} \tag{F.1}$$

The stiffness matrix M is obtained by inverting C,

$$M = \sqrt{BP}\begin{bmatrix} \frac{\left((3\beta+30)P^2+\sigma_s^2+6\sigma_1^2-2\sigma_2^2\right)}{4((3\beta+3)P^2+\sigma_s^2)} & \frac{-\left((3\beta-42)P^2+\sigma_s^2+2\left(\sigma_1^2+\sigma_2^2\right)\right)}{4((3\beta+3)P^2+\sigma_s^2)} & \frac{\tau_4(2\sigma_1-3P)}{(6\beta+6)P^2+2\sigma_s^2} \\ \frac{-\left((3\beta-42)P^2+\sigma_s^2+2\left(\sigma_1^2+\sigma_2^2\right)\right)}{4((3\beta+3)P^2+\sigma_s^2)} & \frac{\left((3\beta+30)P^2+\sigma_s^2+6\sigma_2^2-2\sigma_1^2\right)}{4((3\beta+3)P^2+\sigma_s^2)} & \frac{\tau_4(2\sigma_2-3P)}{(6\beta+6)P^2+2\sigma_s^2} \\ \frac{\tau_4(2\sigma_1-3P)}{(6\beta+6)P^2+2\sigma_s^2} & \frac{\tau_4(2\sigma_2-3P)}{(6\beta+6)P^2+2\sigma_s^2} & M_{33} \end{bmatrix} \tag{F.2}$$

$$M_{33} = \frac{\left((3\beta+9)P^2 + 3\sigma_s^2 - 2\left(\sigma_1^2+\sigma_2^2\right)\right)}{4\left((3\beta+3)P^2+\sigma_s^2\right)} \tag{F.3}$$

Abaqus benchmarks for the plane stress case are shown in table F.1.

F.4.2 UMAT

```
************************************************************************
**  Einav/Puzrin hyperelastic umat for abaqus/standard,               **
**  plane stress elements.                                            **
************************************************************************
      SUBROUTINE UMAT(STRESS,STATEV,DDSDDE,SSE,SPD,SCD,
     & RPL,DDSDDT,DRPLDE,DRPLDT,
     & STRAN,DSTRAN,TIME,DTIME,TEMP,DTEMP,PREDEF,DPRED,CMNAME,
     & NDI,NSHR,NTENS,NSTATV,PROPS,NPROPS,COORDS,DROT,PNEWDT,
     & CELENT,DFGRD0,DFGRD1,NOEL,NPT,LAYER,KSPT,KSTEP,KINC)
      INCLUDE 'ABA_PARAM.INC'
      CHARACTER*80 CMNAME
      DIMENSION STRESS(NTENS),STATEV(NSTATV),
     & DDSDDE(NTENS,NTENS),DDSDDT(NTENS),DRPLDE(NTENS),
     & STRAN(NTENS),DSTRAN(NTENS),TIME(2),PREDEF(1),DPRED(1),
     & PROPS(NPROPS),COORDS(3),DROT(3,3),DFGRD0(3,3),DFGRD1(3,3)
      parameter (one=1.d0,two=2.d0,three=3.d0,four=4.d0,six=6.d0)
      dimension dstress(3), dds(3,3)
      double precision B,beta,P,P2,Ss2
c-----------------------------------------------------------------------
c  material properties - specify in problem input
      B = props(1)
      beta = props(2)
c  calculate invariants
       P = -(stress(1)+stress(2))/three
       P2 = P**two
       Ss2 = stress(1)**two + stress(2)**two + two*stress(3)**two -
     &       three*P2
      if (P .lt. one) then ! ensure positive compression
       P = one
       P2 = P**two
      endif
c  stiffness matrix
      dds(1,1)=dsqrt(B*P)*(three*(beta+10.d0)*P2 + Ss2 +
```

```
     &         six*stress(1)**two - two*stress(2)**two) /
     &         (four*(three*(beta+one)*P2 + Ss2))
      dds(2,2)=dsqrt(B*P)*(three*(beta+10.d0)*P2 + Ss2 +
     &         six*stress(2)**two - two*stress(1)**two) /
     &         (four*(three*(beta+one)*P2 + Ss2))
      dds(1,2)=-dsqrt(B*P)*(three*(beta-14.d0)*P2 + Ss2 +
     &                         two*(stress(1)**two + stress(2)**two)) /
     &                        (four*(three*(beta+one)*P2 + Ss2))
      dds(2,1)=dds(1,2)
      do i = 1,2
       dds(i,3)=dsqrt(B*P)*stress(3)*(two*stress(i)-three*P) /
     &          (six*(beta+one)*P2 + two*Ss2)
       dds(3,i)=dds(i,3)
      end do
      dds(3,3) = dsqrt(B*P)*((three*beta+9.d0)*P2+ three*Ss2 -
     &                           two*(stress(1)**two+stress(2)**two)) /
     &           (four*((three*(beta+one)*P2) + Ss2))
c  stress increment
      do i = 1,3
       dstress(i)= dds(i,1)*dstran(1) + dds(i,2)*dstran(2) +
     &             dds(i,3)*dstran(3)
      end do
c  update stress
      do i = 1,3
        stress(i) = stress(i) + dstress(i)
      end do
c  Jacobian
      do j = 1,3
       do i = 1,3
        ddsdde(i,j) = dds(i,j)
       end do
      end do
      return
      end
```

F.5 Einav and Puzrin Model - 3D

F.5.1 3D stress

The full 3D stiffness matrix is obtained by inverting the full compliance matrix,

$$C_{ij} = \begin{bmatrix} & \hat{C} & & \frac{2\tau_4}{3\sqrt{BP^3}} & \frac{2\tau_5}{3\sqrt{BP^3}} & \frac{2\tau_6}{3\sqrt{BP^3}} \\ & & & \frac{2\tau_4}{3\sqrt{BP^3}} & \frac{2\tau_5}{3\sqrt{BP^3}} & \frac{2\tau_6}{3\sqrt{BP^3}} \\ & & & \frac{2\tau_4}{3\sqrt{BP^3}} & \frac{2\tau_5}{3\sqrt{BP^3}} & \frac{2\tau_6}{3\sqrt{BP^3}} \\ \frac{2\tau_4}{3\sqrt{BP^3}} & \frac{2\tau_4}{3\sqrt{BP^3}} & \frac{2\tau_4}{3\sqrt{BP^3}} & \frac{4}{\sqrt{BP}} & 0 & 0 \\ \frac{2\tau_5}{3\sqrt{BP^3}} & \frac{2\tau_5}{3\sqrt{BP^3}} & \frac{2\tau_5}{3\sqrt{BP^3}} & 0 & \frac{4}{\sqrt{BP}} & 0 \\ \frac{2\tau_6}{3\sqrt{BP^3}} & \frac{2\tau_6}{3\sqrt{BP^3}} & \frac{2\tau_6}{3\sqrt{BP^3}} & 0 & 0 & \frac{4}{\sqrt{BP}} \end{bmatrix} \tag{F.4}$$

with

$$\hat{C}_{ij} = \frac{1}{12\sqrt{BP}} \left(\frac{\sigma_s^2}{P^2} + \frac{4(\sigma_i + \sigma_j)}{P} + \beta + 24\delta_{ij} \right) \tag{F.5}$$

The stiffness matrix is

$$M = \sqrt{BP} \begin{bmatrix} \hat{M} & & \hat{M}_{CA} & & \\ & & \frac{\left(4\tau_4^2+3\beta P^2+\sigma_s^2\right)}{4(3\beta P^2+\sigma_s^2)} & \frac{\tau_4\tau_5}{(3\beta P^2+\sigma_s^2)} & \frac{\tau_4\tau_6}{(3\beta P^2+\sigma_s^2)} \\ \hat{M}_{CA}^T & & \frac{\tau_5\tau_4}{(3\beta P^2+\sigma_s^2)} & \frac{\left(4\tau_5^2+3\beta P^2+\sigma_s^2\right)}{4(3\beta P^2+\sigma_s^2)} & \frac{\tau_5\tau_6}{(3\beta P^2+\sigma_s^2)} \\ & & \frac{\tau_6\tau_4}{(3\beta P^2+\sigma_s^2)} & \frac{\tau_6\tau_5}{(3\beta P^2+\sigma_s^2)} & \frac{\left(4\tau_6^2+3\beta P^2+\sigma_s^2\right)}{4(3\beta P^2+\sigma_s^2)} \end{bmatrix} \tag{F.6}$$

where

$$\hat{M}_{CA} = \begin{bmatrix} \frac{\tau_4(P-\sigma_1)}{(3\beta P^2+\sigma_s^2)} & \frac{\tau_5(P-\sigma_1)}{(3\beta P^2+\sigma_s^2)} & \frac{\tau_6(P-\sigma_1)}{(3\beta P^2+\sigma_s^2)} \\ \frac{\tau_4(P-\sigma_2)}{(3\beta P^2+\sigma_s^2)} & \frac{\tau_5(P-\sigma_2)}{(3\beta P^2+\sigma_s^2)} & \frac{\tau_6(P-\sigma_2)}{(3\beta P^2+\sigma_s^2)} \\ \frac{\tau_4(P-\sigma_3)}{(3\beta P^2+\sigma_s^2)} & \frac{\tau_5(P-\sigma_3)}{(3\beta P^2+\sigma_s^2)} & \frac{\tau_6(P-\sigma_3)}{(3\beta P^2+\sigma_s^2)} \end{bmatrix} \tag{F.7}$$

and

$$\hat{M} = \begin{bmatrix} \frac{\left(3(P-\sigma_1)^2+3\beta P^2+\sigma_s^2\right)}{3(3\beta P^2+\sigma_s^2)} & \frac{\left(6(P-\sigma_1)(P-\sigma_2)-3\beta P^2-\sigma_s^2\right)}{6(3\beta P^2+\sigma_s^2)} & \frac{\left(6(P-\sigma_1)(P-\sigma_3)-3\beta P^2-\sigma_s^2\right)}{6(3\beta P^2+\sigma_s^2)} \\ \frac{\left(6(P-\sigma_2)(P-\sigma_1)-3\beta P^2-\sigma_s^2\right)}{6(3\beta P^2+\sigma_s^2)} & \frac{\left(3(P-\sigma_2)^2+3\beta P^2+\sigma_s^2\right)}{3(3\beta P^2+\sigma_s^2)} & \frac{\left(6(P-\sigma_2)(P-\sigma_3)-3\beta P^2-\sigma_s^2\right)}{6(3\beta P^2+\sigma_s^2)} \\ \frac{\left(6(P-\sigma_3)(P-\sigma_1)-3\beta P^2-\sigma_s^2\right)}{6(3\beta P^2+\sigma_s^2)} & \frac{\left(6(P-\sigma_3)(P-\sigma_2)-3\beta P^2-\sigma_s^2\right)}{6(3\beta P^2+\sigma_s^2)} & \frac{\left(3(P-\sigma_3)^2+3\beta P^2+\sigma_s^2\right)}{3(3\beta P^2+\sigma_s^2)} \end{bmatrix} \tag{F.8}$$

is the same as for the axisymmetric case. Abaqus benchmarks for the 3D case are shown in table F.2.

σ_1	σ_2	σ_3	Analytical	Abaqus
500	750	1000	u_1 = -6.895e-5 u_2 = -1.267e-4 u_3 = -1.844e-4	u_1 = -6.963e-5 u_2 = -1.279e-4 u_3 = -1.862e-4
1000	1000	1000	u_1 = -1.5e-4 u_2 = -1.5e-4 u_3 = -1.5e-4	u_1 = -1.514e-4 u_2 = -1.514e-4 u_3 = -1.514e-4
1000	1100	1200	u_1 = -1.380e-4 u_2 = -1.570e-4 u_3 = -1.761e-4	u_1 = -1.393e-4 u_2 = -1.586e-4 u_3 = -1.778e-4

Table F.2. Abaqus results for a single quadratic, reduced integration, 3D stress element.

F.5.2 UMAT

```
************************************************************************
**  Einav/Puzrin hyperelastic umat for abaqus/standard, 3D elements.   **
************************************************************************
      SUBROUTINE UMAT(STRESS,STATEV,DDSDDE,SSE,SPD,SCD,
     & RPL,DDSDDT,DRPLDE,DRPLDT,
     & STRAN,DSTRAN,TIME,DTIME,TEMP,DTEMP,PREDEF,DPRED,CMNAME,
     & NDI,NSHR,NTENS,NSTATV,PROPS,NPROPS,COORDS,DROT,PNEWDT,
     & CELENT,DFGRD0,DFGRD1,NOEL,NPT,LAYER,KSPT,KSTEP,KINC)
      INCLUDE 'ABA_PARAM.INC'
      CHARACTER*80 CMNAME
      DIMENSION STRESS(NTENS),STATEV(NSTATV),
     & DDSDDE(NTENS,NTENS),DDSDDT(NTENS),DRPLDE(NTENS),
     & STRAN(NTENS),DSTRAN(NTENS),TIME(2),PREDEF(1),DPRED(1),
     & PROPS(NPROPS),COORDS(3),DROT(3,3),DFGRD0(3,3),DFGRD1(3,3)
      parameter (one=1.d0,two=2.d0,three=3.d0,four=4.d0,six=6.d0)
      dimension dstress(6), dds(6,6)
      double precision B,beta,P,P2,Ss2
c-----------------------------------------------------------------------
c  material properties - specify in problem input
      B = props(1)
      beta = props(2)
c  calculate invariants
       P = -(stress(1)+stress(2)+stress(3))/three
       P2 = P**two
       Ss2 = stress(1)**two + stress(2)**two + stress(3)**two - three*P2
     &    + two*stress(4)**two + two*stress(5)**two + two*stress(6)**two
      if (P .lt. one) then ! ensure positive compression
       P = one
       P2 = P**two
      endif
c  stiffness matrix
      do j = 1,3
       do i = 1,3
```

```
          dds(i,j)=dsqrt(B*P)*(six*(P-stress(i))*(P-stress(j)) -
     &           three*beta*P2 - Ss2) / (six*(three*beta*P2 + Ss2))
         end do
        end do
        do i = 1,3
         dds(i,i)=dsqrt(B*P)*(three*(P-stress(i))**two+three*beta*P2+Ss2) /
     &          (three*(three*beta*P2 + Ss2))
        end do
        do j = 4,6
         do i = 1,3
          dds(i,j)=dsqrt(B*P)*(stress(j)*(P-stress(i)))/(three*beta*P2+Ss2)
          dds(j,i)=dds(i,j)
         end do
        end do
        do j = 4,6
         do i = 4,6
          dds(i,j)=dsqrt(B*P)*stress(i)*stress(j)/(three*beta*P2+Ss2)
          dds(j,i)=dds(i,j)
         end do
        end do
        do i = 4,6
         dds(i,i) = (four*(stress(i))**two + three*beta*P2 + Ss2) *
     &            dsqrt(B*P) / (four*(three*beta*P2 + Ss2))
        end do
c  stress increment
        do i = 1,6
         dstress(i) = dds(i,1)*dstran(1) + dds(i,2)*dstran(2) +
     &              dds(i,3)*dstran(3) + dds(i,4)*dstran(4) +
     &              dds(i,5)*dstran(5) + dds(i,6)*dstran(6)
        end do
c  update stress
        do i = 1,6
          stress(i) = stress(i) + dstress(i)
        end do
c  Jacobian
```

```
do j = 1,6
 do i = 1,6
  ddsdde(i,j) = dds(i,j)
 end do
end do
return
end
```

G Appendix: Extension to cohesive materials

It is readily observable that as particle size decreases, cohesive effects become important in the behavior of granular materials, a point not considered in the preceding analysis. In GE and EP, tension is strictly forbidden due to $\sqrt{\Delta}$ and $\sqrt{P}$ terms; in ILE and HAR, the material has the same behavior under both tension and compression. In the Mohr-Coulomb yield criterion (equation 2.9), the cohesive force is taken to be a constant, c. Jiang and Liu [69, 72] point out that addition of a term linear in the compressive strain Δ to the free energy of GE gives precisely this form:

$$\mathcal{F} = \tilde{G}\sqrt{\Delta}(\frac{2}{5}\xi\Delta^2 + u_s^2) + c\Delta \tag{G.1}$$

Then the pressure $P = \partial\mathcal{F}/\partial\Delta$ increases by a constant c and the shear (equation 3.48) is unchanged, resulting in the cohesive form of the Coulomb yield condition; this effectively changes the reference point for zero stress to some non-zero value of strain, and does not change the form of the stiffness matrix. The constant cohesion is understood to apply to wet granular materials; for dry powders, there may be cohesive effects for sufficiently small constituent particles, but it is not clear that the physics should be similar (others have questioned the assumption of constant cohesion, see [142]). As the Hertz problem is instructive in understanding non-linearity in bulk granular materials, a generalized particle interaction that includes adhesion may be a starting point in extending the theory to cohesive materials. The present state of such models will be briefly reviewed here.

G.1 Particle interaction models

Generalization of the Hertz model to incorporate attractive forces has been an area of active research for the last thirty years. Several generalized models have been presented, the differences being where (Figure G.1), and at what distance (Figure G.2), adhesive forces are assumed to act. The most general method specifies some interaction potential between particles. However, this approach results in analytically intractable integral equations [143], which are not suitable for present purposes. Alternately, a stress distribution may be specified in the contact region [143]; it is models of this type that will be considered here.

Bradley [145], considering adhesive forces between rigid spheres of radius R, determined the adhesive force to be $2\pi R\gamma$ based on an exact solution for the potential between spheres. Here γ is a "surface energy", with units of force/distance. The first extension of the elastic theory of Hertz was given by Johnson, Kendall, and Roberts [146], and is referred to as the JKR theory. Assuming that a surface energy $-\pi a^2\gamma$ acts in the contact area (and neglecting interactions outside the contact area), the Hertz equations are modified:

$$a = \left(\frac{R}{K}\right)^{1/3}\left(\sqrt{\frac{3}{2}\pi R\gamma} + \sqrt{F + \frac{3}{2}\pi R\gamma}\right)^{2/3} \tag{G.2}$$

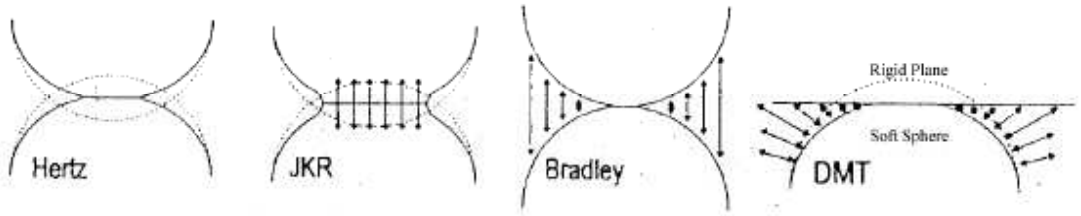

Figure G.1. Particle interaction models, from [28]. The Hertz model considers only elastic deformation. In the JKR theory, surface forces act only inside the contact circle. In the Bradley and DMT theories, van der Waals forces act outside the contact area. The DMT theory also includes elastic deformation; Bradley considers only rigid spheres.

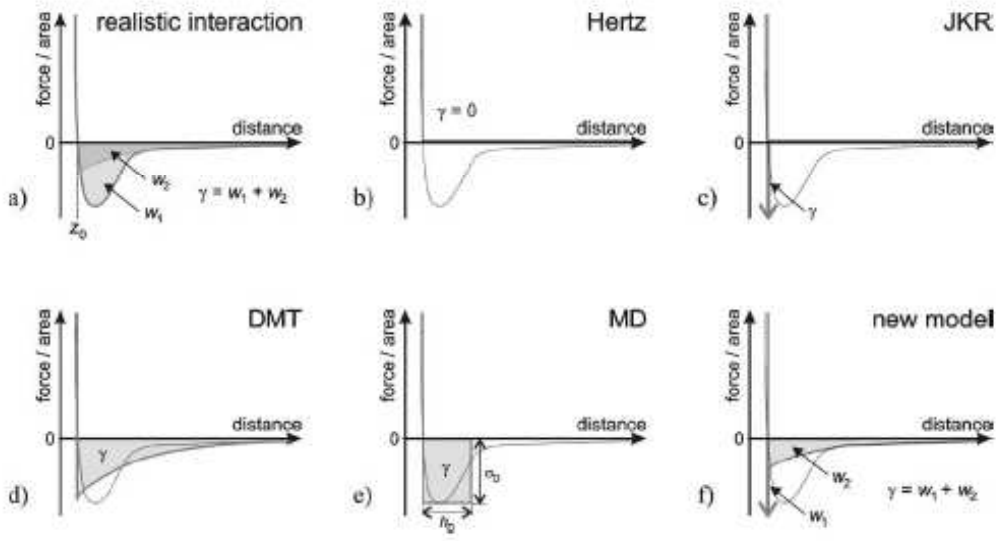

Figure G.2. A comparison of particle interaction models (reprinted from [144] with permission from Elsevier). The JKR theory (c) assumes short (infinitesimal) range forces, while in the DMT theory (d) they act over longer distances. In the transition regime, Schwarz proposes a superposition of the JKR and DMT models (f); Maugis uses a Dugale model (e).

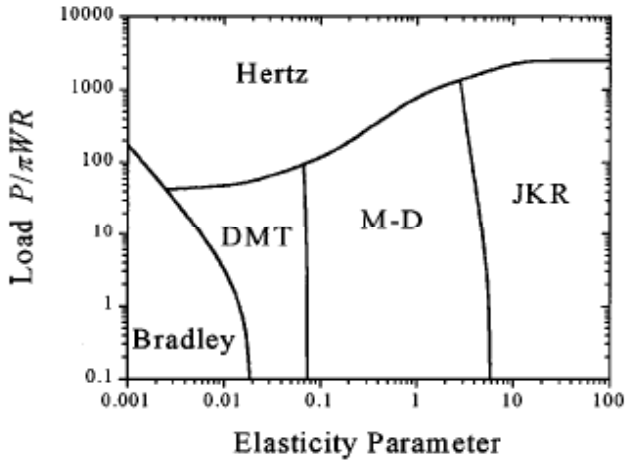

Figure G.3. Map of the various particle interaction models and there range of applicability (reprinted from [150] with permission from Elsevier). The elasticity parameter $\lambda = 1.16\mu$, with the Tabor parameter μ defined in equation G.6.

and

$$\delta = \frac{a^2}{R} - \sqrt{\frac{8\pi\gamma a}{3K}} \tag{G.3}$$

Here the pull-off force is $(3/2)\pi R\gamma$, seemingly in contradiction with Bradley's result. An alternate theory was subsequently introduced by Derjaguin, Muller, and Toporov (the DMT theory [147]), which did not result in analytical expressions. An approximation by Maugis [148] results in the DMT-M theory, which is somewhat the opposite of the JKR theory; the stress inside the contact area is assumed to Hertzian (i.e., no adhesive forces act there), but van der Waals forces acting outside the contact result in a constant offset to the applied force:

$$a = \left(\frac{R\left(F + 2\pi R\gamma\right)}{K}\right)^{1/3} \tag{G.4}$$

and

$$\delta = \frac{a^2}{R} \tag{G.5}$$

Tabor [149] showed that these were limiting cases, with the transition governed by the parameter

$$\mu \equiv \left(\frac{4R\gamma^2}{3K^2 z_0^3}\right)^{1/3} \tag{G.6}$$

with K defined in equation 2.18 and z_0 the effective range of surface forces. The JKR limit applies for $\mu \gtrsim 5$, while the DMT limit applies for $\mu \lesssim 0.1$ (Figure G.3). Thus, the JKR limit is understood to apply to "large, compliant spheres" and the DMT limit to "small, stiff spheres" [150]. Considerable effort has since been devoted to modeling the transition region, whether via approximate [144, 148] or exact numerical calculations using the Lennard-Jones potential [151].

While the displacement-force relationship $\delta(F)$ cannot be inverted for the JKR model, the DMT model results in the following:

$$F = KR^{1/2}\delta^{3/2} - 2\pi R\gamma \tag{G.7}$$

This is the Hertz model with a constant offset, consistent with a constant cohesion. In addition, identifying the strain ϵ in terms of the displacement δ and particle radius R,

$$\epsilon = \frac{\delta}{R} \tag{G.8}$$

the force is given by

$$F = KR^2\epsilon^{3/2} - 2\pi R\gamma \tag{G.9}$$

The weaker dependence of the adhesive term on R (linear vs. quadratic) indicates that adhesion becomes important for small particle radii, as is observed for granular materials. Thus, a simple constant cohesion may be justified by individual particle models. Addition of this effect to hyperelastic models is trivially simple and would provide at least a useful starting point for considering cohesive materials.

Bibliography

[1] P.-G. de Gennes, "Granular matter: a tentative view," *Reviews of Modern Physics*, vol. 71, no. 2, pp. S374–S382, 1999.

[2] K. Kamrin and M. Z. Bazant, "Stochastic flow rule for granular materials," *Physical Review E*, vol. 75, p. 041301, 2007.

[3] ANSYS, Inc., *Fluent 6.3 User's Guide*, 2008. `http://fluent.com`.

[4] W. J. Carmack, R. A. Anderl, R. J. Pawelko, G. R. Smolik, and K. A. McCarthy, "Characterization and analysis of dusts produced in three experimental tokamaks: TFTR, DIII-D, and Alcator C-Mod," *Fusion Engineering and Design*, vol. 51-52, pp. 477–484, 2000.

[5] J. P. Sharpe, D. A. Petti, and H.-W. Bartels, "A review of dust in fusion devices: Implications for safety and operational performance," *Fusion Engineering and Design*, vol. 63-64, pp. 153–163, 2002.

[6] R. Moormann, "Fission product transport and source terms in HTRs: Experience from AVR pebble bed reactor," *Science and Technology of Nuclear Installations*, vol. 2008, p. 597491, 2008.

[7] P. W. Humrickhouse and J. P. Sharpe, "Dust mobilization and transport modeling for loss of vacuum accidents," *Fusion Engineering and Design*, vol. 83, pp. 1721–1724, 2008.

[8] C.-A. Coulomb, "Essai sur une application des règles de maximis et minimis à quelques problèmes de statique, relatifs à l'architecture," *Mémoires de Mathématique de l'Académie Royale des Sciences*, vol. 7, pp. 343–382, 1776.

[9] R. M. Nedderman, *Statics and Kinematics of Granular Materials*. Cambridge: Cambridge University Press, 1992.

[10] A. Modaressi and P. Evesque, "Is the friction angle the maximum slope of a free surface of a non cohesive material?," *Poudres et Grains*, vol. 12, no. 5, pp. 83–102, 2001. `http://www.mssmat.ecp.fr/IMG/pdf/poudres12_5-Avalanching-Modaress-Evesq.pdf`.

[11] H. J. Herrmann, "On the shape of a sandpile," in *Physics of Dry Granular Media* (H. J. Herrmann, J.-P. Hovi, and S. Luding, eds.), pp. 319–337, Dordrecht, The Netherlands: Kluwer Academic Publishers, 1998.

[12] P. Boltenhagen, "Boundary effects on the maximal angle of stability of a granular packing," *European Physical Journal B*, vol. 12, pp. 75–77, 1999.

[13] R. L. Brown and J. C. Richards, *Principles of Powder Mechanics*. Oxford: Pergamon Press, 1970.

[14] J. Duran, *Sands, Powders, and Grains*. New York: Springer, 2000.

[15] Y. Grasselli and H. J. Herrmann, "On the angles of dry granular heaps," *Physica A*, vol. 246, pp. 301–312, 1997.

[16] R. A. Bagnold, "Experiments on a gravity-free dispersion of large solid spheres in a newtonian fluid under shear," *Proceedings of the Royal Society of London A*, vol. 225, pp. 49–63, 1954.

[17] C. M. Dury, G. H. Ristow, and M. Nakagawa, "Angle of repose in a rotating drum," in *Powders and Grains '97* (R. P. Behringer and J. T. Jenkins, eds.), pp. 507–510, Rotterdam, The Netherlands: Balkema, 1997.

[18] O. Reynolds, "On the dilatancy of media composed of rigid particles in contact, with experimental illustrations," *Philosophical Magazine*, vol. 20, pp. 469–481, 1885.

[19] L. Vanel, D. Howell, D. Clark, R. P. Behringer, and E. Clément, "Memories in sand: Experimental tests of construction history on stress distributions under sandpiles," *Physical Review E*, vol. 60, no. 5, pp. R5040–R5043, 1999.

[20] C. Goldenberg and I. Goldhirsch, "Force chains, microelasticity, and macroelasticity," *Physical Review Letters*, vol. 89, no. 8, p. 084302, 2002.

[21] J. P. Wittmer, P. Claudin, M. E. Cates, and J.-P. Bouchaud, "An explanation for the central stress minimum in sand piles," *Nature*, vol. 382, pp. 336–338, 1996.

[22] M. E. Cates, J. P. Wittmer, J.-P. Bouchaud, and P. Claudin, "Jamming, force chains, and fragile matter," *Physical Review Letters*, vol. 81, no. 9, pp. 1841–1844, 1998.

[23] S. B. Savage, "Modeling and granular material boundary value problems," in *Physics of Dry Granular Media* (H. J. Herrmann, J.-P. Hovi, and S. Luding, eds.), pp. 25–95, Dordrecht, The Netherlands: Kluwer Academic Publishers, 1998.

[24] A. P. F. Atman, P. Brunet, J. Geng, G. Reydellet, P. Claudin, R. P. Behringer, and E. Clément, "From the stress response function (back) to the sand pile "dip"," *European Physical Journal E*, vol. 17, pp. 93–100, 2005.

[25] D. O. Krimer, M. Pfitzner, K. Bräuer, Y. Jiang, and M. Liu, "Granular elasticity: General considerations and the stress dip in sand piles," *Physical Review E*, vol. 74, p. 061310, 2006.

[26] H. Hertz, "On the contact of elastic solids," *Journal für die Reine und Angewandte Mathematik*, vol. 92, pp. 156–171, 1881.

[27] L. D. Landau and E. M. Lifshitz, *Theory of Elasticity*. Oxford: Butterworth-Heinemann, 2nd ed., 1986.

[28] K. L. Johnson, *Contact Mechanics*. Cambridge: Cambridge University Press, 1985.

[29] V. V. Sokolovski, *Statics of Granular Media*. Oxford: Pergamon Press, 1965.

[30] H. A. Janssen, "Versuche über getreidedruck in silozellen," *Z. Ver. Dt. Ing.*, vol. 39, pp. 1045–1049, 1895.

[31] J. Jaky, "Earth pressure in silos," in *Proceedings of the 2nd International Conference on Soil Mechanics and Foundation Engineering*, pp. 103–107, June 1948.

[32] J. P. Bouchaud, P. Claudin, M. E. Cates, and J. P. Wittmer, "Models of stress propagation in granular media," in *Physics of Dry Granular Media* (H. J. Herrmann, J.-P. Hovi, and S. Luding, eds.), pp. 97–121, Dordrecht, The Netherlands: Kluwer Academic Publishers, 1998.

[33] F. Cantelaube and J. D. Goddard, "Elastoplastic arching in 2d granular heaps," in *Powders and Grains '97* (R. P. Behringer and J. T. Jenkins, eds.), pp. 231–234, Rotterdam, The Netherlands: Balkema, 1997.

[34] F. Cantelaube, A. K. Didwania, and J. D. Goddard, "Elastoplastic arching in two dimensional granular heaps," in *Physics of Dry Granular Media* (H. J. Herrmann, J.-P. Hovi, and S. Luding, eds.), pp. 123–127, Dordrecht, The Netherlands: Kluwer Academic Publishers, 1998.

[35] S. B. Savage, "Problems in the statics and dynamics of granular materials," in *Powders and Grains '97* (R. P. Behringer and J. T. Jenkins, eds.), pp. 185–194, Rotterdam, The Netherlands: Balkema, 1997.

[36] J.-P. Bouchaud, P. Claudin, D. Levine, and M. Otto, "Force chain splitting in granular materials: A mechanism for large-scale pseudo-elastic behaviour," *European Physical Journal E*, vol. 4, pp. 451–457, 2001.

[37] B. O. Hardin and F. E. Richart, "Elastic wave velocities in granular soils," *Journal of the Soil Mechanics and Foundations Division, Proceedings of the American Society of Civil Engineers*, vol. 89, no. SM1, pp. 33–65, 1963.

[38] B. O. Hardin and W. L. Black, "Vibration modulus of normally consolidated clay," *Journal of the Soil Mechanics and Foundations Division, Proceedings of the American Society of Civil Engineers*, vol. 94, no. SM2, pp. 353–369, 1968.

[39] V. P. Drnevich and F. E. Richart, "Dynamic prestraining of dry sand," *Journal of the Soil Mechanics and Foundations Division, Proceedings of the American Society of Civil Engineers*, vol. 96, no. SM2, pp. 453–469, 1970.

[40] F. E. Richart, J. R. Hall, and R. D. Woods, *Vibrations of Soils and Foundations*. Englewood Cliffs, New Jersey: Prentice-Hall, 1970.

[41] S. N. Domenico, "Elastic properties of unconsolidated porous sand reservoirs," *Geophysics*, vol. 42, no. 7, pp. 1339–1368, 1977.

[42] S. K. Roesler, "Anisotropic shear modulus due to stress anisotropy," *Journal of the Geotechnical Engineering Division, Proceedings of the American Society of Civil Engineers*, vol. 105, no. GT7, pp. 871–880, 1979.

[43] P. Yu and F. E. Richart, "Stress ratio effects on shear modulus of dry sands," *Joural of Geotechnical Engineering*, vol. 110, no. 3, pp. 331–345, 1984.

[44] B. O. Hardin and G. E. Blandford, "Elasticity of particulate materials," *Joural of Geotechnical Engineering*, vol. 115, no. 6, pp. 788–805, 1989.

[45] T. G. Thomann and R. D. Hryciw, "Laboratory measurement of small strain shear modulus under K_0 conditions," *Geotechnical Testing Journal*, vol. 13, no. 2, pp. 97–105, 1990.

[46] S. Shibuya, F. Tatsuoka, S. Teachavorasinskun, X. J. Kong, F. Abe, Y.-S. Kim, and C.-S. Park, "Elastic deformation properties of geomaterials," *Soils and Foundations*, vol. 32, no. 3, pp. 26–46, 1992.

[47] R. Bellotti, M. Jamiolkowski, D. C. F. Lo Presti, and D. A. O'Neill, "Anisotropy of small strain stiffness in Ticino sand," *Géotechnique*, vol. 46, no. 1, pp. 115–131, 1996.

[48] P.-Y. Hicher, "Elastic properties of soils," *Joural of Geotechnical Engineering*, vol. 122, no. 8, pp. 641–648, 1996.

[49] E. Hoque, F. Tatsuoka, and T. Sato, "Measuring anisotropic elastic properties of sand using a large triaxial specimen," *Geotechnical Testing Journal*, vol. 19, no. 4, pp. 411–420, 1996.

[50] G.-L. Jiang, F. Tatsuoka, A. Flora, and J. Koseki, "Inherent and stress-state-induced anisotropy in very small strain stiffness of a sandy gravel," *Géotechnique*, vol. 47, no. 3, pp. 509–521, 1997.

[51] Y. Kohata, F. Tatsuoka, L. Wang, G.-L. Jiang, E. Hoque, and T. Kodaka, "Modelling the non-linear deformation properties of stiff geomaterials," *Géotechnique*, vol. 47, no. 3, pp. 563–580, 1997.

[52] E. Hoque and F. Tatsuoka, "Anisotropy in elastic deformation of granular materials," *Soils and Foundations*, vol. 38, no. 1, pp. 163–179, 1998.

[53] X. Jia, C. Caroli, and B. Velicky, "Ultrasound propagation in externally stressed granular media," *Physical Review Letters*, vol. 82, no. 9, pp. 1863–1866, 1999.

[54] V. Fiorvante, "Anisotropy of small strain stiffness of Ticino and Kenya sands from seismic wave propagation measured in triaxial testing," *Soils and Foundations*, vol. 40, no. 4, pp. 129–142, 2000.

[55] R. Kuwano and R. J. Jardine, "On the applicability of cross-anisotropic elasticity to granular materials at very small strains," *Géotechnique*, vol. 52, no. 10, pp. 727–749, 2002.

[56] E. Hoque and F. Tatsuoka, "Effects of stress ratio on small-strain stiffness during triaxial shearing," *Géotechnique*, vol. 54, no. 7, pp. 429–439, 2004.

[57] N. HongNam, J. Koseki, and T. Sato, "Effect of specimen size on quasi-elastic properties of Toyoura sand in hollow cylinder triaxial and torsional shear tests," *Geotechnical Testing Journal*, vol. 31, no. 2, pp. 1–10, 2007.

[58] L. Bonneau, B. Andreotti, and E. Clément, "Surface elastic waves in granular media under gravity and their relation to booming avalanches," *Physical Review E*, vol. 75, p. 016602, 2007.

[59] P. A. Vermeer, "Non-associated plasticity for soils, concrete, and rock," in *Physics of Dry Granular Media* (H. J. Herrmann, J.-P. Hovi, and S. Luding, eds.), pp. 163–195, Dordrecht, The Netherlands: Kluwer Academic Publishers, 1998.

[60] J. A. Yamamuro and V. N. Kaliakin, eds., *Soil Constitutive Models: Evaluation, Selection, and Calibration*. Reston, Virginia: American Society of Civil Engineers, 2005.

[61] M. J. Boussinesq, "Essai théorique sur l'equilibre d'élasticité des massifs pulvérulents et sur la poussée des terres sans cohésion," *Mém. Acad. Sci.*, 1874.

[62] G. Gudehus in *Constitutive Relations for Soils* (G. Gudehus, F. Darve, and I. Vardoulakis, eds.), Rotterdam, The Netherlands: Balkema, 1984.

[63] Y. Jiang and M. Liu, "Incremental stress-strain relation from granular elasticity: Comparison to experiments," *Physical Review E*, vol. 77, p. 021306, 2008.

[64] J. Duffy and R. D. Mindlin, "Stress-strain relations and vibrations of a granular medium," *Journal of Applied Mechanics*, vol. 24, pp. 585–593, 1957.

[65] K. N. Kamrin, *Stochastic and Deterministic Models for Dense Granular Flow.* PhD thesis, Massachusetts Institute of Technology, 2008. `http://people.seas.harvard.edu/~kkamrin/`.

[66] M. Zytynski, M. F. Randolph, R. Nova, and C. P. Wroth, "On modelling the unloading-reloading behaviour of soils," *International Journal for Numerical and Analytical Methods in Geomechanics*, vol. 2, pp. 87–94, 1978.

[67] G. T. Houlsby and A. M. Puzrin, *Principles of Hyperplasticity: an approach to plasticity theory based on thermodynamic principles.* London: Springer, 2006.

[68] Y. Jiang and M. Liu, "Granular elasticity without the Coulomb condition," *Physical Review Letters*, vol. 91, no. 14, p. 144301, 2003.

[69] Y. Jiang and M. Liu, "Energetic instability unjams sand and suspension," *Physical Review Letters*, vol. 93, no. 14, p. 148001, 2004.

[70] Y. M. Jiang and M. Liu, "A unified theory of granular statics," in *Powders and Grains 2005* (R. García-Rojo, H. J. Herrmann, and S. McNamara, eds.), pp. 433–436, Leiden, The Netherlands: A. A. Balkema, 2005.

[71] K. Bräuer, M. Pfitzner, D. O. Krimer, M. Mayer, Y. Jiang, and M. Liu, "Granular elasticity: Stress distributions in silos and under point loads," *Physical Review E*, vol. 74, p. 061311, 2006.

[72] Y. Jiang and M. Liu, "A brief review of "granular elasticity"," *European Physical Journal E*, vol. 22, pp. 255–260, 2007.

[73] I. Einav and A. M. Puzrin, "Pressure-dependent elasticity and energy conservation in elastoplastic models for soils," *Journal of Geotechnical and Geoenvironmental Engineering*, vol. 130, no. 1, pp. 81–92, 2004.

[74] I. F. Collins and G. T. Houlsby, "Application of thermomechanical principles to the modelling of geotechnical materials," *Proceedings of the Royal Society of London A*, vol. 453, no. 1964, pp. 1975–2001, 1997.

[75] G. T. Houlsby and A. M. Puzrin, "A thermomechanical framework for constitutive models for rate-independent dissipative materials," *International Journal of Plasticity*, vol. 16, pp. 1017–1047, 2001.

[76] G. T. Houlsby, A. Amorosi, and E. Rojas, "Elastic moduli of soils dependent on pressure: a hyperelastic formulation," *Géotechnique*, vol. 55, no. 5, pp. 383–392, 2005.

[77] J. D. Goddard, "Nonlinear elasticity and pressure-dependent wave speeds in granular media," *Proceedings of the Royal Society of London A*, vol. 430, pp. 105–131, 1990.

[78] P.-G. de Gennes, "Static compression of a granular medium: the "soft shell" model," *Europhysics Letters*, vol. 35, no. 2, pp. 145–149, 1996.

[79] Y. C. Fung, *Foundations of Solid Mechanics*. Englewood Cliffs, New Jersey: Prentice-Hall, 1965.

[80] D. Kolymbas, *Introduction to Hypoplasticity*. Rotterdam, The Netherlands: Balkema, 2000.

[81] D. Kolymbas and I. Herle, "Hypoplasticity: A framework to model granular materials," in *Behaviour of Granular Materials* (B. Cambou, ed.), New York: Springer, 1998.

[82] Y. Jiang and M. Liu, "Hydrodynamic Theory of Granular Solids: Permanent, Transient and Granular Elasticity," *ArXiv e-prints*, vol. 706, June 2007.

[83] F. Alonso-Marroquin and H. J. Herrmann, "Ratcheting of granular materials," *Physical Review Letters*, vol. 92, p. 054301, 2004.

[84] H. A. Makse, "Nonlinear elasticity and thermodynamics of granular materials," *Advances in Complex Systems*, vol. 4, no. 4, pp. 491–501, 2001.

[85] H. A. Makse, N. Gland, D. L. Johnson, and L. Schwartz, "Granular packings: Nonlinear elasticity, sound propagation, and collective relaxation dynamics," *Physical Review E*, vol. 70, p. 061302, 2004.

[86] C. Goldenberg and I. Goldhirsch, "Friction enhances elasticity in granular solids," *Nature*, vol. 435, pp. 188–191, 2005.

[87] C. Goldenberg and I. Goldhirsch, "Effects of friction and disorder on the quasistatic response of granular solids to a localized force," *Physical Review E*, vol. 77, p. 041303, 2008.

[88] C. H. Rycroft, K. Kamrin, and M. Z. Bazant, "Defining and testing a granular continuum element." `http://repositories.cdlib.org/lbnl/LBNL-63631`, 2008.

[89] J. T. Jenkins and S. B. Savage, "A theory for the rapid flow of identical, smooth, nearly elastic particles," *Journal of Fluid Mechanics*, vol. 130, pp. 187–202, 1983.

[90] P. K. Haff, "Grain flow as a fluid-mechanical phenomenon," *Journal of Fluid Mechanics*, vol. 134, pp. 401–430, 1983.

[91] H. B. Callen, *Thermodynamics and an introduction to Thermostatistics*. New York: Wiley, 2nd ed., 1985.

[92] P. H. Mott, J. R. Dorgan, and C. M. Roland, "The bulk modulus and Poisson's ratio of "incompressible" materials," *Journal of Sound and Vibration*, vol. 312, pp. 572–575, 2008.

[93] G. T. Houlsby, "The use of a variable shear modulus in elastic-plastic models for clays," *Computers and Geotechnics*, vol. 1, pp. 3–13, 1985.

[94] R. I. Borja, C. Tamagnini, and A. Amorosi, "Coupling plasticity and energy-conserving elasticity models for clays," *Journal of Geotechnical and Geoenvironmental Engineering*, vol. 123, no. 10, pp. 948–957, 1997.

[95] A. I. Lurie, *Theory of Elasticity*. Berlin: Springer, 2005.

[96] H. E. Stanley, *Introduction to Phase Transitions and Critical Phenomena*. New York: Oxford University Press, 1971.

[97] L. AnhDan and J. Koseki, "Small strain behavious of dense granular soils by true triaxial tests," *Soils and Foundations*, vol. 45, no. 3, pp. 21–38, 2005.

[98] L. AnhDan, J. Koseki, and T. Sato, "Evaluation of quasi-elastic properties of gravel using a large-scale true triaxial apparatus," *Geotechnical Testing Journal*, vol. 29, no. 5, p. GTJ100221, 2006.

[99] D. J. Pickering, "Anisotropic elastic parameters for soil," *Géotechnique*, vol. 20, no. 3, pp. 271–276, 1970.

[100] Dassault Systèmes, *Abaqus Version 6.8 Documentation Collection*, 2008. `http://simulia.com`.

[101] L. Vanel, P. Claudin, J.-P. Bouchaud, M. E. Cates, E. Clément, and J. P. Wittmer, "Stresses in silos: Comparison between theoretical models and new experiments," *Physical Review Letters*, vol. 84, no. 7, pp. 1439–1442, 2000.

[102] A. Kézdi, *Erddrucktheorien*. Berlin: Springer, 1962.

[103] D. Schulze, *Powders and Bulk Solids*. Berlin: Springer, 2008.

[104] V. Sundaram and S. C. Cowin, "A reassessment of static bin pressure experiments," *Powder Technology*, vol. 22, pp. 23–32, 1979.

[105] G. Ovarlez, C. Fond, and E. Clément, "Overshoot effect in the Janssen granular column: A crucial test for granular mechanics," *Physical Review E*, vol. 67, p. 060302(R), 2003.

[106] L. Vanel and E. Clément, "Pressure screening and fluctuations at the bottom of a granular column," *European Physical Journal B*, vol. 11, pp. 525–533, 1999.

[107] G. Ovarlez and E. Clément, "Elastic medium confined in a column versus the Janssen experiment," *European Physical Journal E*, vol. 16, pp. 421–438, 2005.

[108] G. Reydellet and E. Clément, "Green's function probe of a static granular piling," *Physical Review Letters*, vol. 86, no. 15, pp. 3308–3311, 2001.

[109] D. Serero, G. Reydellet, P. Claudin, É. Clément, and D. Levine, "Stress response function of a granular layer: Quantitative comparison between experiments and isotropic elasticity," *European Physical Journal E*, vol. 6, pp. 169–179, 2001.

[110] A. P. F. Atman, P. Brunet, J. Geng, G. Reydellet, G. Combe, P. Claudin, R. P. Behringer, and E. Clément, "Sensitivity of the stress response function to packing preparation," *Journal of Physics: Condensed Matter*, vol. 17, pp. S2391–S2403, 2005.

[111] J. Boussinesq, *Application des Potentials à l'etude de l'équilibre et du mouvement des solides élastiques*. Paris: Gauthier-Villars, 1885.

[112] V. Cerruti, "Roma, acc. lincei," *Mem. fis. mat.*, p. 45, 1882.

[113] K. Takase, "Numerical simulations on dust-air two-phase flows in fusion experimental reactors during loss-of-vacuum-accident events," *Fusion Technology*, vol. 39, no. 2, pp. 1043–1049, 2001.

[114] K. Takase, "Three-dimensional numerical simulations of dust mobilization and air ingress characteristics in a fusion reactor during a LOVA event," *Fusion Engineering and Design*, vol. 54, no. 3-4, pp. 605–615, 2001.

[115] Y. Jiang and M. Liu, "From Elasticity to Hypoplasticity: Dynamics of Granular Solids," *Physical Review Letters*, vol. 99, p. 105501, Sept. 2007.

[116] M. Syamlal, W. Rogers, and T. O'Brien, *MFIX Documentation: Theory Guide*. Department of Energy: Morgantown Energy Technology Center, Morgantown, West Virginia, December 1993. DOE/METC-94/1004.

[117] D. G. Schaeffer, "Instability in the evolution equations describing incompressible granular flow," *Journal of Differential Equations*, vol. 66, pp. 19–50, 1987.

[118] A. Srivastava and S. Sundaresan, "Analysis of a frictional-kinetic model for gas-particle flow," *Powder Technology*, vol. 129, pp. 72–85, 2003.

[119] C. Leppert and D. Dinkler, "A fluid mechanical model for granular flow in silos," *Proceedings in Applied Mathematics and Mechanics*, vol. 5, pp. 309–310, 2005.

[120] R. Jackson, "Some mathematical and physical aspects of continuum models for the motion of granular materials," in *Theory of Dispersed Multiphase Flow* (R. E. Meyer, ed.), New York: Academic Press, 1983.

[121] D. G. Schaeffer and E. B. Pitman, "Ill-posedness in three-dimensional plastic flow," *Communications on Pure and Applied Mathematics*, vol. 41, pp. 879–890, 1988.

[122] E. B. Pitman and D. G. Schaeffer, "Stability of time dependent compressible granular flow in two dimensions," *Communications on Pure and Applied Mathematics*, vol. 40, pp. 421–447, 1987.

[123] D. D. Gray and J. M. Stiles, "On the constitutive relation for frictional flow of granular materials," tech. rep., Morgantown Energy Technology Center, Morgantown, WV, March 1988. DOE/MC/21353-2584.

[124] D. D. Gray and J. M. Stiles, "Theoretical and numerical studies of constitutive relations for frictional granular flow," tech. rep., Morgantown Energy Technology Center, Morgantown, WV, April 1990. DOE/MC/24207-2852.

[125] D. Gray, J. M. Stiles, and I. Celik, "Theoretical and numerical studies of constitutive relations for frictional granular flow," tech. rep., Morgantown Energy Technology Center, Morgantown, WV, January 1991. DOE/MC/24207-3009.

[126] A. N. Schofield and C. P. Wroth, *Critical State Soil Mechanics*. London: McGraw-Hill, 1968.

[127] G. I. Tardos, S. McNamara, and I. Talu, "Slow and intermediate flow of a frictional bulk powder in the couette geometry," *Powder Technology*, vol. 131, pp. 23–39, 2003.

[128] G. I. Tardos, "A fluid mechanistic approach to slow, frictional flow of powders," *Powder Technology*, vol. 92, pp. 61–74, 1997.

[129] P. C. Johnson and R. Jackson, "Frictional-collisional constitutive relations for granular materials, with application to plane shearing," *Journal of Fluid Mechanics*, vol. 176, pp. 67–93, 1987.

[130] S. Torquato, T. M. Truskett, and P. G. Debenedetti, "Is random close packing of spheres well defined?," *Physical Review Letters*, vol. 84, no. 10, pp. 2064–2067, 2000.

[131] S. Chapman and T. G. Cowling, *The Mathematical Theory of Non-Uniform Gases*. Cambridge: Cambridge University Press, 1970.

[132] S. B. Savage and D. J. Jeffrey, "The stress tensor in a granular flow at high shear rates," *Journal of Fluid Mechanics*, vol. 110, pp. 255–272, 1981.

[133] C. K. K. Lun, S. B. Savage, D. J. Jeffrey, and N. Chepurniy, "Kinetic theories for granular flow: inelastic particles in couette flow and slightly inelastic particles in a general flolwfield," *Journal of Fluid Mechanics*, vol. 140, pp. 223–256, 1984.

[134] D. Gidaspow, R. Bezburuah, and J. Ding, "Hydrodynamics of circulating fluidized beds, kinetic theory approach," in *Fluidization VII, Proceedings of the 7th Engineering Foundation Conference on Fluidization*, pp. 75–82, 1992.

[135] A. Einstein, "Elementare theorie der brownschen bewegung," *Zeitschrift für Elektrochemie und angewandte physikalische Chemie*, vol. 14, pp. 235–239, 1908.

[136] S. K. Friedlander, *Smoke, Dust, and Haze*. New York: Wiley, 1977.

[137] J. Fernandez de la Mora and D. E. Rosner, "Inertial deposition of particles revisited and extended: Eulerian approach to a traditionally lagrangian problem," *PhysicoChemical Hydrodynamics*, vol. 2, no. 1, pp. 1–21, 1981.

[138] A. L. Addy and B. J. Walker, "Rapid discharging of a vessel through a nozzle or an orifice," March 1972. ASME Paper 72-FE-40.

[139] C. J. Dutton and R. E. Coverdill, "Experiments to study the gaseous discharge and filling of vessels," *International Journal of Engineering*, vol. 13, pp. 123–134, 1997.

[140] F. P. Incropera and D. P. Dewitt, *Fundamentals of Heat and Mass Transfer*. New York: Wiley, 4th ed., 1996.

[141] O. C. Zienkiewicz and R. L. Taylor, *The Finite Element Method*, vol. 1. Oxford: Butterworth-Heinemann, 5th ed., 2000.

[142] F. Restagno, L. Bocquet, and E. Charlaix, "Where does a cohesive granular heap break?," *European Physical Journal E*, vol. 14, pp. 177–183, 2004.

[143] E. Barthel, "On the description of the adhesive contact of spheres with arbitrary interaction potentials," *Journal of Colloid and Interface Science*, vol. 200, pp. 7–18, 1998.

[144] U. D. Schwarz, "A generalized analytical model for the elastic deformation of an adhesive contact between a sphere and a flat surface," *Journal of Colloid and Interface Science*, vol. 261, pp. 99–106, 2003.

[145] R. S. Bradley, "The cohesive force between solid surfaces and the surface energy of solids," *Philosophical Magazine*, vol. 13, pp. 853–862, 1932.

[146] K. L. Johnson, K. Kendall, and A. D. Roberts, "Surface energy and the contact of elastic solids," *Proceedings of the Royal Society of London A*, vol. 324, no. 1558, pp. 301–313, 1971.

[147] V. M. Muller, B. V. Derjaguin, and Y. P. Toporov, "On two methods of calculation of the force of sticking of an elastic sphere to a rigid plane," *Colloids and Surfaces*, vol. 7, pp. 251–259, 1983.

[148] D. Maugis, "Adhesion of spheres: The JKR-DMT transition using a Dugale model," *Journal of Colloid and Interface Science*, vol. 150, no. 1, pp. 243–269, 1992.

[149] D. Tabor, "Surface forces and surface interactions," *Journal of Colloid and Interface Science*, vol. 58, no. 1, pp. 2–13, 1977.

[150] K. L. Johnson and J. A. Greenwood, "An adhesion map for the contact of elastic spheres," *Journal of Colloid and Interface Science*, vol. 192, pp. 326–333, 1997.

[151] J. A. Greenwood, "Adhesion of elastic spheres," *Proceedings of the Royal Society of London A*, vol. 453, pp. 1277–1297, 1997.